Exploration of approaches to shock-wave simulations

Jacob S. Wilkins

Submitted for the Degree of
Doctor of Philosophy

Department of Physics
University of York

September 2018

Abstract

This thesis covers research into a number of atomistic methods for the simulation of shock-waves, most importantly comparisons are drawn between the Hugoniostat method and non-equilibrium molecular dynamics (NEMD), with a view towards removing the limitations of pre-parametrised potentials in atomistic shock-wave studies and enable the capture of more complex phenomena and electronic properties.

Simulations were performed on Argon and Silicate structures using standard potentials (the Lennard-Jones and van Beest, Kramer, van Santen (BKS) potentials for Argon and SiO_2 respectively), *ab initio* approaches and neural network potentials.

In this work, we present a reparametrisation of the BKS potential, which corrects some of the known flaws of the short-range modification of the BKS potential of Farrow and Probert. We also present algorithms and equations for developments and improvements to the Hugoniostat method including: convergence rate enhancements, methods for elimination of transient states and an automated system for the generation of Hugoniot curves. We have also developed a procedure for creation of sets of systems for the purposes of generating neural network potentials for use in extreme rates simulations.

Further, we demonstrate the benefits of pseudo-equilibrium atomistic simulation to the study of shock-waves, with data obtained from these simulations including detailed local-structure analysis of shocked states of post-shock α-quartz and by applying known approaches of equilibrium molecular dynamics to the pseudo-equilibrium Hugoniostat method such as fluctuation formulae to calculate key system properties such as the Grüneisen parameter in the shocked state.

We also attempt to determine the limitations of the Hugoniostat, how far we can stretch the paradigm of reduced system sizes without compromising the validity of the calculation of certain properties.

Contents

List of Figures

List of Tables

List of Algorithms

Declarations

I declare that the work presented in this thesis, except where otherwise stated, is based on my own research and has not been submitted previously for a degree in this or any other university.

Signed

Jacob Wilkins

Acknowledgements

I would like to thank my supervisor Prof. Matt Probert for his constant support and guidance throughout this endeavour, for his encouragement to undertake my own projects which would be “useful in the long-run” or “good for the soul”, while still providing ever-present reminders to “do your PhD”.

I would also like to thank Dr Phil Hasnip for his invaluable assistance, advice, patience and knowledge, who has at many stages of this project helped academically, personally and in coffee-related matters.

I would also like to thank Dr Ian Bush for reading through and reviewing this work and giving helpful advice.

I would like to thank my parents for their encouragement and endurance over the years, for without them I would never have had this opportunity.

I would also like to thank all my friends for their tolerance to inane ramblings, their advice and discussions and their being there when things looked like they were going nowhere.

Glossary of terms and common symbols

- Notation

  $\mathbf{V}$ A vector is designated by being in bold font.

  $\underline{\underline{\mathbf{M}}}$ A matrix or rank-2 tensor is designated by being in bold font with a double underline.

  $\dot{x}$ Refers to the first-order time derivative if not explcitly noted.

  $\ddot{x}$ Refers to the second-order time derivative.

  $\|\mathbf{V}\|$ The euclidean norm of a vector

  $\left\|\underline{\underline{\mathbf{M}}}\right\|$ The determinant of a matrix

  EoM refers to equation of motion.

  EoS refers to equation of state.

- Constants

  k_B The Boltzmann constant.

  $N(0,1)$ A number drawn from the Gaussian normal distribution of mean 0 and variance of 1.

- Variables

  $\mathscr{H}$ Refers to a Hamiltonian.

  $\mathscr{L}$ Refers to a Liouville operator.

  $\mathbf{r}$ Position of an atom within a cell.

  $\mathbf{v}$ Velocity of an atom.

  $\mathbf{F}$ Force on an atom.

  $\mathbf{q}$ Generalised position coordinate.

  $\mathbf{p}$ Momentum of an atom or generalised momentum coordinate.

  $\underline{\underline{\mathbf{P}}}$ The pressure tensor.

  P The hydrostatic pressure, defined as $\frac{1}{3}\mathbf{tr}\left(\underline{\underline{\mathbf{P}}}\right)$.

  m Mass of an atom.

  $\underline{\underline{\mathbf{h}}}$ Matrix of cell vectors.

  V The volume of the cell, defined as $\left\|\underline{\underline{\mathbf{h}}}\right\|$.

  ε The compression of the cell, defined as $\frac{V}{V_0}$.

  Δt The finite time-step in molecular dynamics integration.

Chapter 1

Introduction

1.1 Why Shock-waves? Why Simulations?

Shock-wave physics is a field of studying extremes: extreme temperatures, extreme pressures and extremely fast timescales. Therefore, it is important for us to be able to study these things with extreme precision and accuracy.

High-pressure physics experiments have two main ways of reaching extreme conditions, these are either static (diamond anvil cell or other compression) or dynamic (shock-waves) (See §1.5.1.1). This makes shock-waves a subject of great interest to a variety of fields, from materials development in engineering to extreme geophysical studies [Medici *et al.*, 2013].

Unfortunately, although many developments in recent years have greatly improved the levels of accuracy and time-scales which are accessible to experiments, many of the processes which we would wish to measure in real materials remain inaccessible due to time-scale or simply material or the experimental apparatus required to measure them being prohibitively expensive. This is where the power of simulation can step in and relieve the burden.

The process of performing static compressions in simulations is well defined [Andersen, 1980] and has been performed for many years using advanced techniques. However, it has only been in relatively recent times that the power of computer hardware has reached a point where shock-wave simulations have been considered viable with an accurate scheme for generating the forces involved.

We hope to bring the power of the detail and accuracy of electronic structure calculations to a field where it has been considered impossible to do so for a long time.

1.2 Layout of Thesis

The remainder of this chapter begins with an introduction to shock-waves and a description of the features which separate them from other types of waves, followed by a discussion of the history behind both experimental and computational methods of measuring and describing shock-waves in materials. Chapter 2 covers the principal theoretical background and means by which this work will be undertaken. Chapter 3 summarises the potentials and force-fields which are used in this work, chapter 4 describes the work undertaken in this project to modify the Hugoniostat to improve its applicability in *ab initio* molecular dynamics calculations. Chapters 5 and 6 present the results of these simulations for Lennard-Jonesium and quartz and chapter 7 summarises and concludes the thesis and suggests work to be undertaken in future projects.

1.3 What is a Shock-wave?

In short, a shock-wave is a state where a material has an injected wave whose velocity is greater than the speed of sound in the medium. The speed of sound is the maximum speed at which the crystal can effectively disperse energy through an elastic wave. The result of this is that the system undergoes a plastic deformation to release the energy.

A shock is generally made up of several major parts, which we will cover in full below, the parts are:

1. Unshocked material – Material which has not yet been reached by the shock-wave, resting in its natural crystal state,
2. Shock front – Split into two parts the shock-front is the area through which the wave-front is currently moving
   (a) Elastic wave – The wave which is able to disperse the energy without destroying the crystal by occupying high energy phonon modes,
   (b) Plastic wave – The wave of structural distortion which permanently deforms the crystal structure,
3. Release wave – A wave of expansion which follows in the wake of the compressive waves as the material is now able to relax outwards,
4. Post-shock material – The material which has been shocked and is now trying to reform, or that which has spallated (been cast off or evaporated from the bulk as “spall”)

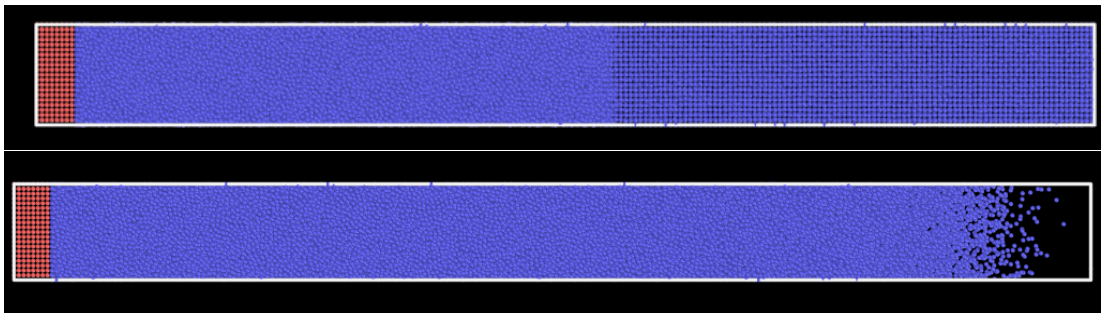

Figure 1.1: (Top) Shock passing through a solid material (left-to-right), note the discontinuity at the shock front. (Bottom) Material after the shock has passed through, the material here is free to spallate as the end has open boundaries. The red section identifies the fixed piston.

These different regions can pose a major problem for simulation due to the diversity of the states which exist simultaneously, and the extreme conditions reached, particularly at the shock-front, can cause any number of problems for the potential (§3) or for the integration algorithms (§2.4).

1.3.1 Unshocked Region

The unshocked region is the region through which the shock-front has not propagated. It is generally considered to be a relaxed ground-state of the material of interest. This region is usually relatively cold, and stable.

1.3.2 Shock-Front

The shock-front and the region just behind it is the main region of interest in a shock-wave simulation as it is where the most dynamics occur and the dynamics which are unique to a shock-wave. The shock-front propagates through the material at a speed greater than the speed of sound in that material. It is made up of two key parts: the elastic wave and the plastic wave. It is the focus of the majority of shock-wave simulation techniques, many of which attempt to remove other parts of the shocked system by various means.

1.3.2.1 Elastic Wave

The elastic wave is the material attempting to disperse the excess energy into accessible phonon modes. In weak enough impacts, the shock can be dissipated entirely by an elastic response from the material. These cases, however, cannot strictly be deemed shocks, as the definition of the shock is that there is a near-discontinuous change propagating through the material [Anderson,

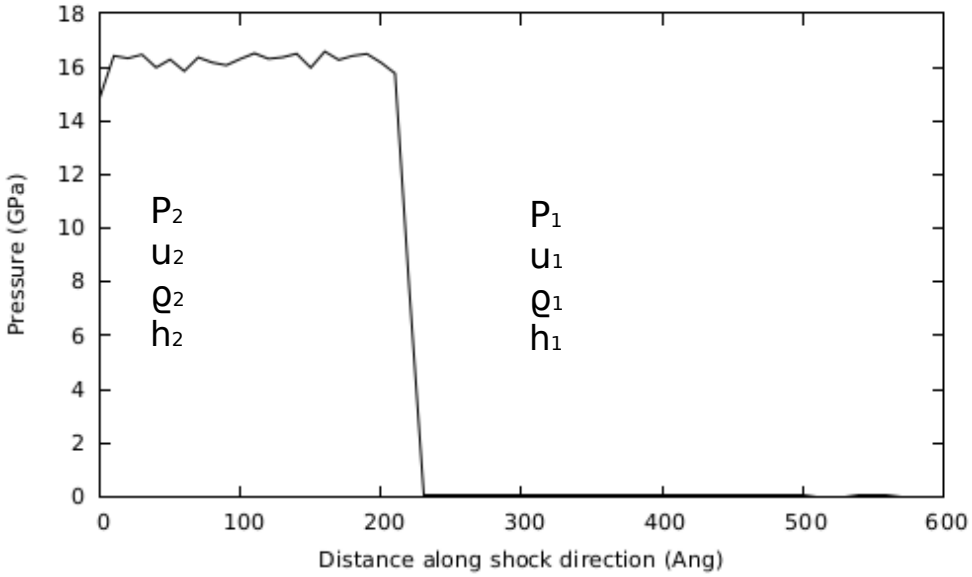

Figure 1.2: Graph showing pressure discontinuity at shock-front caused by a shock-wave in Lennard-Jones Argon due to a flyer-plate impact at 2km/s. The discontinuity exists in many system properties such as pressure, velocity, density and energy (Eqs. 1.5 – 1.7).

2001]. In a shock, the energy is too great to be effectively dispersed and so a plastic deformation occurs. In weak shock-waves, a clear elastic wave precedes the plastic shock-wave and in this instance is called an elastic precursor. In stronger shock-waves, it is often presumed that the elastic wave is overtaken by the plastic wave and so is rendered invisible and ineffectual, however, recent studies have found this to not be the case [Zhakhovsky *et al.*, 2011].

The elastic response of the material can be shown to be described by Hooke's law [Hooke *et al.*, 1678] for small atomic displacements. Assuming that we expand an arbitrary potential at its minimum (r) by a Taylor series, we find:

$$V(r+\delta r) \simeq V(r) + \delta r \left.\frac{\mathrm{d}V}{\mathrm{d}r}\right|_r + \left.\frac{\delta r^2}{2!}\frac{\mathrm{d}^2V}{\mathrm{d}r^2}\right|_r . \tag{1.1}$$

However, by definition at the minimum of the potential:

$$F(r) = -\left.\frac{\mathrm{d}V}{\mathrm{d}r}\right|_r = 0, \tag{1.2}$$

therefore we find that:

$$V(r+\delta r) \simeq V(r) + \left.\frac{\delta r^2}{2!}\frac{\mathrm{d}^2V}{\mathrm{d}r^2}\right|_r , \tag{1.3}$$

and that the force between the particle and its neighbours is:

$$F(r+\delta r) = -\frac{\mathrm{d}V}{\mathrm{d}r} \simeq -\delta r \left.\frac{\mathrm{d}^2V}{\mathrm{d}r^2}\right|_r, \tag{1.4}$$

that is a restoring force which is linear with respect to its displacement.

Hooke's law governs a large number of the processes described in this work, from approximations to the transmission of sound waves in the material, to material responses to compressions.

1.3.2.2 Plastic Wave

Plastic deformation occurs when the small displacements governing Hooke's law no longer apply and the material is deformed beyond its spring limit, and when the resulting restoring force does not return the displaced atom to its original location.

In a shock-wave, the plastic wave follows closely behind the elastic wave and is defined as a wave which causes persistent damage to the crystal structure. The energy in a plastic wave can be sufficient to cause melting of the material and complete destruction of the crystal lattice such that it cannot reform into its original state.

1.3.3 Release

The release wave is the material's response to its compression after the shock-wave has passed through the material and new material has stopped being forced into the region. Due to the high pressure state the material is in, molecular forces try to return the material to its original state and respond by overextending the material. Several of these elastic compressive-release cycles can occur as the material attempts to dissipate the energy.

1.3.4 Post-Shock Material

After the shock has passed through the subject medium, the system attempts to restore some sort of order as it cools and the energy dissipates, but is often left with many disrupted structures: grain boundaries, vacancies, meta-stable phases, etc.

This region is particularly difficult to accurately explore in simulation due to the time-scales over which simulations can operate compared to those of real-

world experiments. The rapid rate of cooling accessible in simulations usually results in glassy, amorphous phases of material where in real life, exotic high pressure phases can be found, such as stishovite around meteoric impact sites [Fleischer, 1962].

1.4 The Hugoniot equation of state

During early developments in the study of discontinuities and their stability and presence in fluids, Rankine [1870] and Hugoniot [1887] independently discovered some key relationships from the conservation laws of fluids. These were found by Rayleigh [1910] to be the same solutions from different perspectives, and so these are now called the Rankine-Hugoniot equations. The state of the system determined by these equations is referred to as the "Hugoniot".

The Hugoniot equation, describe the locus of all possible thermodynamic states reachable by the shocked system, and so forms the basis for the equation of state of a shock-wave and describes how a shock-wave discontinuity forms on both sides of the shock-front. It is formed from 3 fundamental conservation laws:

$$\text{Mass:} \qquad \rho_1 u_1 = \rho_2 u_2 \tag{1.5}$$

$$\text{Momentum:} \qquad \rho u_1^2 + P_1 = \rho u_2^2 + P_2 \tag{1.6}$$

$$\text{Energy:} \qquad h_1 + \tfrac{1}{2}u_1^2 = h_2 + \tfrac{1}{2}u_2^2, \tag{1.7}$$

where subscript 1 and 2 refer to the states ahead and behind the shock-front, ρ is the mass density of the fluid, u is the fluid velocity, P is the pressure and h is the specific enthalpy (per unit mass). It can also be formulated in terms of the shock speed:

$$\text{Mass:} \qquad \rho_1 u_s = \rho_2 (u_s - u_2) \tag{1.8}$$

$$\text{Momentum:} \qquad P_2 - P_1 = \rho_2 u_2 (u_s - u_2) = \rho_1 u_s u_2 \tag{1.9}$$

$$\text{Energy:} \qquad P_2 u_2 = \rho_1 u_s \left(\tfrac{1}{2}u_2^2 + e_2 - e_1\right), \tag{1.10}$$

where u_s is the shock speed and e is the specific internal energy. Using substitutions of Eqs. 1.8 & 1.9 into Eq. 1.10 it is possible to derive the Hugoniot equation:

$$e_2 - e_1 = \tfrac{1}{2}(P_1 + P_2)\left(\rho_1^{-1} - \rho_2^{-1}\right), \tag{1.11}$$

which in the per-unit-mass basis gives us:

$$e_2 - e_1 = \tfrac{1}{2}(P_1 + P_2)(V_1 - V_2)\,, \tag{1.12}$$

which is essential to the derivation of the Hugoniostat (§2.4.9).

For many materials, the shock (u_s) and the particle (u_p) velocities are related by a linear dependence [Kanel *et al.*, 2004]:

$$u_s = v_s + s\,u_p, \tag{1.13}$$

where v_s is the speed of sound, s is some constant which is material dependent.

For a full review and detailed analysis of some of the assumptions made in the Rankine-Hugoniot formulation of shock mechanics see Krehl [2015].

1.4.1 Rayleigh Lines

A Rayleigh line is underpinned by the assumption that the P-V Hugoniot is the set of accessible states of independent shocks, if the wave can be considered independent and adiabatic. Under this assumption, we can estimate the jump-conditions for any initial to any final state on the Hugoniot by a straight line.

Rayleigh lines may be described by a combination of Eqs. 1.8 and 1.9 which gives us:

$$P_2 - P_1 = u_s^2\left(\rho_1 - \frac{\rho_1^2}{\rho_2}\right), \tag{1.14}$$

or eqivalently:

$$P_2 = P_1 + u_s^2\rho_1^2(V_1 - V_2)\,, \tag{1.15}$$

which shows that the difference between any two pressures on the P-V Hugoniot can be related by a linear corresponding change in densities with $-\left(\frac{u_s}{V_1}\right)^2$ as the gradient. This linear correspondence defines the Rayleigh line between two states.

1.4.2 Alternative Equations of State

An alternative equation of state for shocked systems is the Mie-Grüneisen [Mie, 1903] equation of state, which uses the Grüneisen parameter [Grüneisen, 1912] to form a relationship between the pressure and volume of a solid at a

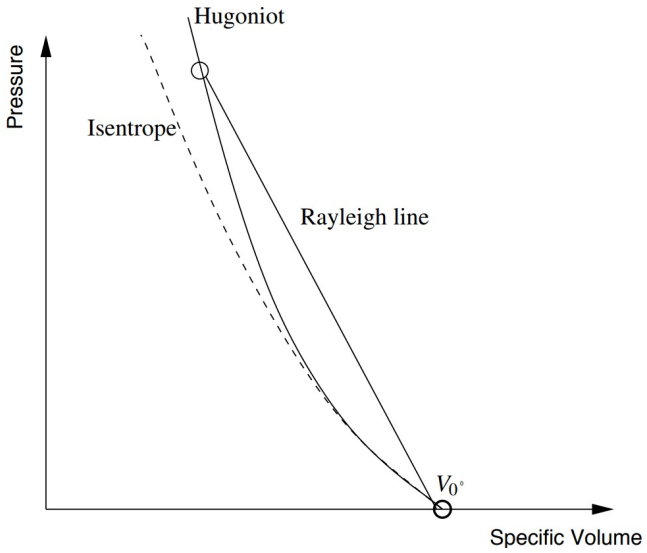

Figure 1.3: Example Hugoniot showing Rayleigh lines and the isentrope. Figure taken from Farrow [2009]

given temperature. The Mie-Grüneisen equation of state can be given as:

$$P = \frac{\rho_0 v_s^2 \chi \left(1 - \frac{1}{2}\gamma_0 \chi\right)}{(1 - s\chi)^2} + \gamma_0 E, \tag{1.16}$$

where subscript 0 means those measurements made in the reference state, E is the internal energy, $\chi = 1 - \varepsilon$ is the compression, v_s is the speed of sound, γ is the Grüneisen parameter (§2.5.9), $s = \frac{\mathrm{d}U_s}{\mathrm{d}U_p}$ is a Hugoniot slope, U_s is the shock velocity and U_p is the piston velocity.

The Mie-Grüneisen EoS can be used to calculate the adiabatic bulk modulus and other properties of the shocked state.

Many other equations of state can be also be derived from conservation relations between pre- and post-shock and more complex measures can be added to account for the anharmonicity in the lattice under shock, but these will not be explored in this work. See Klotz *et al*. [2012] for an extended review of shock equations of state.

1.5 Review of Prior Work

The aim of this section is to provide a brief overview of the current state of understanding of shock-wave physics both experimentally and theoretically.

1.5.1 Shock-wave Experiments

Shock-wave experiments are a well established means of exploring the effects of extreme physical states. Unfortunately, they are limited by the resolution to which the results can be recorded and analysed. In spite of many recent developments in high-speed techniques, faster computers and more resilient materials, the main limitation remains the ability of the experimental equipment to withstand the extreme conditions it experiences in measuring the shock.

Shock-wave experiments can also be expensive as they usually destroy the sample material and, in the case of explosive detonation experiments, the explosive sources and sometimes recording equipment. Extreme pressures require expensive materials such as diamond in order to maintain the pressures desired, though more recently lab-grown diamonds have reduced these costs significantly.

Though the focus of this work is purely on the theoretical simulation of shock-waves, it is important to have an understanding of the experimental methods and measurements in order to be able to produce comparable simulations and corroborative analyses. As such, a brief description of some experimental methods and measurements follow.

1.5.1.1 Experimental Methods

There are many approaches which are used in experiments in order to create shock-waves in materials. This section outlines a selection of the methods which we may hope to reproduce in simulations, along with a brief analysis of the advantages and disadvantages associated with each.

Explosive Detonation The most obvious way for a shock-wave to be generated in a material is to inject a large amount of energy into the material in a very short time-span. Explosives serve this purpose well and are frequently used to this end, pressures upwards of 10TPa have been generated using nuclear blasts, but bans of nuclear weapons testing mean this is no longer possible [Trunin, 1998].

Blasts from common chemical explosives such as TNT and RDX can reach $\sim$1TPa, which is sufficient for many applications [Rice *et al.*, 1958]. Unfortunately there are many difficulties in measuring such experiments due to the uncontrollable nature of explosives, and the wide area that is affected by the explosion, which can overwhelm and damage sensitive apparatus.

A more recent approach to explosive-initiated shock-waves is that of laser in-

duced shock, where a laser is used to locally apply extreme heating causing the material surface to expand rapidly, effectively inducing a detonation shock into the medium, but with a more controllable and directed impulse with much lower collatoral damage and less risk to measurement apparatus [Kubota *et al.*, 2001]. This method even extends to using Z-Pinch produced X-Ray induced shocks into media [Konrad *et al.*, 1998].

Split-Hopkinson Pressure Bar The Hopkinson pressure bar is a way of measuring induced shock pressure-transfer in materials by examining the transfer to a known material and measuring the properties in the known material [Hopkinson, 1914]. In this way it was made possible to measure shocks which were beyond the perceived maximum resolution of the time.

The more modern split-Hopkinson pressure bar, designed by Volterra [1948] to have two bars suspended freely, and later improved by Kolsky [1949] to use fixed bars, uses a pair of Hopkinson bars to introduce a longitudinal shock-wave into the sample material.

Placing the sample between two bars, and initiating a stress wave into one of the bars (the "incident bar"). The wave which passes through the sample then enters the other bar (the "transmission" bar) and is dissipated. Measurements of the properties of the shock in the transmission bar such as the stress-strain and shock speed can be made and compared with those of known values for the bar material. Using matching techniques it is possible to calculate the corresponding properties in the sample material. The stress wave may be caused by a variety of mechanisms including a gas-gun launched "striker" bar or explosive detonations.

The Hopkinson bar can also be used to test torsional and tensile properties by varying the set-up slightly.

Flyer Plate Experiments The flyer plate approach involves launching a projectile of sample material against a resistant target and introducing a shock-wave through the impact or firing a resistant projectile against a target of sample material [Davison and Graham, 1979]. The sample is usually wedged between two plates to enforce a planar shock in the sample. The plate material's Hugoniot is known, and from this is it possible to use a method called impedance matching to calculate the shock through the sample accurately.

The propellant for the flight is often either a high pressure, light gas or an explosive detonation building enough pressure to burst a cap, releasing the gas against the flyer plate, launching it (Fig. 1.4).

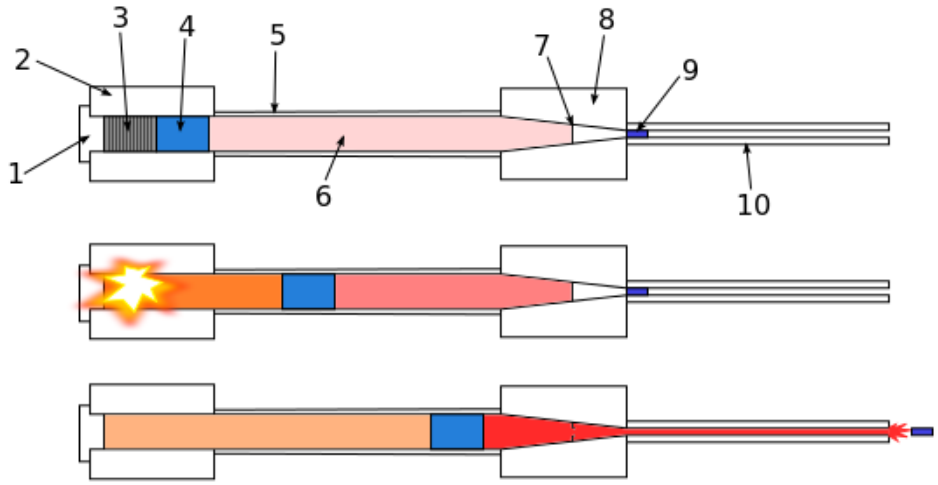

Figure 1.4: Gas gun schematic and operation mechanism. Labelled points are: 1 – Breech block, 2 – Chamber, 3 – Propellant charge, 4 – Piston, 5 – Pump tube, 6 – Light gas, 7 – Rupture disk, 8 – High pressure coupling, 9 – Projectile, 10 – Gun barrel. Taken from: Wikipedia [b]

Gas-gun experiments are favoured over explosive detonations in many cases for their relative safety and ability to reach large pressures in a controlled manner.

Diamond-Anvil Cell The diamond-anvil cell (DAC) is a system for applying high loads of static pressure to a material (up to around TPa ranges, but more typically 200GPa [Dubrovinskaia *et al.*, 2016]).

The set-up consists of a pair of fine diamond tips, usually sub-millimetre, linked with a pair of screws to aid the application of pressure, between which the sample is placed. As diamonds are transparent to a number of key light wavelengths, measurements of the sample material can be made using a variety of techniques (§1.5.2). Due to the size of the apparatus and the difficulty in attaining large pressures while making it any larger, the sample must be small in DAC experiments [Klotz *et al.*, 2012].

The obvious limitation to the pressures attainable in a diamond anvil cell actually lies in the construction material of the cell itself and the pressure limits before the cell itself ruptures.

1.5.2 Experimental Measurements

In shock and static compression experiments the ways in which we can measure the properties of materials are very diverse and can measure a wide range

of features [Klotz *et al.*, 2012].

VISAR Velocity Interferometer System for Any Reflector (VISAR) is a method for measuring the particle velocity in the medium of the shocked material. The system works by shining a coherent laser at the free surface of the sample of interest and measuring the interference produced by the Doppler shifted reflected waves [Barker, 1972].

VISAR is one of the key tools in experimentally determining the Hugoniot state.

IR Spectroscopy Infra-red Spectroscopy and Raman spectroscopy are useful tools for measuring thermal radiation emissions of the material under shock Dlott [1999].

IR temperature sensing is one of the few ways besides VISAR of getting an approximate measure of the particle velocities in a material and was the main method before VISAR was developed [Hall *et al.*, 1965].

X-Ray Diffraction X-Ray diffraction (XRD) is a method used to measure the crystal structure of the sample material by the reflection and deflection of X-Rays from the atoms in the sample material. It is a commonly used and well understood crystallographic technique to measure structure and it produces a Fourier-space representation of the crystal lattice.

For examination of static, high-pressure systems, the disadvantage of using XRD is that it requires that the anvil itself (or at least the gaskets) must be transparent to x-rays and also the time resolution of dynamic XRD measurements can be limiting, though recent developments have increased this resolution considerably [Klotz *et al.*, 2012].

Traditionally, it has only been possible to perform XRD on static high-pressure systems, though recent developments in x-ray diffraction crystallography have actually allowed for *in situ* examination of shock-waves [Wehrenberg *et al.*, 2017].

High Speed Cameras In many open shock-wave experiments, such as flyer plate or explosive detonations, direct visual (or high IR) spectrum cameras are used to provide a visual aid to describe how the system is responding on a macro-scale. It is common to employ techniques such as schlieren photography [Krehl and Engemann, 1995], which identifies density gradients in a transparent medium, to high speed imaging to identify properties of the shock.

High speed cameras have reached a scale such that in the extreme they can measure over 10^8 fps, which allows for the direct capture and measurement of shock transfer in harder materials [Honour, 2001].

1.5.3 Shock-wave Simulations

There are a number of different approaches which can be used to simulate a shock-wave in a material. Many of these methods differ in the amount of simulated material required to develop the measurements, the time-scales over which they can operate and the parts of the shock which they are able to reproduce. In general it is favourable to require less material and allow the shock to propagate indefinitely such that the calculations run sufficiently quickly and that long-time averages can be taken.

As is the case with all simulations, finite size effects can drastically alter the validity of a shock-wave simulation, and it is important to be aware of the approximate sizes which are required to allow proper dynamics to form.

One key difference between many types of shock simulation is whether the simulation covers the entire shock-wave moving through the system or merely the shocked portion and what is deemed important. Obviously in terms of the movement of material, the shock-front is the key, however, it may be that the surrounding regions of ambient material or wave splitting, reflection or interference in the medium may critically alter the material response, and in methods which ignore these larger scale waves, it may be that the real response may be very different. It is often assumed, however, that the length scales of real shocks – which may be in the order of centimetres ($10^{-2}m$) of material – relative to those which are possible in atomistic simulations – maybe up to $\sim$1000s of Ångströms ($10^{-7}m$) – means that the shock is effectively infinite in our simulations.

1.5.3.1 Simulation Methods

Finite element methods It is important to note that there exist methods which are not atomistic, i.e. do not represent the motion of each atom directly. Finite element methods subdivide regions of the material of interest into deformable blocks, whose macroscopic properties such as shear stress and bulk modulus may be input, which are affected by a general stress, rather than individual atomic interactions. Due to the immense variability of the scale of these divisions, it is possible to create finite element models on the scales on which the real shocks occur [Ashraf *et al.*, 2007]. Advanced methods may have adaptive

meshes [Nochetto *et al.*, 2009] which allow for even larger spatial scales while treating regions outside the area of interest crudely.

These approaches are usually heavily parametrised to material properties on a measurable and observable scale, but do not usually capture changes, for example in the crystal structure, which drastically affect the properties of the material.

The key focus of this work is to explore the effects of shock-waves on the crystal structure itself and as such, these methods are not suitable.

High Pressure Static Molecular Dynamics In order to simulate the properties which may occur in a shock-wave it is possible to run an NPT or NPH (§2.2) molecular dynamics (MD) simulation at the temperatures and pressures which may be reached in a shock. This method more accurately describes a simulation of a diamond-anvil cell experiment with controlled temperatures, though it can be used to extract properties which may be applicable to the shocked substance [Farrow, 2009].

The disadvantage of this approach is that in order to accurately mimic the state at a shock-front, certain parameters such as the energy injected and the pressure induced by the shock-wave must be known beforehand by other means before they can be used for the calculation; though a series of runs at different temperatures may give a spread of information allowing accurate averages to be determined.

Direct NEMD We can attempt to reproduce the flyer plate experiment directly by using an NVE simulation of a block of material whose initial velocity moves it towards a "momentum mirror" at a given piston speed [Holian, 1995]. This "momentum mirror" as the name suggests is a plane which reverses the momentum of any particle which impacts against it. Effectively, it can be considered as an infinitely massive wall, causing perfect elastic reflection of the incoming projectile.

The issue with momentum mirrors is that the shock they deliver, being perfectly elastic fails to capture some of the more subtle interactions of collisions and so causes unphysically strong shocks.

As such it is more common to use a softer wall interaction by launching the flyer plate at a wall of interacting medium, with artificially high mass to reduce the chance of coalescence and reflect the majority of momentum back at the flyer-plate [Farrow, 2009]. This soft-wall collision recreates the effect of a light flyer plate of material impacting on a bulk target more accurately than the

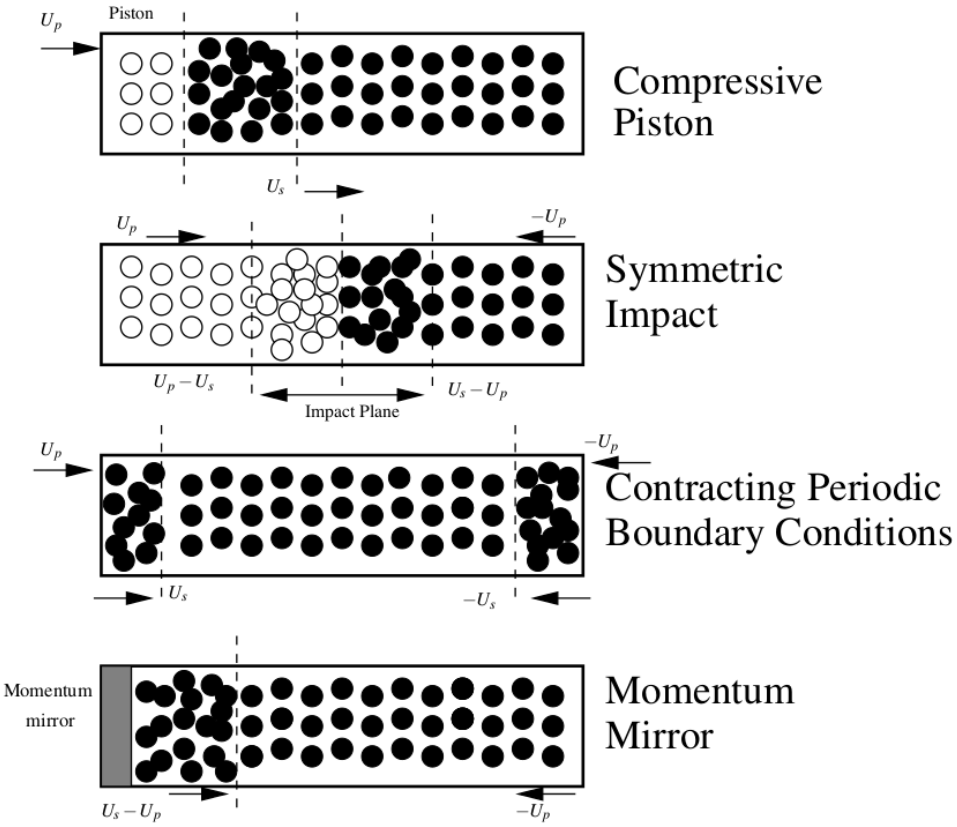

Figure 1.5: A diagram showing several approaches to NEMD shock-wave simulation. Taken from Farrow [2009].

momentum mirror, and the deceleration of the plate as it approaches the wall rather than an instantaneous inversion in direction means that this collision is more realistic (Fig. 1.5).

Piston Methods It is possible to think of cell volume changes as the action of a piston on the internal system (See: Appendix B), it is possible to use this "piston" to introduce a shock-wave into a system and allow it to propagate as a pressure induced shock.

Work by Anisimov *et al*. [1997] has attempted to improve this approach by modifying the potential across the system to improve the closeness to actual shock dynamics.

There are also methods which involve altering the boundaries of the cell to emulate this piston impact for forcing the material to interact with itself (Fig. 1.5).

Ram-Jet The Ram-Jet method or Moving Window Molecular Dynamics [Zhakhovskiĭ *et al*., 1999] is a method by making the simulation cell such that it follows a

window focused on the shock-front. A piston introduces a shock-wave into the system, and as particles are forced out the "back" side of the cell, new particles are created at the "front" side of the cell at the piston velocity to represent a shock in an infinitely long bulk crystal.

An advantage to this method is that it keeps that cell size constant and the system can effectively be kept in a shock state for an indefinite amount of time.

This approach would be incredibly difficult to achieve with a DFT model, because the act of creating and destroying particles within a DFT calculation would result in massive complications in calculating the electronic density.

Hugoniostat The term Hugoniostat describes a class of pseudo-ensembles which drive the temperature and pressure such that the system lies on the Hugoniot line [Maillet and Stoltz, 2008]. It does this via a thermo-barostat, which is derived from the Hugoniot-Rankine equations (§1.4). There are several approaches to the Hugoniostat which give different samplings of the pseudo-ensemble (§2.2) or have the properties of different integrators (§2.4).

A more detailed description of the different Hugoniostats can be found in §2.4.9.

1.5.4 Farrow and Probert

This work is built upon the prior work of Farrow [2009] and attempts to extend the simulation of shock-waves in CASTEP to that of *ab initio* force-fields (§3.2) for the calculation of the forces, rather than the empirical potentials used in Farrow and Probert [2011]. In order to do this, this work focuses on the implementation of the Hugoniostat (§2.4.9). The approach taken by Farrow [2009] was to perform NEMD shocks of empirical potential systems using the Lennard-Jones and modified BKS potentials (§3.1), along with *ab initio* and BKS simulations using static compression methods to explore the possibility of inducing phase transitions, demonstrate the importance of shocks as a driver of phase transitions and to measure the accuracy of their modified potential.

They provided a set of modifications ot the BKS potential to allow for shock-wave compressions, to switch to a core-core repulsion 6-2-1 potential at short ranges. This potential switching was designed to match the gradient at the point of inflexion of the BKS potential and to prevent unphysical fusion at high compressions. This approach was different to that taken by Guissani and Guillot [1996], who added a strong, but short-ranged Lennard-Jones-like (18-6) repulsion to the potential.

1.6 Materials

In this section, we will examine the test materials which we will be using for the entirety of this study. These are argon and silica (SiO_2). The reason for these choices is explored below.

1.6.1 Argon

Argon was the first of the noble gases to be discovered [Rayleigh and Ramsay, 1895] and its inert nature led to its rather derogatory name of "lazy" or "inactive". It is the third most abundant gas in the atmosphere after nitrogen and oxygen and is used in several applications where its inert nature plays to its favour, such as fire extinguishers for vulnerable equipment and the exclusion of corrosive material in processes such as welding. Its most common use, however is in incandescent lighting to prevent the degradation of the filament and gas-discharge ("neon") lamps to produce a blue light.

Argon is a common material of interest in simulations due to the simplicity of its interactions, being a noble gas, it forms no real bonds and so can be modelled using a simple induced-dipole-dipole interaction (§3.1.1). This cheap, and soft potential makes it ideal for testing purposes of algorithms. Due to the simplicity of the potential, many of its properties can and have been calculated analytically or numerically [Klein and Venables, 1976], which assists in the confirmation of an algorithm's correctness. Due to its abundance many experiments have been performed on Argon, and there is a plethora of data available in the literature (Klein and Venables [1976] and West [1974]).

Argon in its solid state is found experimentally to be an FCC crystal. Though it is known that the Lennard-Jones model for argon favours an HCP phase, it is metastable in the FCC phase [Kihara and Koba, 1952].

1.6.2 Silica

Silicates are one of the most abundant crystalline materials in the earth's crust [West, 1974], and make up for a large proportion of the crust and upper layers of the earth. They also form a rich and varied phase diagram with a large number of both stable and meta-stable phases. Their abundance in the earth's crust and mantle make their study essential for geophysical applications.

In the mantle, silicates are subjected to pressures over 100GPa and temperatures upwards of 1200K, at these temperatures and pressures they may become

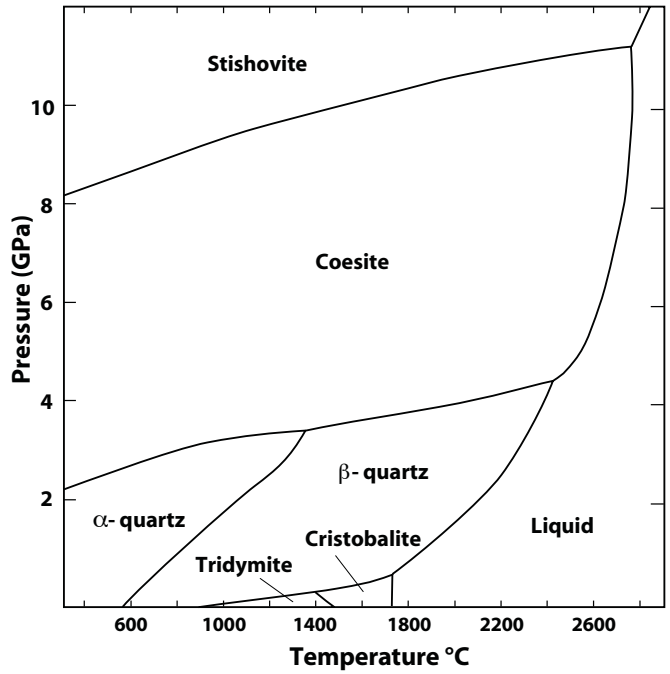

Figure 1.6: A phase diagram of silicate (SiO_2) minerals. The key phases which will be explored in this work are the α-quartz and β-quartz phases, along with the high pressure polymorphs of coesite and stishovite. Taken from SERC based on Swamy *et al*. [1994].

amorphous, but as we descend through the earth's crust many of the more exotic phases can be found. Due to its prevalence in the earth's crust, many interesting phases of silicates are also found around meteoric impact sites, where temperatures and pressures much higher than within the mantle would have temporarily existed.

Silica is a name given to a number crystalline phases of silicon-dioxide (SiO_2) formed from a number of tessellating SiO_4 tetrahedra. The stacking of these tetrahedra give rise to a number of different phases of silicates. The main structures which will be explored in this work will be the pressure and temperature induced phases of α-quartz, β-quartz, coesite and stishovite (Fig. 1.6), though stishovite under some definitions is strictly not a silica structure as it is not made up of tetrahedra (Fig. 1.10).

The silicates as a whole have been widely explored in shock experiments for their rich phase diagram (Fig. 1.6) and their abundance. Coesite and stishovite are collectively referred to as "shocked quartz" for their occurance in the aftermath of shock experiments and their appearance at sites where extreme shocks have occurred such as nuclear blasts and meteoric impacts.

1.6.2.1 α-Quartz

α-Quartz is the most common phase of silica on earth and is the usual state in which quartz is found. Many common minerals are polymorphs of, or impure, quartz crystals and such crystals are as diverse as amethyst, flint and rock crystal. Today it has many uses from glassmaking and fibre-optic cabling to piezoelectric crystals in watches and other devices.

Crystallographically speaking, α-quartz has a trigonal crystal structure in the $P3_221$ space group [West, 1974], its conventional cell has 9 atoms (Fig. 1.7).

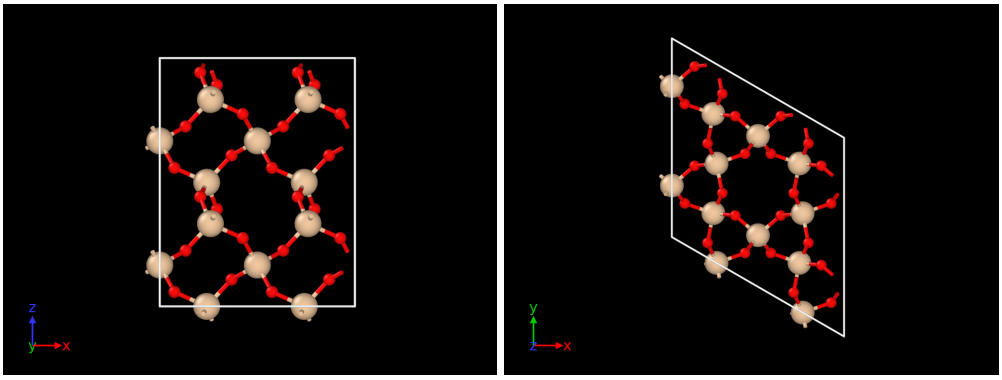

Figure 1.7: A schematic of the α-quartz structure. Each silicon is bound to 4 oxygens in a tetragonal arrangement.

1.6.2.2 β-Quartz

When heated beyond 573°C α-quartz undergoes what is known as an inversion and transitions to the β-quartz phase. This reaction is reversible and as such β-quartz does not commonly occur naturally. The transition is a simple rotation of the tetrahedra to form a hexagonal symmetry. β-quartz as a hexagonal crystal structure in the $P6_422$ group, its conventional cell has 9 atoms (Fig. 1.8).

1.6.2.3 Coesite

Coesite is a high-temperature (1000K), high-pressure (2-3 GPa) metastable polymorph of silica which was first discovered synthetically [Coes, 1953] while searching for other mineral structures. It was later found naturally occurring around a site which was believed to be the site of a meteorite impact.

Coesite is a monoclinic structure in the $C2/c$ group, its conventional cell has 24 atoms (Fig. 1.9).

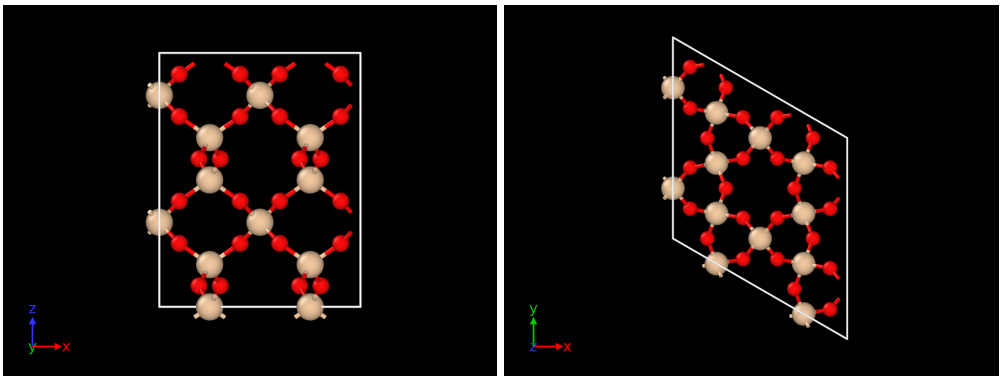

Figure 1.8: A schematic of the β-quartz structure. The α-quartz–β-quartz transition is simply a rotation of the tetrahedrons, so each silicon is still bound to 4 oxygens in a tetragonal arrangement.

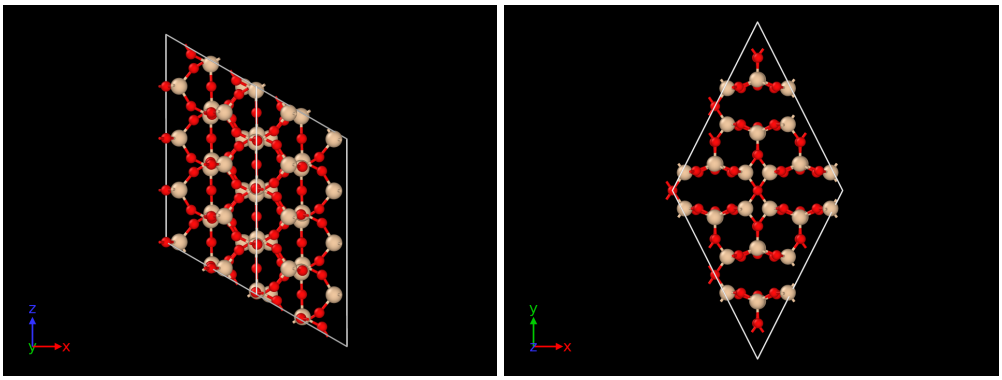

Figure 1.9: A schematic of the coesite structure. The crystal structure of the coesite phase is significantly changed from the α-quartz and β-quartz phases, and is a metastable high-pressure, high-temperature state which usually reverts to one of the lower phases when cooling unless quenched. Each silicon is bound to 4 oxygens in a tetragonal arrangement.

1.6.2.4 Stishovite

Stishovite is an ultra-hard dense phase of SiO_2 which is extremely rare to find in nature. It requires temperatures and pressures in excess of 1500K and 10GPa to form and was previously only found at meteorite impact sites though it has also been found in deposits extruded from the mantle and within diamonds.

Sitshovite is a tetragonal crystal in the $P4_2/mnm$ space group, its conventional cell has 6 atoms (Fig. 1.10)

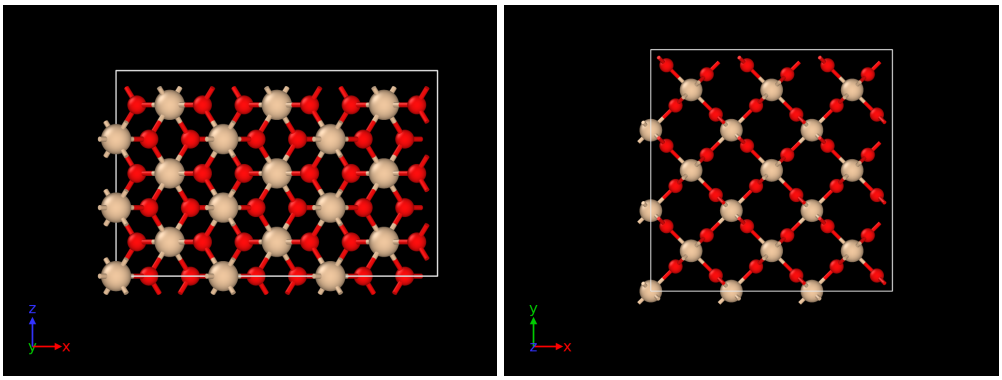

Figure 1.10: A schematic of the stishovite structure. The stishovite structure is a complete reordering of the crystal and instead of the silicate tetrahedra which define the silica phases, each silicon is now 6-fold co-ordinated with the oxygens. Stishovite is only found at extreme temperatures and pressures.

1.7 Software

In this work we will be using a number of software packages to simulate these materials and subsequently analyse the results using methods described below. These packages include:

- CASTEP [Clark *et al.*, 2005] - A primarily *ab initio* simulation package for materials into which empirical force-fields have been added for testing and development purposes by the author.
- LAMMPS [Plimpton, 1995] - An empirical force-field simulation package for materials
- MDTEP [Quigley] - A CASTEP specific post-hoc molecular dynamics analysis package which calculates several key properties
- OVITO [Stukowski, 2010] - A post-hoc molecular dynamics analysis package and visualisation tool

1.8 Summary

Throughout this work, we will be exploring the properties and structure of the shocked states of these media and perform analysis described in the following chapter to describe the reasons for the physical states and their implications for materials science.

Chapter 2

Molecular Dynamics

Molecular dynamics (MD) is a field which covers the study of the motion of materials on an atomistic scale, the applications of molecular dynamics extend from detailed small-scale studies of novel bulk materials Kalikka *et al*. [2014] to billion atom simulations of complete proteins [Jung *et al*., 2019]

A molecular dynamics simulation is essentially just the numerical propagation of Newton's Laws of Motion through time:

1. In an inertial reference frame, an object either remains at rest or continues to move at a constant velocity, unless acted upon by a force.

2. In an inertial reference frame, with constant mass, the vector sum of the forces $\mathbf{F}$ on an object is equal to the mass m of that object multiplied by the acceleration $\mathbf{a}$ of the object, i.e. $\mathbf{F} = m\mathbf{a}$.

3. When one body exerts a force on a second body, the second body simultaneously exerts a force equal in magnitude and opposite in direction on the first body.

Unfortunately, these equations become impossible to solve exactly for more than two bodies (the three-body problem), and so the exact integral of:

$$\ddot{\mathbf{r}}_i = \mathbf{a}_i = \frac{\partial^2 \mathbf{r}_i}{\partial t^2} = \frac{\mathbf{F}_i}{m_i}, \tag{2.1}$$

must be broken down into an approximate finite difference integral problem solving for $\mathbf{r}_i$ and $\mathbf{v}_i$. The choice of our finite element integrator makes a significant difference to our calculation's correctness (See: §2.4). We commonly use the term "trajectory", which describes a molecular dynamics sampling from an initial state to some finite time in the future.

The forces used in these calculations usually come from either a predefined equation designed to mimic the potential of a particular atomic system (§3.1) or from a solution of the Schrödinger equations and a sum of electronic contributions (§3.2).

2.1 Transient States and Equilibration

Due to the way in which molecular dynamics calculations are initialised, they are usually in a state which does not conform to the ensemble or desired state. As a result, it is generally necessary to equilibrate the system by allowing it to propagate for a period of time under the ensemble. The fact that the dynamics of the equilibration do not necessarily conform to the desirable states of the calculation, they are normally discarded from calculations and, as the results are already unphysical, accelerated methods are often used to reduce the required equilibration times.

Extreme transients also waste calculation time, which in *ab initio* calculations in particular can be costly, and so are generally best avoided. If the initial state is too far from the equilibrated state, then over- or under-shooting of the desired state can occur which, in extreme cases, can result in instability and ultimately failure of the calculation.

2.2 Standard Ensembles

A statistical ensemble is a means of controlling the microstates of a configuration space [Bowley and Sánchez] which can sampled by a molecular dynamics trajectory. An MD trajectory is equivalent to an average of many different configurations in which the system can exist, or a sampling of those that do exist (§2.3). In order to constrain or bias the sampling to a chosen property or set of states, certain properties of the system may be constrained or controlled for each particular problem.

Ensembles are generally denoted by a short alias describing the properties which are constrained in any particular run. A brief description of several key ones is contained below.

2.2.1 Microcanonical Ensemble

The microcanonical ensemble, or constant number of particles (N), volume (V) and energy (E) ensemble is the system which obeys Newton's Laws of motion for an isolated system, with no external perturbations. It is the simplest scheme and relies upon the conservation of energy of central forces in order to maintain a stable total energy.

2.2.2 Canonical Ensemble

The canonical ensemble, or constant number of particles (N), volume (V) and temperature (T) ensemble regulates the temperature of a system via a thermostat, i.e. attached to some form of heat-bath, to more accurately replicate the environments commonly found in experimental systems, where systems can not be totally isolated from their environments. There are a number of thermostats which can be used, which are described below (§2.4.7).

2.2.3 Isoenthalpic-isobaric Ensemble

The isoenthalpic-isobaric ensemble or constant number of particles (N), pressure (P) and enthalpy (H) ensemble uses a barostat to alter the volume of the system to regulate the pressure of the sample, it relies on the conservation of energy in order to conserve the constant enthalpy ($H = E + PV$) of the internal system. There are a number of barostats available, which are described below (§2.4.8)

2.2.4 Isothermal-isobaric Ensemble

The isothermal-isobaric ensemble or constant number of particles (N), pressure (P) and temperature (T) ensemble combines thermostats and barostats to maintain pressure, by attaching them to a pressure-bath or piston, and temperature within the sample system, again to more closely match certain experimental conditions which are not in isolated systems. They combine a thermostat (§2.4.7) and a barostat (§2.4.8) to sample these states.

2.3 Phase Space

Phase space describes the entire state of a system at any given time, it is often a $6N$-dimensional space consisting of the positions and momenta of the particles involved, but can be expanded or contracted as necessary. A generic phase-space vector might be written as:

$$\mathbf{x} = (\{\mathbf{q}\}, \{\mathbf{p}\}), \tag{2.2}$$

$$\mathbf{x} = (\mathbf{q}_1, \ldots, \mathbf{q}_N, \mathbf{p}_1, \ldots, \mathbf{p}_N), \tag{2.3}$$

$$\mathbf{x} = (q_1, \ldots, q_{3N}, p_1, \ldots, p_{3N}), \tag{2.4}$$

where q is the generalised position coordinate, p is the generalised momentum coordinate, curly braces describe the entire set of the properties.

An example of an extended phase space would be for the purpose of variable cell calculations as follows:

$$\mathbf{x} = (\{\mathbf{h}\}, \{\mathbf{h}_v\}, \{\mathbf{q}\}, \{\mathbf{p}\}), \tag{2.5}$$

where h is the set of cell vectors and h_v is the set of cell vector momenta.

As mentioned above, phase space describes the entire state of the system at any given time. Hence it is really through phase space which we are progressing when we perform a molecular dynamics calculation, and so in a molecular dynamics calculation, we are tracing a path or trajectory through phase space and can describe any point in the trajectory by the following phase-space vector:

$$\mathbf{x}(t) = (\mathbf{q}_1(t), \ldots, \mathbf{q}_N(t), \mathbf{p}_1(t), \ldots, \mathbf{p}_N(t)) \tag{2.6}$$

The entire phase space is often denoted as either Γ or Ω.

2.4 Integrators

The choice of how we translate the infinitely precise derivatives of mathematics into a numerical approximation for us to simulate on a computer makes a large difference to the feasibility of our calculations to represent real systems.

In order for an integrator to be considered a reasonable approximation to the system, we establish 4 key criteria: stability, accuracy, ergodicity and symplecticity, which are defined below.

Most finite difference integrator schemes are derived from a Taylor's expansion (Eq. 2.7) of a derivative to a certain order, and then solved for the desired

order.

$$\mathbf{r}_i(t+\Delta t) \approx \mathbf{r}_i(t) + \frac{1}{1!}\Delta t \left.\frac{\partial \mathbf{r}_i}{\partial t}\right|_t + \frac{1}{2!}\Delta t^2 \left.\frac{\partial^2 \mathbf{r}_i}{\partial t^2}\right|_t + \frac{1}{3!}\Delta t^3 \left.\frac{\partial^3 \mathbf{r}_i}{\partial t^3}\right|_t + \mathscr{O}\left(\Delta t^4\right) + \ldots, \quad (2.7)$$

where $\mathscr{O}(N)$ refers to the rate of propagation of error in the system.

There are many finite difference schemes including Euler integrators, Runge-Kutta integrators and Verlet Integrators, depending on the number of dependants and the desired accuracy.

The most common finite integrator scheme used in MD calculations is the velocity Verlet integrator [Swope *et al.*, 1982], which is a two-step, second-order integrator, which splits the integration through phase space about the following scheme:

$$r(t+\Delta t) = r(t) + v(t)\,\Delta t + \frac{F(t)}{2m}\Delta t^2 + \mathscr{O}\left(\Delta t^4\right), \quad (2.8)$$

$$v(t+\Delta t) = v(t) + \frac{F(t+\Delta t) + F(t)}{2m}\Delta t + \mathscr{O}\left(\Delta t^2\right), \quad (2.9)$$

which, to integrate numerically, we split in two, giving:

$$r(t+\Delta t) \simeq r(t) + v(t)\,\Delta t + \frac{F(t)}{2m}\Delta t^2, \quad (2.10)$$

$$v\left(t+\tfrac{\Delta t}{2}\right) \simeq v(t) + \frac{F(t)}{2m}\Delta t, \quad (2.11)$$

$$F(t+\Delta t) \simeq -\nabla U(r_1(t+\Delta t), \ldots, r_N(t+\Delta t)), \quad (2.12)$$

$$v(t+\Delta t) \simeq v\left(t+\tfrac{\Delta t}{2}\right) + \frac{F(t+\Delta t)}{2m}\Delta t, \quad (2.13)$$

which we call the velocity Verlet integrator.

The order in which we update these variables and how we choose to split is important for time-reversibility [Hoover *et al.*, 1996] and symplecticity Tuckerman *et al.* [1992] concerns. Ensuring these two things are preserved results in a reduced drift in the conserved quantities of the system, and hence a reduced error in our calculations.

2.4.1 Hamiltonian Formulation

Hamilton's equations describe how the Hamiltonian can be used to derive equations of motion (EoM) for a system. Starting from a classical Hamiltonian

for a set of phase-space coordinates $\mathbf{x} = (\{\mathbf{q}\}, \{\mathbf{p}\})$:

$$\mathscr{H} = \sum_{i=1}^{N} \frac{\mathbf{p}_i^2}{2m} + U(\mathbf{q}_1, \ldots, \mathbf{q}_N), \tag{2.14}$$

the evolution of the system with respect to these coordinates is:

$$\frac{\partial \mathbf{p}}{\partial t} = -\frac{\partial \mathscr{H}}{\partial \mathbf{q}}, \tag{2.15}$$

$$\frac{\partial \mathbf{q}}{\partial t} = \frac{\partial \mathscr{H}}{\partial \mathbf{p}}. \tag{2.16}$$

Given our definition of the Hamiltonian (Eq. 2.14), and substituting in Eqs. 2.15 and 2.16, we find:

$$\frac{\partial \mathbf{p}}{\partial t} = -\nabla U(\mathbf{q}_1, \ldots, \mathbf{q}_N) \qquad \text{and} \tag{2.17}$$

$$\frac{\partial \mathbf{q}}{\partial t} = \frac{\mathbf{p}_i}{m}, \tag{2.18}$$

which correspond to the time-evolution equations of an NVE ensemble with no external work.

In the case of a Hamiltonian which describes an extended space with additional canonical coordinates (See: Appendix A and Appendix B), the same rules apply provided the coordinate dependencies are uncorrelated.

2.4.2 Liouvillian Formulation

While Hamilton's equations give us the set of equations which we need to evolve through time to explore our ensemble, the order of integration of the non-commutative differential operators leads to several possible solutions to Hamilton's equations, not all of which lead to dynamics which obey the integrator criteria (described in detail §2.4.3).

It was shown by Tuckerman *et al*. [1992] that it was possible to prove the conservation of several phase-space properties by applying schemes similar to those used in path-integral quantum mechanics [Feynman and Hibbs, 1965] and constructing an integrator based on a Liouvillian formulation. The Liouvillian can be seen as a classical analogue to the Heisenberg operators in the Heisenberg picture of quantum mechanics. Essentially, the Liouville operator propagates a classical phase-space vector through time.

For a classical Hamiltonian (Eq. 2.14), we assume that the time evolution of

the state $\mathbf{x} = (\{\mathbf{q}\}, \{\mathbf{p}\})$ is given by:

$$\frac{\mathrm{d}\mathbf{x}}{\mathrm{d}t} = \sum_{i=1}^{3N} \left(\frac{\partial \mathbf{x}}{\partial q_i} \dot{q}_i + \frac{\partial \mathbf{x}}{\partial p_i} \dot{p}_i \right), \tag{2.19}$$

which substituting in Hamilton's equations (Eqs. 2.15 & 2.16), we find:

$$\frac{\mathrm{d}\mathbf{x}}{\mathrm{d}t} = \sum_{i=1}^{3N} \left(\frac{\partial \mathbf{x}}{\partial q_i} \frac{\partial \mathscr{H}}{\partial p_i} - \frac{\partial \mathbf{x}}{\partial p_i} \frac{\partial \mathscr{H}}{\partial q_i} \right), \tag{2.20}$$

which has the form of a Poisson bracket:

$$\frac{\mathrm{d}\mathbf{x}}{\mathrm{d}t} = \{\mathbf{x}, \mathscr{H}\}. \tag{2.21}$$

Taking this Poisson bracket as an operator we call $i\mathscr{L}$, this can be applied to the phase-space state to propagate the system through time, which we can also present as a differential operator:

$$i\mathscr{L}\mathbf{x} \equiv \{\mathbf{x}, \mathscr{H}\} \equiv \frac{\mathrm{d}\mathbf{x}}{\mathrm{d}t} \equiv \sum_{i=1}^{3N} \left(\frac{\partial \mathscr{H}}{\partial p_i} \frac{\partial}{\partial q_i} - \frac{\partial \mathscr{H}}{\partial q_i} \frac{\partial}{\partial p_i} \right) \mathbf{x}, \tag{2.22}$$

it can then be shown that since $\frac{\mathrm{d}\mathbf{x}}{\mathrm{d}t} = i\mathscr{L}\mathbf{x}$

$$\mathbf{x}(t) = \exp(i\mathscr{L}t)\,\mathbf{x}(0). \tag{2.23}$$

Further to this it can be seen that, in this case, this Liouvillian operator is the application of two distinct elements:

$$i\mathscr{L} = i\mathscr{L}_1 + i\mathscr{L}_2, \tag{2.24}$$

$$i\mathscr{L}_1 = \sum_{i=1}^{3N} \frac{\partial \mathscr{H}}{\partial p_i} \frac{\partial}{\partial q_i}, \tag{2.25}$$

$$i\mathscr{L}_2 = \sum_{i=1}^{3N} -\frac{\partial \mathscr{H}}{\partial q_i} \frac{\partial}{\partial p_i}. \tag{2.26}$$

Due to the non-commutative nature of derivative operators, the splitting is not so simple as replacing the single Liouvillian with the individual elements, and so we must employ a Trotter factorisation [Trotter, 1959]. Trotter's theorem states that any two non-commuting operators can be separated according to:

$$\exp(A+B) = \lim_{P\to\infty} \left(\exp\left(\frac{B}{2P}\right) \exp\left(\frac{A}{P}\right) \exp\left(\frac{B}{2P}\right) \right)^P. \tag{2.27}$$

Applying this to Eqs. 2.23 and 2.24, we can find that:

$$\exp((i\mathscr{L}_1 + i\mathscr{L}_2)t) = \lim_{P\to\infty}\left(\exp\left(\frac{i\mathscr{L}_2 t}{2P}\right)\exp\left(\frac{i\mathscr{L}_1 t}{P}\right)\exp\left(\frac{i\mathscr{L}_2 t}{2P}\right)\right)^P. \tag{2.28}$$

Introducing to this a discrete time integral wherein $\Delta t \Rightarrow \frac{t}{P}$, we find:

$$\exp(i\mathscr{L}t) = \lim_{P\to\infty,\Delta t\to 0}\left(\exp\left(i\mathscr{L}_2\tfrac{\Delta t}{2}\right)\exp(i\mathscr{L}_1\Delta t)\exp\left(i\mathscr{L}_2\tfrac{\Delta t}{2}\right)\right)^P, \tag{2.29}$$

which if we take the P^{th} root of both sides, we find:

$$\exp\left(i\mathscr{L}\tfrac{t}{P}\right) = \exp(i\mathscr{L}\Delta t) \approx \left(\exp\left(i\mathscr{L}_2\tfrac{\Delta t}{2}\right)\exp(i\mathscr{L}_1\Delta t)\exp\left(i\mathscr{L}_2\tfrac{\Delta t}{2}\right)\right), \tag{2.30}$$

which, if we apply this to the phase-space vector, we arrive at a time-reversible and symplectic velocity Verlet integrator as in Eq. 2.13.

2.4.3 Stability

Stability is the property of a finite integrator to be able to remain convergent towards the correct answer even with finite errors in the calculation of forces, and its resilience to extreme conditions or step-lengths. An unstable integrator may rapidly diverge to infinity if certain conditions are met, such as an overly long time-step.

One key method of numerically establishing the stability of a particular algorithm is to use von Neumann stability analysis [Faul, 2016]. This calculation finds the bounds of stability such that any error is not divergent within a given domain of integration.

Assuming that a general numerical admits a solution in the form of a wave such as:

$$r(n\Delta t) = a^n(\omega)\exp(i\omega\Delta t), \tag{2.31}$$

where a is a Fourier component describing error noise, ω is an angular frequency and i is $\sqrt{-1}$. The amplification factor is defined as growth of a at each successive step and is defined as:

$$G(\omega) = \frac{a^{n+1}(\omega)}{a^n(\omega)}. \tag{2.32}$$

The von Neumann stability condition holds whenever the error does not diverge, i.e.:

$$\|G(\omega)\| \leq 1. \tag{2.33}$$

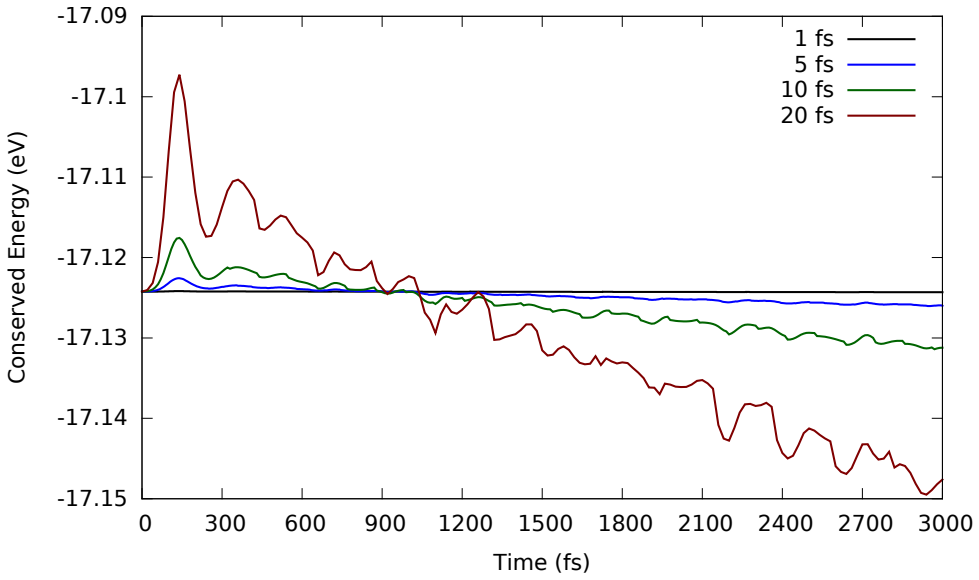

Figure 2.1: Energy conservation and drift in a 512-atom Lennard-Jones NVE calculation initialised at 80K in perfect FCC crystal for different time-step lengths.

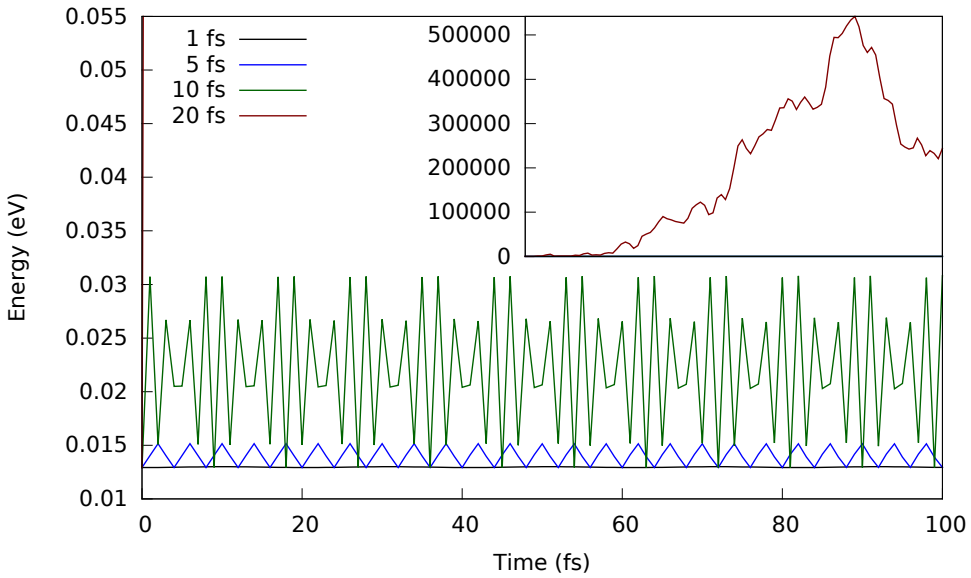

Figure 2.2: Critical instability in energy conservation for a NVE SHO calculation for different time-step lengths. The inset shows the same plot for the $20fs$ time-step system which diverges rapidly from physical solution.

Another key factor in stability of a molecular dynamics calculation is that the dynamics of the system are able to be captured by the chosen time-step. If the time-step chosen is too large, it means that the system can gain or lose energy. Take, for instance, the case of the simple harmonic oscillator. A step which is too large will cause the velocity inversion at a point beyond the point where it should have inverted. This injects energy into the system at each time-step resulting in a divergent calculation (Fig. 2.2).

2.4.4 Accuracy

Accuracy describes the tendency of an integrator to accumulate error due to the fact it is taking finite steps in an infinitesimal space. Usually the accuracy of an integrator is determined by the order at which the expansion is truncated (with cancellations).

If we consider the error to be a random deviation about the correct answer, i.e.:

$$A = \bar{A} + \varepsilon, \tag{2.34}$$

where A is the computed answer, $\bar{A}$ is the correct answer and ε is the error (in the case of velocity Verlet $\mathscr{O}(\Delta t^4)$), therefore as we integrate our equation of motion:

$$r(t+\Delta t) = r(t) + v(t)\,\Delta t + \frac{F(t)}{2m}\Delta t^2 + \mathscr{O}\left(\Delta t^4\right), \tag{2.35}$$

$$r(t+2\Delta t) = 2\big(r(t+\Delta t) + \mathscr{O}\left(\Delta t^4\right)\big) - r(t) + \frac{F(t)}{2m}\Delta t^2 + \mathscr{O}\left(\Delta t^4\right), \tag{2.36}$$

$$r(t+2\Delta t) = 2r(t+\Delta t) - r(t) + \frac{F(t)}{2m}\Delta t^2 + 3\mathscr{O}\left(\Delta t^4\right), \tag{2.37}$$

likewise the accumulated error for $r(t+3\Delta t) = 6\mathscr{O}\left(\Delta t^4\right)$, $r(t+4\Delta t) = 10\mathscr{O}\left(\Delta t^4\right)$ and so on, such that:

$$r(t+n\Delta t) = \bar{r}(t+n\Delta t) + \frac{n(n+1)}{2}\mathscr{O}\left(\Delta t^4\right), \tag{2.38}$$

substituting $T = n\Delta t$ and expanding:

$$r(t+T) = \bar{r}(t+T) + \left(\frac{T^2}{2\Delta t^2} + \frac{T}{2\Delta t}\right)\mathscr{O}\left(\Delta t^4\right) \tag{2.39}$$

which by cancellation gives us the global error of $\mathscr{O}\left(\Delta t^2\right)$, for a cost only fractionally more than the first order Euler expansion [Frenkel and Smit, 1996]. Though there many higher-order integration schemes exist and can be de-

rived, the relative gain in permitted time-step versus the cost of calculation often renders them inefficient compared to more steps of a simpler integrator [Berendsen and van Gunsteren, 1986].

2.4.5 Ergodicity

The ergodic hypothesis describes that for a molecular dynamics simulation of an isolated system to adequately describe a system, that the long-time average of an instantaneous property should equal the ensemble average of said property [Tuckerman, 2010].

$$\bar{X} = \lim_{t\to\infty} \frac{1}{t} \int_{t_0}^{t_0+t} X(r,t')\, dt' = \frac{1}{N} \sum_{i=1}^{N} X[\mathbf{x}_{i\Delta t}] = \langle X(r) \rangle \,, \tag{2.40}$$

where X is some system observable, t is time, N is the number of time-steps, $\mathbf{x}$ is a phase-space vector.

In other words, ergodicity is whether, given infinite time, the ensemble will explore all of phase space with the correct probability.

2.4.6 Symplecticity

Symplecticity, otherwise known as phase-space incompressibility, describes whether the system will preserve the volume of the domain of phase-space explored at any given time. If we consider the phase space vector:

$$\mathbf{x} = (q_1, \ldots, q_{3N}, p_1, \ldots, p_{3N}) \,, \tag{2.41}$$

and its propagation through phase space:

$$\dot{\mathbf{x}} = \left(\frac{\partial \mathscr{H}}{\partial q_1}, \ldots, \frac{\partial \mathscr{H}}{\partial q_{3N}}, \frac{\partial \mathscr{H}}{\partial p_1}, \ldots, \frac{\partial \mathscr{H}}{\partial p_{3N}} \right) , \tag{2.42}$$

then we must be able to show that a given "flow" (time evolution) through phase space, is incompressible. In analogy to fluid dynamics where the divergence of the flow must be zero ($\nabla \cdot \mathbf{v}(\mathbf{r}) = 0$), so it must be for our phase space flow, i.e:

$$\nabla_{\mathbf{x}} \cdot \dot{\mathbf{x}}(\mathbf{x}) = 0. \tag{2.43}$$

As it is known that the true propagation of the Hamiltonian equations for an infinitesimal integration is symplectic, then if an integrator is not symplectic it can be shown that: if the system does not map to the true Hamiltonian prop-

agation as $\Delta t \to 0$, it cannot be a true sampling. For non-Hamiltonian integrators, however, this cannot be shown exactly, but through Liouville's theorem it can be shown that a minimal requirement for non-Hamiltonian systems is that they must conserve a weighted phase-space volume [Tuckerman *et al.*, 1999].

2.4.7 Thermostats

Thermostats are a means of controlling the temperature in an MD simulation. There are many approaches to thermostats, each with their own benefits and drawbacks, and the appropriate tool should be chosen for the job at hand. For a more detailed review of thermostats, see Tuckerman [2010].

2.4.7.1 Berendsen

The Berendsen thermostat [Berendsen *et al.*, 1984] is a thermostat which forces the system to be at the target temperature by re-scaling the velocities of the particles such the kinetic energy of the system is that of the target temperature.

Due to the fact that it is just a direct scaling, it does not produce the correct ensemble or the Maxwell-Boltzmann distribution as desired. This makes it unsuitable for most statistical purposes, but it is commonly used as a means of rapidly equilibrating (§2.1) a system to the desired temperature in a physically reasoned way.

The EoM that govern the Berendsen thermostat are:

$$\dot{\mathbf{r}}_i = \frac{\mathbf{p}_i}{m_i}, \tag{2.44}$$

$$\dot{\mathbf{p}}_i = \mathbf{F}_i + \frac{1}{2\tau}\left(\frac{T_{\text{target}}}{T(t)} - 1\right)\mathbf{p}_i, \tag{2.45}$$

where τ is a relaxation time which governs how quickly the current temperature ($T(t)$) converges to the target temperature (T_{target}).

2.4.7.2 Langevin

The Langevin thermostat [Langevin, 1908] is a thermostat based on the idea of the system containing a gas of fictitious particles held at a fixed temperature, colliding with the sample material, as in Brownian motion. It is possible through a branch of stochastic calculus called Itō calculus to prove the ergodic nature of the Langevin term (see Leimkuhler *et al.* [2009] and references therein). However, it is also possible to see by inspection that the infinite Gaus-

sian tails of the random numbers (Eq. 2.47) should, given infinite time, push a system out of any given well of stability, allowing the Langevin thermostat to explore all of phase space.

The Langevin thermostat is made up of two parts, the fluctuation term, which provides normally-distributed "kicks" in random directions to each of the particles in the system, and a damping term, which applies a velocity-dependent drag to the particles to maintain a semi-stable total energy. The approach can be shown, using the fluctuation-dissipation theorem to result in the ensemble average temperature being the target temperature [Kubo, 1966].

The EoM that govern the Langevin thermostat are:

$$\dot{\mathbf{r}}_i = \frac{\mathbf{p}_i}{m_i}, \tag{2.46}$$

$$\dot{\mathbf{p}}_i = \mathbf{F}_i - \underbrace{\gamma \mathbf{p}_i}_{\text{Damping Term}} + \underbrace{\sqrt{\frac{2 m_i k_B T \gamma}{\Delta t}} \mathbf{N}(0,1)}_{\text{Fluctuation}}, \tag{2.47}$$

where γ is a coupling constant which determines the decorrelation time of the system, i.e. the time over which the velocities of the particles may be considered no longer correlated, and $\mathbf{N}(0,1)$ is a vector of normally distributed random numbers according to the definition of $N(0,1)$.

The choice of γ is important as a coupling which is too large (coupled too strongly) will cause the system to undergo Brownian dynamics (or random walk), a gamma which is too small (coupled too weakly) will result in near NVE dynamics, with little control on the temperature. A common means of determining an ideal time-step is to ensure that the time-step does not exceed the lowest period (highest frequency) modes (§2.5.8).

2.4.7.3 Nosé-Hoover

The Nosé-Hoover thermostat [Hoover, 1985] is a set of equations, derived as an extension by Hoover of Nosé's extended Hamiltonian system (See Nosé [1984] and Appendix A). It is designed to control the temperature of an enclosed system by means of a fictitious, frictional fluid in which the particles are suspended, called the heat bath. The frictional force of this fluid is determined by the deviation of the system's instantaneous temperature from the target temperature.

The Nosé-Hoover thermostat is entirely deterministic, and relatively simple to implement, but unfortunately, it can be proven that the system is not ergodic for simple cases such as the simple harmonic oscillator (Fig. 2.4)

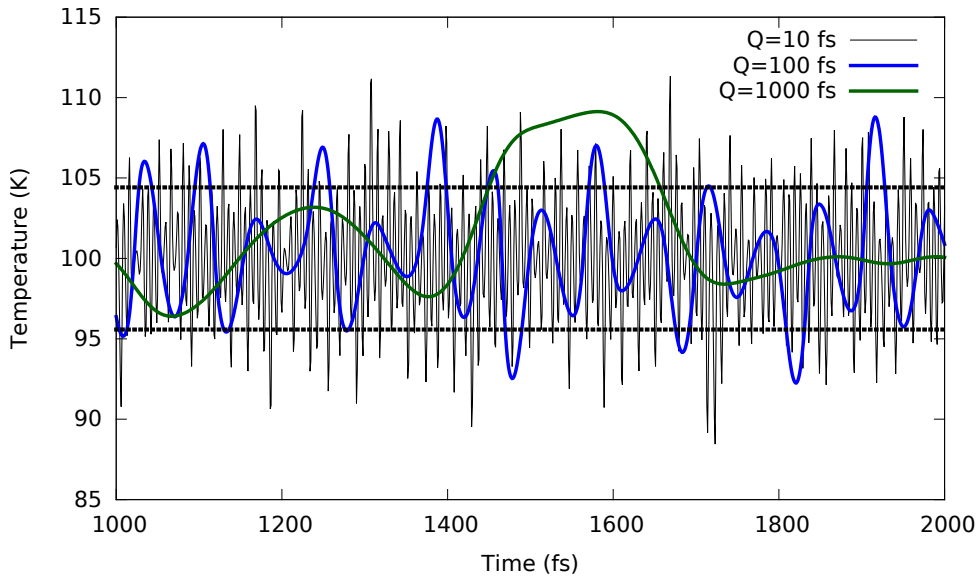

Figure 2.3: Effect of the choice of Q on the temperature dynamics of an NVT simulation for a 512-atom Lennard-Jones system at a $100K$ target. Also labelled are the expected fluctuations based on $\Delta T = \frac{T}{\sqrt{N}}$

The EoM governing the Nosé-Hoover thermostat are:

$$\dot{\mathbf{r}}_i = \frac{\mathbf{p}_i}{m_i}, \tag{2.48}$$

$$\dot{\mathbf{p}}_i = \mathbf{F}_i - \frac{\eta}{Q}\mathbf{p_i}, \tag{2.49}$$

$$\dot{\eta} = \frac{p_\eta}{Q}, \tag{2.50}$$

$$\dot{p_\eta} = \sum_{i=1}^{N} \frac{\mathbf{p}_i^2}{m_i} - dNk_BT, \tag{2.51}$$

where T is the target temperature, η is the frictional coefficient of the thermostat, p_η is a fictitious "momentum" of the thermostat, Q is a fictitious "mass" of the thermostat and determines the coupling of the heat bath to the system, d is the dimensionality of the system, N is the number of particles in the system, which together form the number of degrees of freedom in the system.

The choice of Q is important to the dynamics of the system and the rate of equilibration to the correct temperature. The choice of optimal Q is outlined in Nosé [1991], which suggests that the best approach is to treat the coupling as a harmonic oscillator bound in resonance to a mode of the system. A characteristic mode of the system can be found from a strong peak in the phononic density of states (§2.5.8). Though the ensemble average may be correct with a sub-optimal choice of Q, the temperature fluctuation may result in unphysical dynamics (Fig. 2.3).

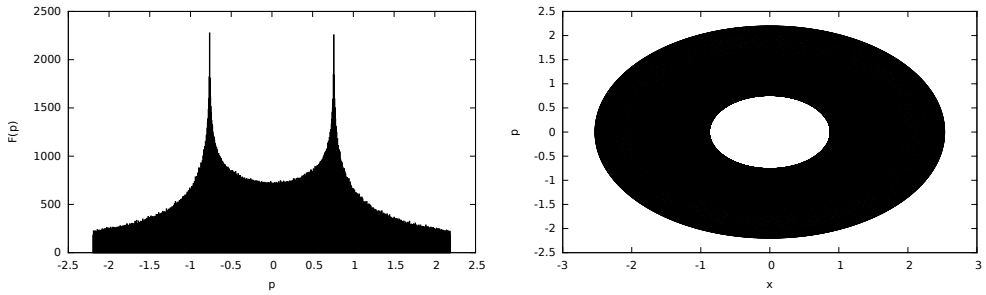

Figure 2.4: The histogram of velocities (Left) and phase space plot of the Nosé-Hoover thermostat (Right) for a simple harmonic oscillator. The correct ergodic exploration traces a Gaussian distribution of velocities and a 2-D Gaussian density of points centred on zero in phase space [Tuckerman, 2010]. Instead in the Nosé-Hoover scheme we find a strongly bimodal distribution of velocities and a ring of explored phase space, whose diameter and annular breadth changes with temperature.

2.4.7.4 Nosé-Hoover-Chains

Nosé-Hoover-Chains [Martyna *et al.*, 1992] are an attempt to overcome the non-ergodic limitations of the Nosé-Hoover thermostat in the simple case by coupling the thermostat to a chain of thermostats, each thermostatted by its predecessor in the chain. In principle, this solves the ergodicity problem in the infinite chain limit. Given the finite limitations of a computer it is generally accepted that fewer chains reduce the non-ergodicity sufficiently for calculations, even with limits as low as 2 chains.

The EoM governing Nosé-Hoover-Chains are:

$$\dot{\mathbf{r}}_i = \frac{\mathbf{p}_i}{m_i}, \tag{2.52}$$

$$\dot{\mathbf{p}}_i = \mathbf{F}_i - \frac{p_{\eta_1}}{Q_1}\mathbf{p_i}, \tag{2.53}$$

$$\dot{\eta}_j = \frac{p_{\eta_j}}{Q_j} \qquad j = 1,\ldots,M, \tag{2.54}$$

$$\dot{p}_{\eta_1} = \left(\sum_{i=1}^{N}\frac{\mathbf{p}_i^2}{m_i} - dNk_BT\right) - \frac{p_{\eta_2}}{Q_2}p_{\eta_1}, \tag{2.55}$$

$$\dot{p}_{\eta_j} = \left(\frac{p_{\eta_{j-1}}^2}{Q_{j-1}} - k_BT\right) - \frac{p_{\eta_{j+1}}}{Q_{j+1}}p_{\eta_j} \qquad j = 2,\ldots,M-1, \tag{2.56}$$

$$\dot{p}_{\eta_M} = \left(\frac{p_{\eta_{M-1}}^2}{Q_{M-1}} - k_BT\right), \tag{2.57}$$

where T is the target temperature, η is the frictional coefficient of the thermostat, p_η is a fictitious "momentum" of the thermostat, Q is a fictitious "mass" of the thermostat and determines the coupling of the heat bath to the system, d

is the dimensionality of the system, N is the number of particles in the system, which together form the number of degrees of freedom in the system, M is the total number of thermostats in the chain. Properties of the j^{th} thermostat are denoted by a subscript.

Again the choice of the Qs is essential for the reproduction of the dynamics of a real system. Martyna *et al*. [1992] suggests using:

$$\begin{aligned} Q_1 &= dNkT\tau^2, \\ Q_j &= kT\tau^2, \qquad j = 2,\ldots,M, \end{aligned} \tag{2.58}$$

where τ is some fundamental time-scale which can be estimated from strong phonon modes. As a general rule of thumb however $\tau \geq 20\Delta t$ is usually reasonable.

2.4.7.5 Nosé-Hoover-Langevin

Nosé-Hoover-Langevin [Leimkuhler *et al*., 2009] is a scheme which combines the deterministic nature of Nosé-Hoover, but solves the ergodicity problem by introducing a slight perturbation in the form of a Langevin style integrator thermostatting the heat bath.

The EoM that govern the Nosé-Hoover-Langevin thermostat are:

$$\dot{\mathbf{r}}_i = \frac{\mathbf{p}_i}{m_i}, \tag{2.59}$$

$$\dot{\mathbf{p}}_i = \mathbf{F}_i - \eta\mathbf{p_i}, \tag{2.60}$$

$$\dot{\eta} = \frac{p_\eta}{Q}, \tag{2.61}$$

$$\dot{p}_\eta = \frac{1}{Q}\left(\sum_{i=1}^{N}\frac{\mathbf{p}_i^2}{m_i} - dNk_BT\right) - \underbrace{\exp\left(-\tfrac{\Delta t}{\sigma}\right)p_\eta}_{\text{Damping Term}} + \underbrace{\sqrt{\frac{k_BT}{Q}\left(1-\exp\left(-\tfrac{2\Delta t}{\sigma}\right)\right)}N(0,1)}_{\text{Fluctuation}}, \tag{2.62}$$

where T is the target temperature, η is the frictional coefficient of the thermostat, p_η is a fictitious "momentum" of the thermostat, Q is a fictitious "mass" of the thermostat and determines the coupling of the heat bath to the system, σ is a coupling constant which determines the decorrelation time of the thermostat, d is the dimensionality of the system, N is the number of particles in the system, which together form the number of degrees of freedom in the system.

2.4.8 Barostats

In systems where the pressure is controlled, we need a way to drive the pressure to a desired value. Following the ideal gas law:

$$PV = Nk_BT, \tag{2.63}$$

we control the pressure by mediating the volume of our system. This is done through a re-scaling of the cell vectors ($\underline{\underline{\mathbf{h}}}$), either independently or dependently, and subsequent properties such as particle positions and velocities. There are different approaches as to how the cell should be re-scaled, some of which are discussed below, but for a full review see Tuckerman [2010].

2.4.8.1 Berendsen

The Berendsen barostat [Berendsen *et al.*, 1984] is a similar scheme to the Berendsen thermostat in that it is a mechanism to force the system to the desired pressure in a given time. It can be shown that:

$$\frac{\partial P(t)}{\partial t} = \frac{P - P(t)}{\tau_P}, \tag{2.64}$$

where P is the target pressure, τ_P is a relaxation time which scales the rate of convergence to the target pressure.

To this end the cell volume is isotropically re-scaled according to a factor given by:

$$\eta(t) = 1 - \frac{\Delta t}{\tau_P}\gamma(P - P(t))\,. \tag{2.65}$$

2.4.8.2 Andersen

The Andersen barostat [Andersen, 1980] is an extended Hamiltonian technique (See Appendix B), similar in principle of the Nosé-Hoover style thermostats, which treats the cell volume as another coordinate, as though the system is acted upon by a piston.

The EoM that govern the isotropic Andersen barostat are:

$$\dot{\mathbf{r}}_i = \frac{\mathbf{p}_i}{m_i} + \frac{\dot{V}}{3V}\mathbf{r}_i, \tag{2.66}$$

$$\dot{\mathbf{p}}_i = \mathbf{F}_i - \frac{\dot{V}}{3V}\mathbf{p}_i, \tag{2.67}$$

$$\dot{V} = \frac{p_V}{W}, \tag{2.68}$$

$$\dot{p}_V = \frac{1}{3V}\underbrace{\sum_{i=1}^{N}\left(\frac{\mathbf{p}_i^2}{m_i} - \mathbf{F}_i \cdot \mathbf{r}_i\right)}_{P(t)} - P, \tag{2.69}$$

where V is the volume, p_V is the "velocity" of the barostat, P is the target pressure, W is the coupling factor which controls the stiffness or mass of the piston, and hence the barostat rate.

It should be noted that it is possible to implement anisotropic compression by replacing P with a particular component of the pressure and $V^{\frac{1}{3}}$ with the length of the corresponding cell vector.

2.4.9 Hugoniostats

2.4.9.1 NVHug Nosé-Hoover

The uniaxial Hugoniostat was first described in Maillet *et al*. [2000] and is a constant volume approach to the Hugoniostat problem which uses a style of Nosé-Hoover integrator in order to drive the temperature of the system to the Hugoniot.

The EoM that govern the Nosé-Hoover NVHug are:

$$\dot{\mathbf{r}}_i = \frac{\mathbf{p}_i}{m_i}, \tag{2.70}$$

$$\dot{\mathbf{p}}_i = \mathbf{F}_i - \nu\chi\mathbf{p}_i, \tag{2.71}$$

$$\dot{\chi} = \frac{\nu}{C}(E(t) - E_H(t)), \tag{2.72}$$

where χ is the heat-flow of the thermostat into the system, ν is the coupling between the thermostat and the system, C is a scaling constant in units of energy to conserve system size independence and

$$E_H(t) = E(t_0) + \tfrac{1}{2}(P(t) + P(t_0))(V(t_0) - V(t)), \tag{2.73}$$

where t_0 is the time before the system has been compressed (i.e. the equilibrium state), we deem the deviation of our current state from the Hugoniot state

the Hugoniot estimator:

$$E(t) - E_H(t) = E(t) - E(t_0) - \tfrac{1}{2}(P(t) + P(t_0))(V(t_0) - V(t)\,). \tag{2.74}$$

2.4.9.2 NVHug Langevin

A scheme for a Langevin-based Hugoniostat was given in Maillet and Stoltz [2008] using the temperature as a dynamical variable throughout the calculation (notation taken directly from Maillet and Stoltz [2008]):

$$\mathrm{d}\mathbf{q}_t = \underline{\underline{\mathbf{M}}}^{-1}\mathbf{p}_t\ \mathrm{d}t, \tag{2.75}$$

$$\mathrm{d}\mathbf{p}_t = -\nabla V(\mathbf{q}_t)\ \mathrm{d}t - \xi\underline{\underline{\mathbf{M}}}^{-1}\mathbf{p}_t\ \mathrm{d}t + \sqrt{2\xi k_B T_t}\ \mathrm{d}W_t, \tag{2.76}$$

$$\mathrm{d}T_t = -\nu\frac{A(\mathbf{q}_t,\mathbf{p}_t)}{A_{ref}}T_{ref}\ \mathrm{d}t, \tag{2.77}$$

where A is the Hugoniot estimator (Eq. 2.74); $\underline{\underline{\mathbf{M}}}$ is a mass matrix; ξ is the Langevin coupling; ν is the temperature coupling which determines the rate of convergence of the target temperature (T_t) to the Hugoniot temperature; $\mathrm{d}W_t$ is a Wiener process which is analogous to a normally-distributed, time-progressive Brownian motion; A_{ref} and T_{ref} are reference values to scale properties to retain system independence.

The suggested scheme involved building a dynamical sampling of the configuration space from previous exploration of the system by the trajectory. This is done by creating a histogram of the expectation value of the observable A at given temperature distributions and thus attempting to drive the temperature to that of the correct expectation value for the Hugoniot.

The time-discretised form of the above equations is:

$$v\big(t+\tfrac{\Delta t}{2}\big) = v(t) + \frac{1}{2}\Delta t\left(F(t) - \xi v(t) + \frac{1}{2}\sqrt{2\xi\Delta t k_B T(t)}N(0,1)\right), \tag{2.78}$$

$$r(t+\Delta t) = r(t) + v\big(t+\tfrac{\Delta t}{2}\big)\,\Delta t, \tag{2.79}$$

$$F(t+\Delta t) = -\nabla V(\,r(t+\Delta t)\,), \tag{2.80}$$

$$v(t+\Delta t) = \left(1+\frac{\xi\Delta t}{2}\right)^{-1}\left(v\big(t+\tfrac{\Delta t}{2}\big) + \frac{F(t+\Delta t)}{2m}\Delta t + \frac{1}{2}\sqrt{2\xi\Delta t k_B T(t)}N(0,1)\right), \tag{2.81}$$

$$T(t+\Delta t) = T(t) - \left(\frac{\sum_{m=0}^{n} E_H(m\Delta t)\,\chi_{\Delta T}(T(m\Delta t) - T(t)\,)}{\sum_{m=0}^{n}\chi_{\Delta T}(T(m\Delta t) - T(t)\,)}\right)\nu\Delta t, \tag{2.82}$$

$\chi_{\Delta T}$ is analogous to a discretised Dirac delta distribution which is defined as:

$$\chi_{\Delta T} = \begin{cases} \frac{1}{\Delta T} & \text{when } T^m \text{ and } T^n \text{ lie in the same bin,} \\ 0 & \text{otherwise.} \end{cases} \tag{2.83}$$

The reason for this is to perform a weighted average, meaning that narrower bins, should they not be evenly distributed, lead to a more significant contribution to the average.

2.4.9.3 NPHug Nosé-Hoover

The uniaxial Hugoniostat was described initially as an instantaneous compression to the shocked volume, followed by a thermal relaxation to the Hugoniot state, but it was later suggested [Ravelo *et al.*, 2004] that a steady compression reduces the transient and leads to a faster convergence, as such the ideas of NPT dynamics (§2.4.8) were adapted to fit into the Hugoniostat formulation.

The EoM that govern the Nosé-Hoover NPHug Hugoniostat are:

$$\dot{r}_{\alpha i} = \frac{p_{\alpha i}}{m_i} + \nu_P \eta_\alpha r_{\alpha i}, \tag{2.84}$$

$$\dot{p}_{\alpha i} = F_{\alpha i} - (\nu_p \eta_\alpha - \nu_H \chi)\, p_{\alpha i}, \tag{2.85}$$

$$\dot{h}_{\alpha\alpha} = \nu_p \eta_\alpha h_{\alpha\alpha}, \tag{2.86}$$

$$\dot{\chi} = \frac{\nu_H}{C}(E(t) - E_H(t))\,, \tag{2.87}$$

$$\dot{\eta}_\alpha = \frac{\nu_p}{D}(P_{\alpha\alpha}(t) - \sigma_{\alpha\alpha})\,, \tag{2.88}$$

where α refers to an element in the direction of a cell-vector $\mathbf{h}$, ν_H is the coupling of the thermostat to the system, ν_P is the coupling of the barostat piston to the system, $\underline{\underline{\sigma}}$ is the target pressure tensor and P is the instantaneous total pressure tensor, D is a scaling constant in units of pressure to conserve system size independence, Ravelo *et al.* [2004] suggest the equilibrium bulk modulus (B_0, §2.5.5) .

2.5 Simulation Measurements

2.5.1 Energy

For empirical potential calculations, the potential energy is defined by some function (§3.1), and so the calculation of the total potential energy (for a pair-

potential between two atoms) is trivially described by:

$$U = \sum_{i<j} V_{PP}(\mathbf{r}_{ij}) \,. \tag{2.89}$$

this can be extended for other possible potentials according to their functional form.

The kinetic energy can be calculated directly from the velocities and masses of particles involve for both *ab initio* or pair-potential calculations.

$$\mathscr{K} = \frac{1}{2} \sum_{i=1}^{N} m_i (\mathbf{v}_i \cdot \mathbf{v}_i) \,, \tag{2.90}$$

where $\mathscr{K}$ is the total kinetic energy, N is the number of particles in the system, m is the mass, $\mathbf{v}$ is the velocity, properties of particle i are described by a subscript.

We describe the total energy as:

$$E = \mathscr{K} + U, \tag{2.91}$$

which is the conserved quantity in the NVE ensemble.

2.5.2 Temperature

The temperature in the statistical ensemble of a molecular dynamics calculation is defined as the average kinetic energy per degree of freedom, rescaled into temperature units by the Boltzmann relation. This is defined mathematically as:

$$T = k_B \frac{\langle 2\mathscr{K} \rangle}{N_f}, \tag{2.92}$$

where T is the temperature, k_B is the Boltzmann constant, N_f is the number of degrees of freedom in the system, usually $3N$ for a perfect, unconstrained gas.

2.5.3 Pressure

The virial theorem [Allen and Tildesley, 1987] allows us to calculate the pressure of a molecular dynamics calculation.

The general form for the pressure of an ideal gas in a periodic cell can be separated into two components:

$$\underline{\underline{\mathbf{P}}} = \underline{\underline{\mathbf{P}}}_{\text{kin}} + \underline{\underline{\mathbf{P}}}_{\text{pot}}. \tag{2.93}$$

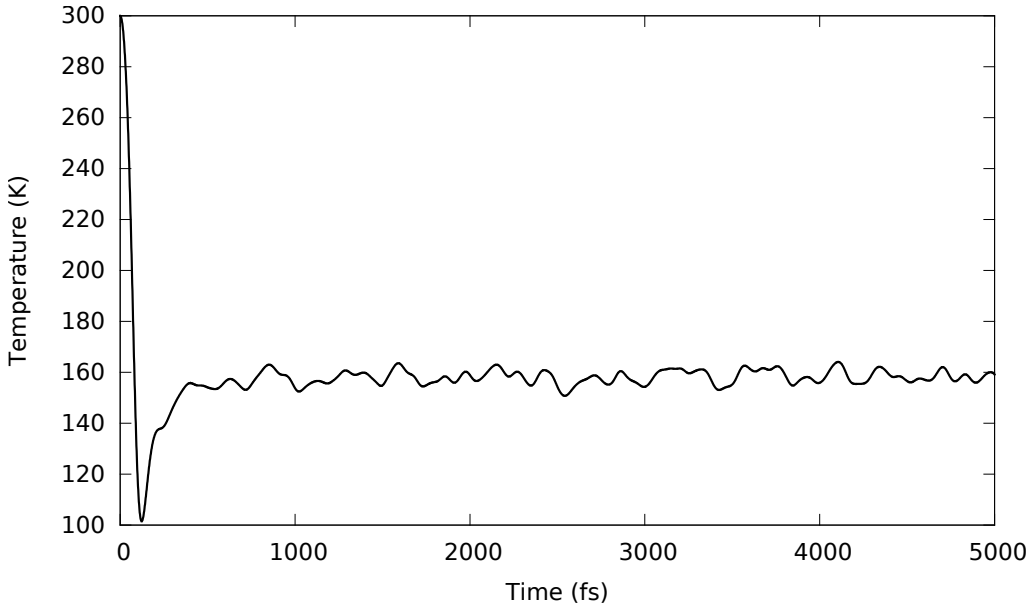

Figure 2.5: Temperature-time plot for a 864-atom Lennard-Jones NVE system initialised at $300K$, starting from a perfect 0K FCC crystal structure, and run through MD for 5000 time-steps. Note that the drop to $160K$ is due to the principle of equipartition of energy.

That is, the potential and kinetic components of the pressure, otherwise known as the static and dynamic pressures in the cell.

The kinetic component of the pressure is easily shown to be:

$$P_{\text{kin}}^{\alpha\beta} = \frac{1}{V}\sum_{i=1}^{N} m_i v_i^{\alpha} v_i^{\beta}, \tag{2.94}$$

where m is the mass, v is the velocity component in a particular direction, α and β are given directions, properties of particle i are described by a subscript.

Using the equations described in earlier sections, the virial equation describes how a pairwise, additive potential generating a force, gives us a measure of the static pressure in a periodic cell:

$$P_{\text{pot}}^{\alpha\beta} = \frac{1}{V}\sum_{i<j} F_{ij}^{\alpha}\mathbf{r}_{ij}^{\beta}, \tag{2.95}$$

where F_{ij} is the component, in a particular direction, of the force between particles i and j, likewise r is the component of the inter-particle separation, α and β are given directions.

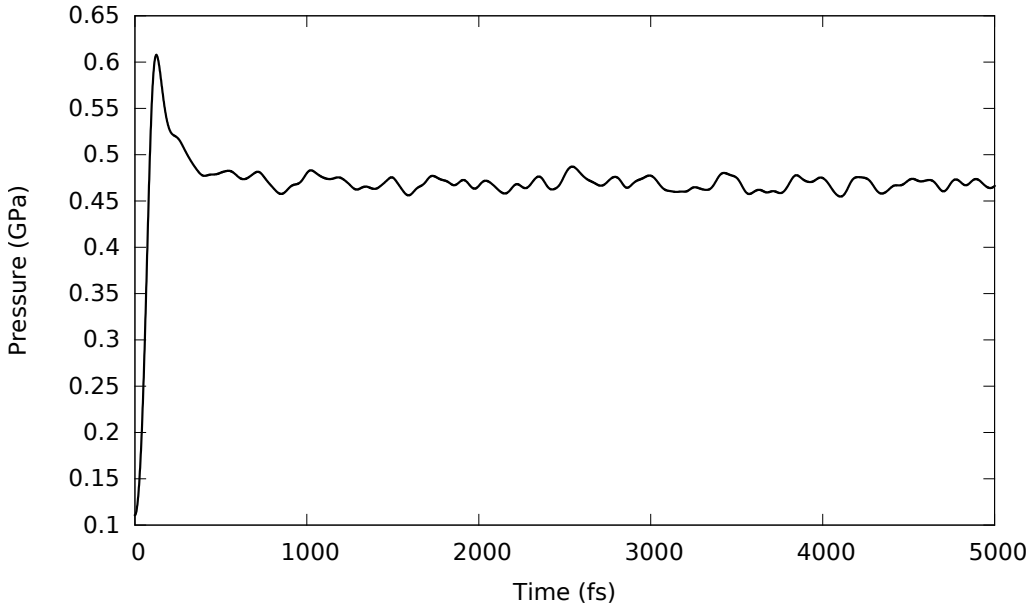

Figure 2.6: Pressure-time plot for a 864-atom Lennard-Jones NVE system initialised at $300K$, starting from a perfect 0K FCC crystal structure, and run through MD for 5000 time-steps.

2.5.4 Heat Capacity

Heat capacity at constant volume or constant pressure can be found through using different ensembles. The two forms of specific heat are usually defined as follows:

$$C_V = \left.\frac{\partial E}{\partial T}\right|_{N,V}, \tag{2.96}$$

$$C_P = \left.\frac{\partial E}{\partial T}\right|_{N,P}, \tag{2.97}$$

which both correspond more or less directly to a series of measurements at controlled temperatures and a first order derivative.

The heat capacities can be calculated from a fluctuation formula [Landau and Lifshitz, 1980], by measuring the mean squared deviations of the energy we find:

$$\text{Using NVE :} \qquad \left\langle (\Delta E)^2 \right\rangle = \frac{1}{N}\sum_{i=1}^{N}(E_i - \langle E \rangle)^2 = k_B T^2 \left.\frac{\partial E}{\partial T}\right|_V = k_B T^2 C_V, \tag{2.98}$$

$$\text{Using NVT :} \qquad \left\langle (\Delta H)^2 \right\rangle = k_B T^2 \left.\frac{\partial E}{\partial T}\right|_P = k_B T^2 C_P, \tag{2.99}$$

where H is the enthalpy $E + PV$.

This fluctuation approach is built into the CASTEP analysis utility MDTEP.

2.5.5 Bulk Modulus

The bulk modulus describes the resistance of a medium to a volume change due to external pressure, defined as:

$$B = -V\frac{\partial P}{\partial V} = -V\frac{\partial^2 E}{\partial V^2} \tag{2.100}$$

The bulk modulus of a material can be extracted from a energy-volume plot as the derivative of the curve or by fitting one of a number of equations of state for compressible materials [Hebbache and Zemzemi, 2004]:

$$E_{BM}(\eta) = E_0 + \frac{9B_0V_0}{16}\left(\eta^2-1\right)^2\left(6+B_0'\left(\eta^2-1\right)-4\eta^2\right), \tag{2.101}$$

$$E_{Vin}(\eta) = E_0 + \frac{2B_0V_0}{\left(B_0'-1\right)^2}\left(2-\left(5+3B_0'(\eta-1)-3\eta\right)\exp\left(-\frac{3\left(B_0'-1\right)(\eta-1)}{2}\right)\right), \tag{2.102}$$

$$E_{PT}(\rho) = E_0 + \frac{B_0V_0\rho^2}{6}\left(3+\rho\left(B_0'-2\right)\right), \tag{2.103}$$

where E_{BM} is the Birch-Murnaghan EoS [Birch, 1947], E_{Vin} is the Vinet EoS [Vinet *et al.*, 1987] and E_{PT} is the Poirier-Tarantola EoS [Poirier and Tarantola, 1998], subscript 0 refers to a value at equilibrium volume (i.e. $P = 0$), η is the linear change in volume $\left(\frac{V}{V_0}\right)^{\frac{1}{3}}$, B' is the first derivative of the bulk modulus $\frac{\partial B}{\partial V}$, $\rho = -3\ln(\eta)$.

This is usually done by a series of static compressions and relaxations of the structure of interest and extraction of the final energies of the system (Fig. 2.7). The inverse of the bulk modulus is called the compressibility and is commonly represented as β.

The bulk modulus can also be calculated from a fluctuation formula [Landau and Lifshitz, 1980], by measuring the mean squared deviations of the volume we find:

$$\left\langle\left(\Delta V\right)^2\right\rangle = -k_BT\left.\frac{\partial V}{\partial P}\right|_T = Vk_BT\beta_T = \frac{Vk_BT}{B_T}, \tag{2.104}$$

where B_T describes the isothermal bulk modulus, rather than the equilibrium bulk modulus (B_0).

This fluctuation approach is built into MDTEP.

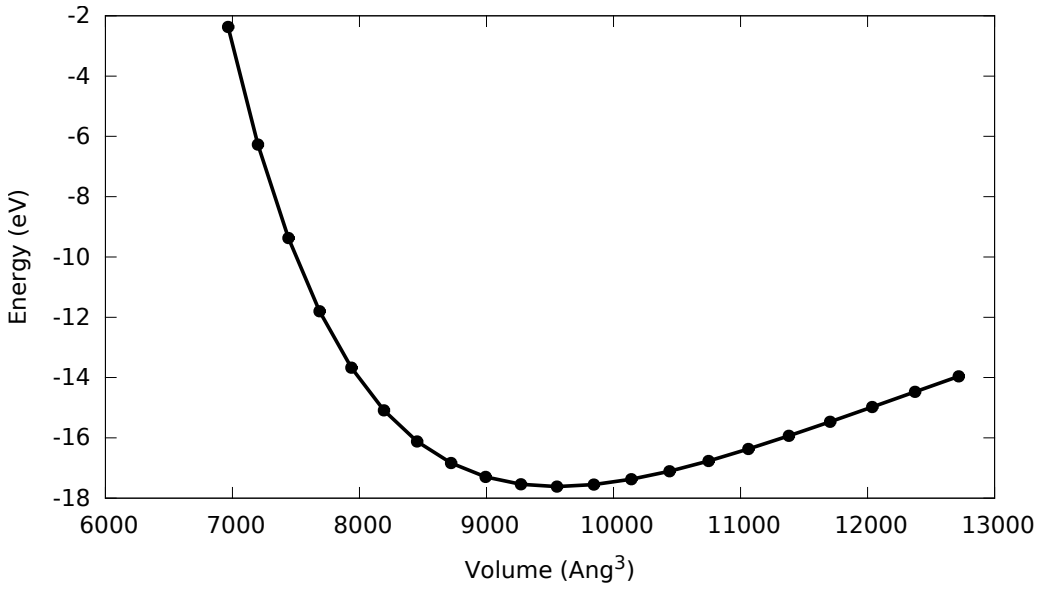

Figure 2.7: Energy-volume plot for a 256-atom FCC Lennard-Jones system. The derivative about the approximately quadratic minimum gives the equilibrium bulk modulus (B_0).

2.5.6 Thermal Coefficient of Expansion

The thermal coefficient of expansion of a material can be calculated from the fluctuation of the material in a pressure regulated ensemble (e.g. NPT) or from long time constrained volume calculations (e.g. NVT) [Buda *et al.*, 1990] by means of:

$$\alpha = \frac{1}{3V}\left.\frac{\partial V}{\partial T}\right|_P \qquad \text{for NPT,} \tag{2.105}$$

$$\alpha = \frac{1}{3B}\left.\frac{\partial P}{\partial T}\right|_V \qquad \text{for NVT,} \tag{2.106}$$

where α is the thermal coefficient of expansion, V is the volume, T is the temperature and B is the bulk modulus.

The thermal coefficient of expansion can also be calculated from a fluctuation formula [Landau and Lifshitz, 1980], by measuring the correlations of the enthalpy and volume, we find:

$$\langle(\Delta H \Delta V)\rangle = -k_B T^2 V^2 \left.\frac{\partial V}{\partial T}\right|_P = -k_B T^2 V^2 \alpha. \tag{2.107}$$

This fluctuation approach is built into the CASTEP utility MDTEP.

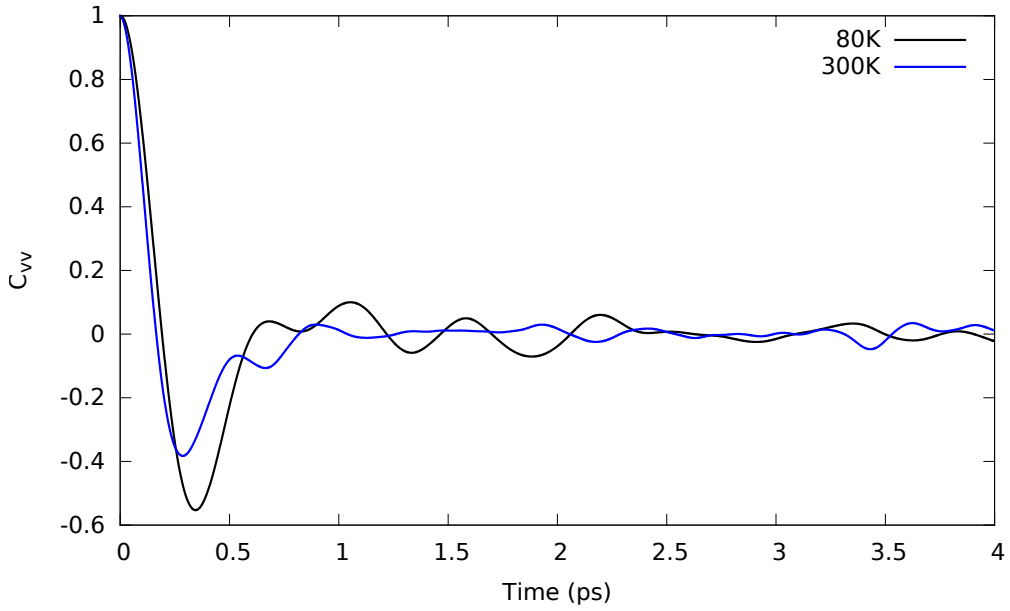

Figure 2.8: Velocity auto-correlation function for a 864-atom Lennard-Jones NVE system initialised at 2 different temperatures (Black: $80K$, Green: $300K$), starting from a perfect 0K FCC crystal structure, and run through MD for 5000 time-steps at different temperatures. Note the more regular oscillations of the lower temperature solid (Black), rather than the rapid decay of the higher temperature fluid state (Blue).

2.5.7 Velocity Auto-correlation Function

The velocity auto-correlation function (VAC) measures the correlation of the velocity with itself at another time w.r.t. the time difference between them. It can be defined as:

$$C_{vv}(t) = \frac{\langle \mathbf{v}_i(t+t_0) \cdot \mathbf{v}_i(t_0) \rangle}{\langle \mathbf{v}_i(t_0) \cdot \mathbf{v}_i(t_0) \rangle}, \tag{2.108}$$

$$= \frac{\sum_{t_0} \sum_{i=1}^{N} \mathbf{v}_i(t+t_0) \cdot \mathbf{v}_i(t_0)}{\sum_{t_0} \sum_{i=1}^{N} \mathbf{v}_i(t_0) \cdot \mathbf{v}_i(t_0)}, \tag{2.109}$$

where t is time, v is velocity, N is the total number of particles, properties of particle i are described by a subscript.

It can also be calculated as a convolution [Tuckerman, 2010]:

$$C_{vv}(t) = \frac{1}{m} v(t) * v^*(t) = \frac{1}{m} \mathscr{F}^{-1}(\mathscr{F}[v(t)]\,\mathscr{F}[v(t)]), \tag{2.110}$$

where $\mathscr{F}$ represents a Fourier transform and m is the number of time samples.

Another property of the VAC is that it can be used to calculate the Einstein

frequency of a material provided we can calculate an average curvature of the potential [Allen and Tildesley, 1987]:

$$\left\langle F_{i\alpha}^2 \right\rangle = -\left\langle F_{i\alpha} \frac{\partial U}{\partial r_{i\alpha}} \right\rangle = -k_B T \left\langle \frac{\partial F_{i\alpha}}{\partial r_{i\alpha}} \right\rangle = k_B T \left\langle \frac{\partial^2 U}{\partial r_{i\alpha}^2} \right\rangle, \tag{2.111}$$

where α denotes an arbitrary direction and other symbols have their usual meanings.

Via a simple substitution from here, it is possible to show that the Einstein frequency is given by:

$$\omega_E^2 = \frac{1}{3m_i} \left\langle \nabla_{r_i}^2 U \right\rangle \tag{2.112}$$

The calculation of the VAC is included in the software package CASTEP as part of MDTEP.

2.5.8 Phonon Properties

Phonons can be calculated from calculations by a number of approaches.

There are several methods built into CASTEP involving direct calculation of phonon frequencies by either response measurement of finite displacements, or by density functional perturbation theory [Refson], which is a perturbation theory expansion of the wavefunction's response to deviations in the atomic positions. These attempt to give the full phonon spectrum with correct amplitudes and so are expensive to calculate, especially for larger systems.

Another approach we can use, which is somewhat cheaper is to Fourier transform the VAC (§2.5.7), which approximates the phonon density of states (Fig. 2.9). It does not, however, capture the vibrational absorption intensities [Allen and Tildesley, 1987].

2.5.9 Grüneisen parameter

The Grüneisen parameter [Grüneisen, 1912] is a dimensionless value, which describes the effect of changing the volume of the lattice on the lattice phonons, as such it also describes the relationship between temperature and the lattice dynamics. The Grüneisen parameter plays a key rôle in the calculation of the Mie-Grüneisen EoS, but is also dependent on the volume and temperature, leading to accuracy problems in fitting these EoSs [Guillermet, 1987].

There are two major Grüneisen parameters, which are the mean Grüneisen parameter, which is commonly obtained through thermodynamic processes

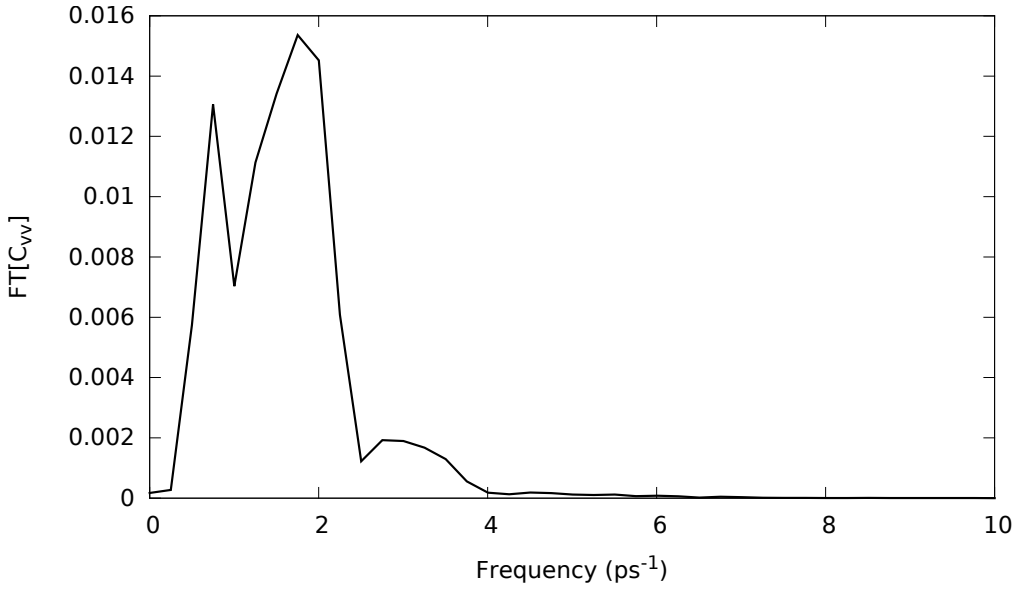

Figure 2.9: Fourier transform of velocity auto-correlation function for a 864-atom Lennard-Jones NVE system initialised at $80K$, starting from a perfect 0K FCC crystal structure.

and the modal Grüneisen parameter which is determined through phononic calculations. The mean Grüneisen parameter is defined equivalently as:

$$\gamma = V\left(\frac{\partial P}{\partial E}\right)_V = \frac{\alpha B_T}{C_V \rho} = \frac{\alpha v_s^2}{C_P}, \tag{2.113}$$

where E is the internal energy, C_V is the specific heat capacity at constant volume, likewise C_P is the constant pressure specific heat capacity, α is the coefficient of thermal expansion, B_T is the bulk modulus at constant temperature, v_s is the speed of sound, and ρ is the density of the material.

The modal Grüneisen parameter is defined as:

$$\gamma_i = -\frac{V}{\omega_i}\frac{\partial \omega_i}{\partial V}, \tag{2.114}$$

where γ_i is the Grüneisen parameter of a given oscillatory mode described by ω_i. The mean and modal Grüneisen parameter are related by a weighted sum:

$$\gamma = \frac{\sum_i \gamma_i C_{V,i}}{\sum_i C_{V,i}}, \tag{2.115}$$

where $C_{V,i}$ is the specific heat capacity of that mode, constructed such that:

$$C_V = \frac{1}{\rho V}\sum_i C_{V,i}. \tag{2.116}$$

The Grüneisen parameter can be extracted through a series of NVT calculations at different temperatures and calculating the finite difference derivative between these runs [Ono, 2009].

It is possible to derive a fluctuation formula for the Grüneisen parameter from Haile [1992]:

$$\gamma = \frac{V}{C_V}\gamma_v, \tag{2.117}$$

where C_V is the heat capacity (§2.5.4) and:

$$\gamma_v = \left.\frac{\partial P}{\partial T}\right|_V = \frac{C_V}{T^2}\langle(\Delta P \Delta T)\rangle\,, \tag{2.118}$$

where γ_v is the thermal pressure coefficient [Landau and Lifshitz, 1980]. Thereby we find that:

$$\gamma = \frac{V}{C_V}\frac{C_V}{T^2}\langle(\Delta P \Delta T)\rangle = \frac{V}{T^2}\langle(\Delta P \Delta T)\rangle\,. \tag{2.119}$$

2.6 Structural Analysis

The way in which atoms in a material align is a subject of great interest in materials science, as different polymorphs of materials often exhibit very different properties. New phases of materials can be very valuable in understanding how suitable a material is for an application. If a material is used for a particular property, a phase change may render it unsuitable for certain applications. Materials in extreme conditions such as shocks are often significantly different from those in ambient conditions, so it is essential that we can detect and categorise these changes.

2.6.1 Voronoi Tessellation

Voronoi analysis is a technique which divides a space into regions where the regions are defined by their distance from a set of points. Each region is the area in which all points within the region are closest to the point inside that region than any other points in the set. The distance metric can be any function which obeys the laws of a metric, but for the purposes of structural analysis of real, Cartesian crystals, we use the Euclidean norm [Allen and Tildesley, 1987].

From this 3-D region, we can use properties of the faces and edges of the polyhedron to define various new properties and the construction of edges perpendicular to the centre of the faces will always be the edge between two particles, allowing us to define a closest neighbour. The graph constructed from these

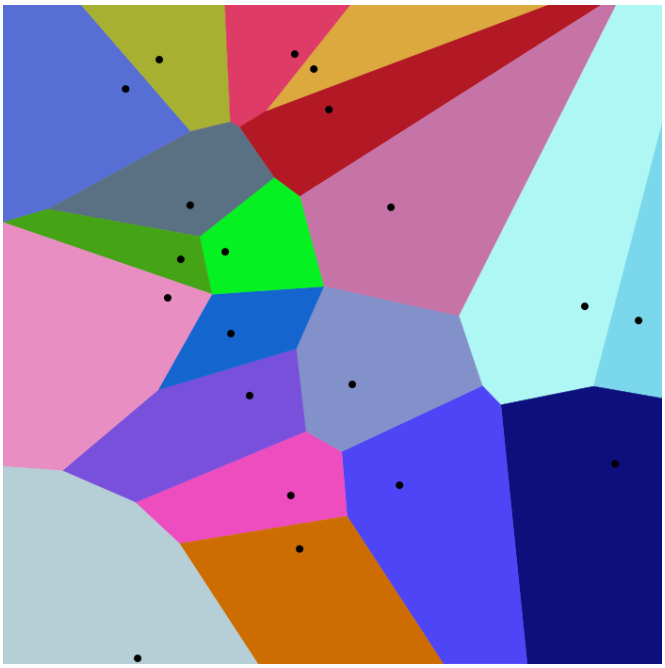

Figure 2.10: An example 2D Voronoi diagram of semi-random points using the Euclidean norm as the distance metric. Taken from Wikipedia [a].

edges is referred to as the Delaunay triangulation.

A common measure used is the volume of the Voronoi polyhedron which not only gives us an indication of the approximate free space atoms have and a measure of the local structure, but also in combination with (§2.5.3) allows us to calculate a per-atom pressure using the Voronoi polyhedron.

2.6.2 Bravais Lattices, Space and Point Groups

Bravais lattices are the set of all possible 3-dimensional shapes a periodic crystal can exhibit. Given the matrix of cell vectors:

$$\underline{\underline{\mathbf{h}}} = (\mathbf{a}_1 \vdots \mathbf{a}_2 \vdots \mathbf{a}_3), \tag{2.120}$$

the Bravais lattice is the complete set formed by integer multiples of the cell-vectors:

$$\underline{\underline{\mathbf{R}}} = n_1\mathbf{a}_1 + n_2\mathbf{a}_2 + n_3\mathbf{a}_3. \tag{2.121}$$

There are further Bravais lattices defined by additional atoms centred on points which are not the corners of the unit cell. These lead to 4 sets of basic types

Primitive (P) – Only at the unit cell corners

Base-centred (C) – Extras at centres of 2 (by symmetry/periodicity) opposing faces of the unit cell

Body-centred (I) – Extra at centre of the unit cell

Face-centred (F) – Extra at the centre of each face of the unit-cell

It turns out there are only 14 possible Bravais lattices in three dimensions formed from these 3 vectors (Table 2.1)[Ashcroft and Mermin, 1976]. Using the following definitions:

$$a = \|\mathbf{a}_1\|, \;\; b = \|\mathbf{a}_2\|, \;\; c = \|\mathbf{a}_3\| \tag{2.122}$$

$$\cos(\alpha) = \frac{\mathbf{a}_1 \cdot \mathbf{a}_2}{ab}, \;\; \cos(\beta) = \frac{\mathbf{a}_1 \cdot \mathbf{a}_3}{ac}, \;\; \cos(\gamma) = \frac{\mathbf{a}_2 \cdot \mathbf{a}_3}{bc} \tag{2.123}$$

Name	Lengths	Angles	Atom-centres
Cubic	$a = b = c$	$\alpha = \beta = \gamma = 90^\circ$	P, I, F
Tetragonal	$a = b \neq c$	$\alpha = \beta = \gamma = 90^\circ$	P, I
Orthorhombic	$a \neq b \neq c$	$\alpha = \beta = \gamma = 90^\circ$	P, C, I, F
Rhombohedral	$a = b = c$	$\alpha = \beta = \gamma \neq 90^\circ$	P
Hexagonal	$a = b \stackrel{?}{=} c$	$\alpha = \beta = 90^\circ, \gamma = 120^\circ$	P
Monoclinic	$a \neq c$	$\alpha = \gamma = 90^\circ, \beta \neq 90^\circ$	P, C
Triclinic	$a \neq b \neq c$	$\alpha \neq \beta \neq \gamma$	P

Table 2.1: List of relationships between the 7 different Bravais lattices permissible in three dimensions

Space and point groups are classifications of symmetries in periodic structures [Ashcroft and Mermin, 1976].

Point groups are combinations of 5 possible symmetry classes:

1. Rotations about an axis
2. Reflections across a plane
3. Inversions about a point
4. Rotation followed by reflection
5. Rotation followed by inversion

Combinations of these symmetry operations and the Bravais lattices give rise to the 230 space groups

2.6.3 Global Structure Analysis

Global structure analysis looks at the structure of the entire cell in a periodic context and tries to assign an order parameter to the entire system. This is useful for categorising crystals into various classes as described in (§2.6.2). These

methods can be engineered to defined crystal structures and can be made tolerant to thermal noise if required, unfortunately these methods are often not usable in large systems, where long range order may not be present, while short range order is.

2.6.3.1 Space Group Analysis

Space group analysis involves looking at the symmetries of the crystal and determining from the repeating pattern in periodic boundary conditions to which space group the structure belongs. Certain space groups correspond to certain crystal classes and allow easy identification of the materials.

2.6.3.2 Radial Distribution Function

The radial distribution function (RDF) is the distribution of inter-atomic distances over the course of a molecular dynamics run, i.e. a weighted likelihood at any given time of finding a particle at distance r from any given central atom. It is calculated by constructing a histogram of all recorded inter-atomic separations, and normalising the result with respect to a spherical domain. In three dimensions, this can be expressed as:

$$g(r) = \frac{n(r)}{\rho 4\pi r^2 \Delta r}, \tag{2.124}$$

where $n(r)$ is the frequency of the given distance, ρ is the density, r is the separation, Δr is the histogram bin width.

The RDF can be used for calculating a number of more detailed crystal properties such as the structure factor, or in the calculation of the isothermal compressibility of a material, but is also useful in its own right as a measure of crystallinity within a system.

The calculation of the RDF is included in the software package CASTEP as part of MDTEP [Quigley] and in the cell visualisation and analysis software OVITO [Stukowski, 2010].

2.6.3.3 Fourier Methods

It is possible to use transforms of the atomic coordinates of atoms to gain a full Fourier representation of the atomic space of the system rather than the spacially reduced sampling of the structure factor or RDF methods. The Fourier transform of atomic coordinates equates experimentally to the effect of powder

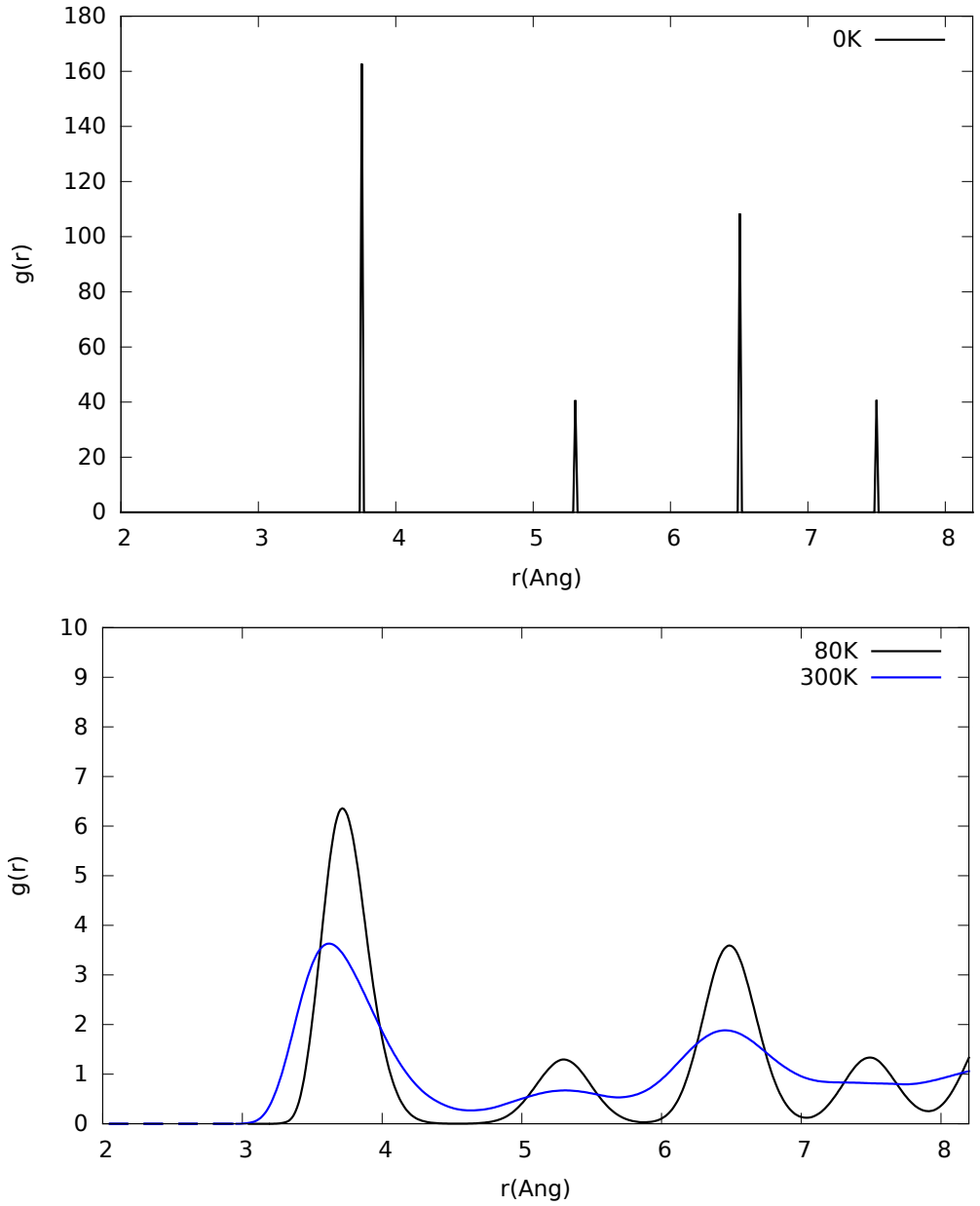

Figure 2.11: Radial distribution function for a 864-atom Lennard-Jones NVE system, starting from a perfect 0K FCC crystal structure, and run through MD for 5000 time-steps at different initial temperatures. The melting point is $\sim 120K$. Note the delta functions of the perfect crystal whose width is purely the bin-width, and the thermal smearing as the particles are allowed to move from their lattice sites. Though they still oscillate about their lattice sites, hence the average location is at the peak of the delta functions.

X-ray diffraction experiments and is commonly used to compare with these experimental methods.This can be built up over time series data to get directly comparable information to experimental systems [Kimminau *et al*., 2007].

2.6.4 Local Structurments e Analysis

In order to work out what effect our shock has had on the post-shock structure and in an attempt to categorise potential phase transitions in a disordered structure, which may contain many phases, it becomes necessary to have a way in which we can use a computer to recognise different structural configurations. Because, as previously mentioned, it is possible that our cell contains a variety of different structures, breaking the symmetry of the system, it becomes impossible to use global structural analysis techniques and calculate space-groups of our periodic crystal, and we must define a method for local structure analysis. Because there is no universal definition of structure on a local scale, there are many approaches to local structure analysis. This section contains a selection of these which may be relevant to our cause.

2.6.4.1 Voronoi Cell Topology

Voronoi Cell Topological Analysis is a class of methods which use measurements of the constructed Voronoi cells (§2.6.1) directly [Bernal, 1959]. The number of edges of a Voronoi face indicates the number of shared neighbours between the two faces and constructing histogram of the neighbour frequency gives a good indication of the local structure. Unfortunately, this approach is very susceptible to noise, as slight perturbations to the system can push a nearest neighbour exactly on the border between two or more atoms out of this domain. As this measure is a single integer value per atom, perturbations can cause quite dramatic broadening of the peaks for very minor disruption.

This approach, known as Nearest Neighbour Counting, was pioneered in liquids and subsequently applied to a variety of condensed matter systems. This method can be used in combination with the RDF (§2.6.3.2) to perform a more detailed analysis and provide more accurate estimates of the crystal structure. However, it became clear that to distinguish similar environments simply, an extension was required.

Lazar *et al*. [2015] provided a possible extension by examining how critical points (i.e. those sensitive to small perturbations) on the Voronoi surface change with respect to infinitesimal perturbations on the structure. Using an approach described in Lazar *et al*. [2012], they characterise these possible structures and

identify 3 major types, which correspond to particular Voronoi structures, and frequencies of these Voronoi structures identify the local structure.

This approach has been implemented in the cell visualisation and analysis software OVITO [Stukowski, 2010].

2.6.4.2 Common Neighbour Analysis

Common Neighbour Analysis (CNA) [Honeycutt and Andersen, 1987] is a method where atoms within a specified cut-off radius are considered neighbours. Generally these radii are considered to be:

$$r_{cut}^{fcc} = \frac{1}{2}\left(\sqrt{\frac{1}{2}}+1\right) a_{fcc} \approx 0.854 a_{fcc}, \tag{2.125}$$

$$r_{cut}^{bcc} = \frac{1}{2}\left(\sqrt{2}+1\right) a_{bcc} \approx 1.207 a_{bcc}, \tag{2.126}$$

where a refers to the lattice constant associated with the corresponding crystal structure. From this list of neighbours, three key measurements are taken:

1. The number of neighbours common to both
2. The number of bonds between the common neighbours
3. The longest chain of bonds between these common neighbours

An extension to CNA, called adaptive common neighbour analysis was presented in Stukowski [2012] to allow for local structure analysis multi-phase systems.

This approach has been implemented in the visualisation and analysis software OVITO [Stukowski, 2010].

2.6.4.3 Centrosymmetry Analysis

Centrosymmetry Analysis (CSA) [Kelchner *et al.*, 1998] is a method which uses a weighted symmetry about the central atom to detect defects when a local-bond symmetry breaks. For a system of N neighbours, the centrosymmetry parameter (CSP) is defined as:

$$CSP = \sum_{i=1}^{N/2} \left\| \mathbf{r}_i + \mathbf{r}_{i+\frac{N}{2}} \right\|^2, \tag{2.127}$$

where the vectors $\mathbf{r}_i$ are the vectors from the central ion to ion i in the list of N neighbours. Given that the particles are indexed cyclically about the central

ion, opposite pairs should be separated by $\frac{N}{2}$ and so are at opposite sides of the central ion,

$$\mathbf{r}_i + \mathbf{r}_{i+\frac{N}{2}} = 0 \tag{2.128}$$

if the neighbours are symmetric about the centre. This makes the calculation robust to any affine transformations of the crystal lattice, though it is still susceptible to thermal variations. It is also difficult to distinguish between different symmetric states, and mostly serves to detect areas where distortions and dislocations are present rather than their structure.

This method is implemented in the visualisation and analysis software OVITO [Stukowski, 2010].

2.6.4.4 Angle Distribution Analysis

Angle distribution analysis (ADA) [Ackland and Jones, 2006] is a method which uses a histogram binning of neighbours within a radius to assign a numerical value to the likeness of a structure to an archetypal structure, using the values contained in Table 2.2. The advantage of this method is that it is possible to construct additional δ-terms to characterise different structures and that it is robust to ordinary thermal fluctuations.

	Minimum $\cos\theta_{ijk}$	Maximum $\cos\theta_{ijk}$	bcc	Ideal fcc	hcp
χ_0	-1.0	-0.945	7	6	3
χ_1	-0.945	-0.915	0	0	0
χ_2	-0.915	-0.755	0	0	6
χ_3	-0.755	-0.705	36	24	21
χ_4	-0.195	0.195	12	12	12
χ_5	0.195	0.245	0	0	0
χ_6	0.245	0.795	36	24	24
χ_7	0.795	1.0	0	0	0
δ_{bcc}	$0.35\frac{\chi_4}{\chi_5+\chi_6+\chi_7-\chi_4}$				
δ_{CP}	$0.61\left\|1-\frac{\chi_6}{24}\right\|$				
δ_{fcc}	$0.10\dot{1}\dot{6}(\|\chi_0+\chi_1-6\|+\chi_2)$				
δ_{hcp}	$0.8\dot{3}(\|\chi_0-3\|+\|\chi_0+\chi_1+\chi_2+\chi_3-9\|)$				

Table 2.2: Taken from [Ackland and Jones, 2006] gives the calculated values of the ADA scheme which were found to define given structures, where: bcc = body-centred cubic; CP = general close-packed; fcc = face-centred cubic and hcp = hexagonal close-packed. θ_{ijk} refers to the angle between any 3 atoms i,j and k

This method is implemented in the visualisation and analysis software OVITO [Stukowski, 2010].

2.6.4.5 Adaptive Template Analysis

Adaptive template analysis (ATA) [Sapozhnikov *et al.*, 2008] is a set of algorithms for matching key local crystal orientations. It involves defining the key parameters based on a number of measurements in three steps:

1. Correspondence between crystal atoms and template points,
2. Generation of a template of suitable size,
3. Calculation of the root-mean-square deviation (RMSD) and deviation from the applied template

These templates are called adaptive because the corresponding template, against which calculations are compared, is fit to the structure on-the-fly. The algorithms for constructing said templates, however, are strictly defined for each crystal structure and identification of a new crystal type requires a new template to be generated. This renders the technique somewhat inflexible as the algorithms for different structures, though they share some key similarities they are sufficiently different to each other to cause difficulty.

2.7 Application to this work

The purpose of this work is to analyse and measure key features of shocked materials in molecular dynamics simulations. Analysis of the various properties of materials in the shocked state will help to confirm the robustness and applicability of the new methods developed in this work and the work of others, along with providing means for new insights into known materials and material design.

Chapter 3

Potentials and Forces

As has been shown, all results of a molecular dynamics simulation ultimately derive from the energies of the system, and properties of the system can all be defined in terms of the energies of the system. As such it is essential in molecular dynamics to have an accurate and efficient means of determining energies of the system.

Also, as we have seen in §2.4.1, the derivatives of these energies, the forces, are the governors of the dynamics of the system and what make a system representative of a real material.

3.1 Empirical Forcefields

Empirical forcefields are the simplest and cheapest method of calculating the energies and forces within a molecular dynamics simulation. They are a simplification of complicated electronic interactions down to a single functional form. These functional forms are usually fitted to a series of calculations using more exact methods, such as *ab initio* calculations, or to reproduce experimental properties of a particular material.

The difficulty in using empirical forcefields is that because they are of fixed functional form and fitted to particular set of data, they can be incorrect or have peculiarities if extrapolation beyond these fitted regions is attempted. Despite this, they see common usage in many applications including shockwaves, which lie well beyond the regions to which they were originally fitted [Farrow and Probert, 2011].

The force due to empirical potentials is usually calculated by an exact derivative of the functional form of the potential with respect to displacement. Even for complicated functional forms, this is usually straightforward and fast to

calculate computationally.

In order to reduce computational costs of empirical forcefields, due to the fact that most potentials decay rapidly at long range, they are usually truncated to zero after a certain distance. The major exception to this is potentials of the order $\frac{1}{r}$ which includes the Coulombic potential This truncation is called a "cut-off" and is used for most empirical potentials. Due to the formation of a discontinuity at the cut-off point, this truncation is usually implemented in one of three ways:

1. Ignoring the discontinuity, the cut-off simply truncates the energy to 0 outside the range:

$$V(r_{ij}) = \begin{cases} V(r_{ij}), & 0 < r_{ij} \leq r_{cut} \\ 0, & r_{ij} > r_{cut} \end{cases} \tag{3.1}$$

2. The potential is shifted such that the energy decays naturally to 0 at the point of the cut off, removing the discontinuity in the energy:

$$V(r_{ij}) = \begin{cases} V(r_{ij}) + V(r_{cut}), & 0 < r_{ij} \leq r_{cut} \\ 0, & r_{ij} > r_{cut} \end{cases} \tag{3.2}$$

3. The potential is shifted such that the force and energy both decay naturally to 0 at the point of the cut off, removing the discontinuity entirely:

$$V(r_{ij}) = \begin{cases} V(r_{ij}) - V(r_{cut}) + (r_{ij} - r_{cut}) \left.\dfrac{\partial V}{\partial r}\right|_{r_{cut}}, & 0 < r_{ij} \leq r_{cut} \\ 0, & r_{ij} > r_{cut} \end{cases} \tag{3.3}$$

3.1.1 Lennard-Jones Potential

The Lennard-Jones (LJ) potential [Lennard-Jones, 1924] is one of the most common testing potentials used in molecular dynamics as it is very cheap and fast to calculate. The potential is designed to represent the van der Waals' interactions occurring in noble gases.

The LJ potential is of the form:

$$V_{LJ}(r_{ij}) = 4\varepsilon\left(\left(\frac{\sigma}{r_{ij}}\right)^6 - \left(\frac{\sigma}{r_{ij}}\right)^{12}\right) \tag{3.4}$$

where r_{ij} is the separation of atoms i and j, ε is the minimum of the potential, and σ is the position of the minimum of the potential.

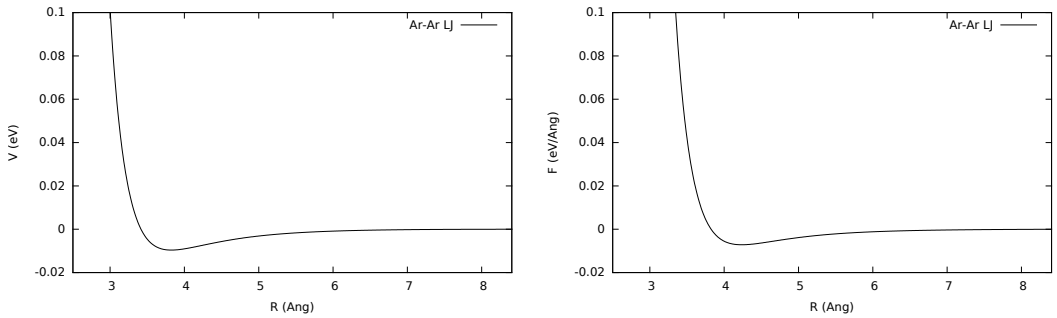

Figure 3.1: Potential (left) and force (right) curves for Lennard-Jones Argon potential.

The origin of the potential is from the ${r_{ij}}^{-6}$ fluctuating dipole-dipole term, and the numerically convenient ${r_{ij}}^{-12}$ close-range repulsive force.

It is often parametrised to argon.

ε (Kk_B)	σ (Å)
120.0	3.405

Table 3.1: Lennard-Jones argon parametrisation

3.1.2 BKS Potential

The BKS potential developed by van Beest, Kramer and van Santen [van Beest *et al.*, 1990] in order to model aluminosilicophosphates in clusters. It is derived from a series of *ab initio* Hartree-Fock calculations. They adopted the form of a Buckingham exponential [Buckingham, 1938] with an additional Coulomb term. Corrections were suggested to eliminate issues with atom overlap at high pressure by Farrow and Probert [2011], the potential becomes:

$$V_{BKS}(r_{ij}) = A_{\alpha\beta}\exp(-b_{\alpha\beta}r_{ij}) - \frac{C_{\alpha\beta}}{{r_{ij}}^6} \tag{3.5}$$

$$V_{sr}(r_{ij}) = \frac{D_{\alpha\beta}}{{r_{ij}}^2} + \frac{E_{\alpha\beta}}{{r_{ij}}^6} + F_{\alpha\beta} \tag{3.6}$$

$$V_{Coulomb}(r_{ij}) = \frac{q_\alpha q_\beta}{r_{ij}}, \tag{3.7}$$

where α and β are labels of the species of atoms i and j

$$V(r_{ij}) = \begin{cases} V_{sr}(r_{ij}), & r_{ij} < r_{sr} \\ V_{BKS}(r_{ij}), & r_{sr} < r_{ij} < r_{cut} \\ 0, & r_{ij} > r_{cut} \end{cases} \tag{3.8}$$

$$V_{tot} = V(r_{ij}) + V_{Coulomb}(r_{ij}) \tag{3.9}$$

The Coulomb interaction is evaluated by Ewald's method to account for the long-range convergence issues and is applied at all $\mathbf{r}_{ij}$.

The original parameters as defined in Farrow and Probert [2011] were found to cause a discontinuity in the potential, leading to erroneous results, to correct this, a new set of parameters was derived for the correction.

$\alpha\beta$	$A(eV)$	$b(\text{Å}^{-1})$	$C(eV\text{Å}^6)$	q
Si–O	18003.7572	4.87318	133.5381	q_{Si} = 2.4
O–O	1388.773	2.76	175	q_O = -1.2

Table 3.2: BKS parameters from papers of van Beest *et al*. [1990]

Source	$\alpha\beta$	r_{sr}(Å)	$D(eV\text{Å}^2)$	$E(eV\text{Å}^6)$	$F(eV)$
Farrow and Probert [2011]	Si–O	1.35	24.17	23.8086	-3.5872
	O–O	1.98	12.3435	18.9662	-6.9426
This work	Si–O	1.37	10.9219	20.5976	-6.43763
	O–O	1.99	23.4731	27.4136	-3.46779

Table 3.3: Short-range modifications to the BKS potential

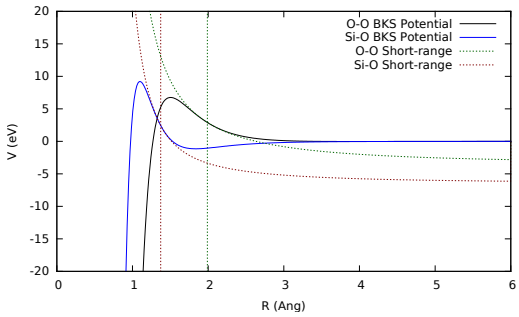

(a)

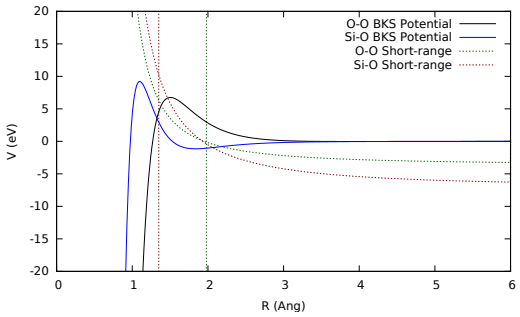

(b)

(a:This Work,b:Farrow) Separated energy curves for BKS potential and short range correction. The vertical, dotted lines represent the calculated point of inflexion in the BKS potential, and therefore the swtch to the short-ranged potential.

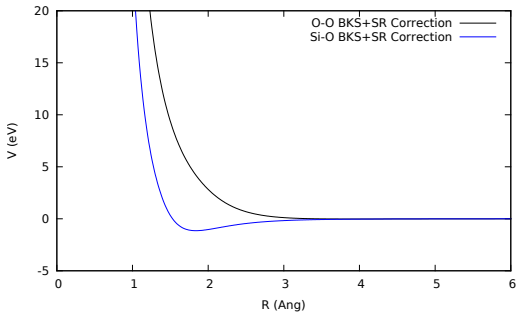

(c)

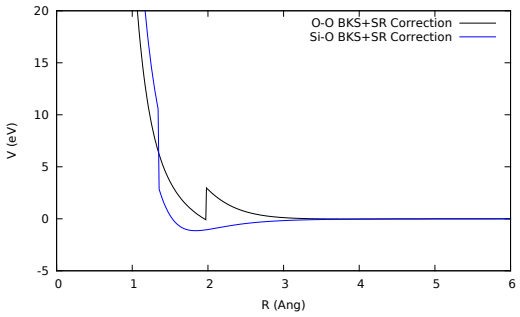

(d)

(c:This Work,d:Farrow) Potential curves for the short-range corrected BKS.

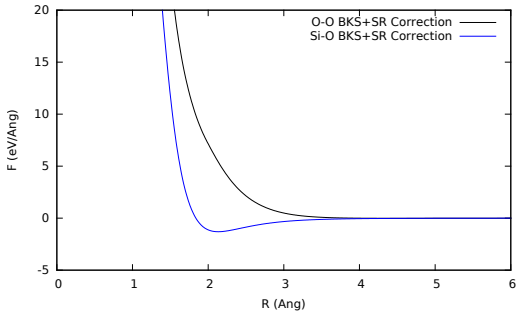

(e)

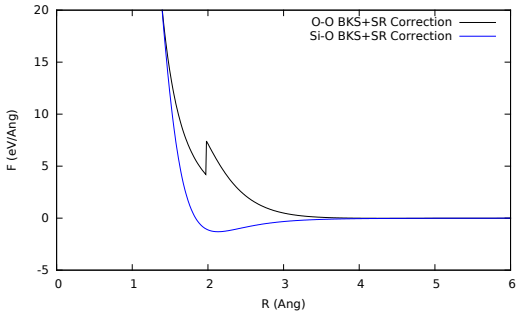

(f)

(e:This Work,f:Farrow) Force curves for the short-range corrected BKS.

Figure 3.2: Short-range corrections to the BKS Potential before (b,d,f) and after (a,c,e) re-fitting of parameters.

With this new parametrisation of the BKS potential, we find that the α-quartz phase is once again the most stable at usual volumes, which is in agreement with experiment, but was not found by Farrow [2009] (Fig. 3.3). We do find, however, that the Stishovite phase has a lower energy than the α-quartz overall, suggesting that is must be the lowest energy state of the quartz system, which is not in line with real life. This suggests that if the system ever transforms into the Stishovite phase, it would be unfavourable to transform back into the α-quartz phase.

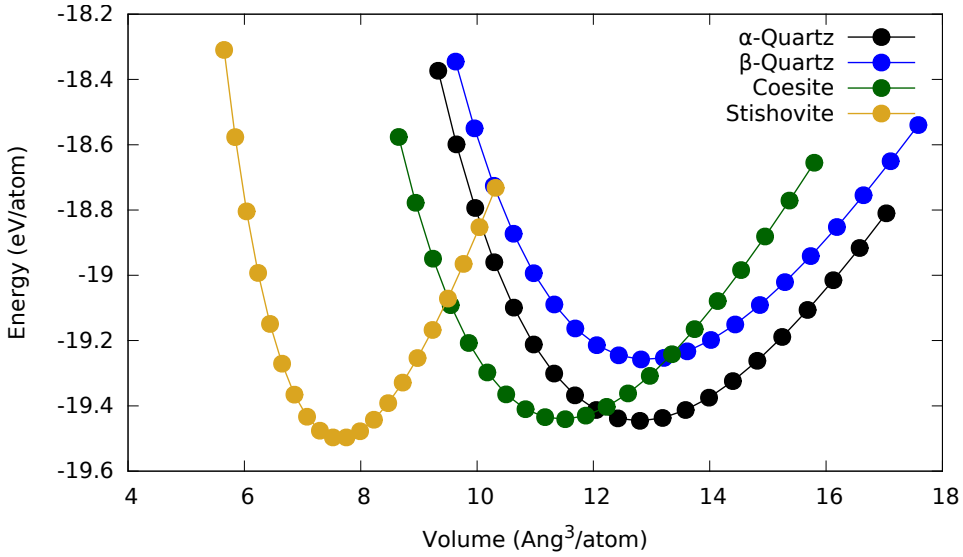

Figure 3.3: Energy-volume plot for the BKS potential showing favourable transitions of common silicate phases. At ambient temperatures and pressures, silica favours the α-Quartz phase, though through thermal excitations can excite into the β-Quartz phase (Fig. 1.6).

3.2 *Ab initio* Energies and Forces

Ab initio refers to the calculation of energies without any assumption of the system itself, just a quantum mechanical measurement, based on a solution of the full Schrödinger equation (Eq. 3.10)

$$\left[\frac{\hbar^2}{2m}\sum_{i=1}^{N}\nabla_i^2 + V(r_1,\ldots,r_N;t)\right]\Psi(r_1,\ldots,r_N;t) = E_i\Psi(r_1,\ldots,r_N;t)\,. \tag{3.10}$$

Even taking the time independent limit, where we assume that the instantaneous state of the electrons is independent of the motion of the ions (Born-Oppenheimer approximation [Engel and Dreizler, 2011]) and solve the time-independent Schrödinger equation (Eq. 3.11),

$$\left[\frac{\hbar^2}{2m}\sum_{i=1}^{N}\nabla_i^2 + V(r_1,\ldots,r_N)\right]\Psi(r_1,\ldots,r_N) = E_i\Psi(r_1,\ldots,r_N)\,, \tag{3.11}$$

a full *ab initio* solution of any real material would be prohibitively expensive (full, many-body solutions are exponentially scaling and mostly limited to fewer than 10 electrons). As such, there are many short-cuts which have been derived in order to make such approaches tractable.

A full description of the approximations and methods employed by modern *ab initio* codes is beyond the scope of this work, however, a good summary of

the approaches can be found in Payne *et al*. [1992] or Marx [2012].

This work has been developed and implemented in the plane-wave density functional theory code CASTEP [Clark *et al*., 2005], and so will focus on the periodic plane-wave DFT approach.

Due to the ability to adiabatically separate the ions and electrons (via the Born-Oppenheimer approximation [Engel and Dreizler, 2011]) we can solve the contributions of the electrons and ions independently.

$$\mathbf{F}_i^{tot} = \mathbf{F}_i^{e^-} + \mathbf{F}_i^{Z^+}. \tag{3.12}$$

The ion-ion forces in *ab initio* calculations comes from the contribution of the Coulomb term due to the charge.

$$\mathbf{F}_i^{Z^+} = \sum_{j \neq i}^{N} \frac{Z_i Z_j}{(\mathbf{R}_j - \mathbf{R}_i)^2}. \tag{3.13}$$

Unfortunately, due to the long-ranged nature of the Coulomb force and the periodic nature of our system it can be shown that the Coulomb force does not converge until infinity in either real or reciprocal space. This is remedied using a mathematical technique known as an "Ewald sum" [Ewald, 1921], which uses the properties of convergence in real and reciprocal space to perform an infinite sum in a finite time,

$$\phi_{tot}(r) = \phi_{sr}(r) + \phi_{lr}(r)\,, \tag{3.14}$$

where ϕ_{sr} is the short-range term which converges rapidly in real space and ϕ_{lr} is the long-range term which converges rapidly in reciprocal space. Details of the complete analytical form can be found in Payne *et al*. [1992].

In order to minimise the electronic ground-state of the system, without requiring the full, many-body solution to the Schrödinger equation (Eq. 3.11), the many-body equation is replaced by a sum of non-interacting single-particle states (Hohenberg and Kohn [1964] and Kohn and Sham [1965]).

$$\left[-\frac{\hbar^2}{2m}\nabla^2 + V_{ion}(\mathbf{r}) + V_H(\mathbf{r}) + V_{XC}(\mathbf{r})\right]\Psi_n(\mathbf{r}) = E_n\Psi_n(\mathbf{r})\,, \tag{3.15}$$

where V_{ion} is the ion-electron contribution to the forces and V_H is the Hartree potential which includes electron-electron contribution, both of which are well defined [Payne *et al*., 1992], and the V_{XC} is a modifying potential which accounts for the approximations made in the Kohn-Sham formulation. Its form

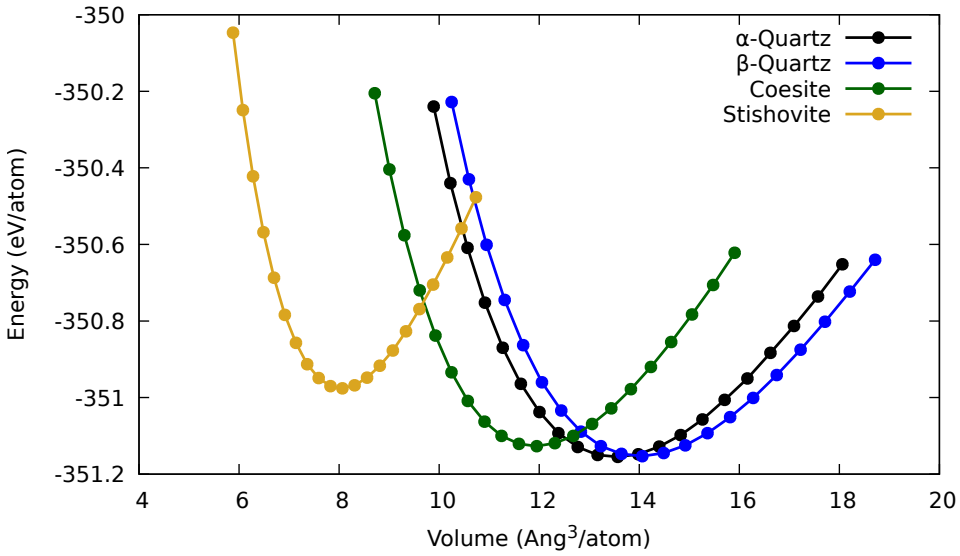

Figure 3.4: Energy-volume plot for the *ab initio* SiO_2 in different silicate phases.

is strictly unknown, though approximations are found to be sufficient for a reasonable solution in many cases [Engel and Dreizler, 2011].

These equations are then solved iteratively to self-consistency (see Payne *et al.* [1992]) to find the ground state eigenfunctions (Ψ_n) for the system.

The electronic forces in *ab initio* calculations can be found as a first order derivative with respect to position of the energy of the calculated wavefunction.

This first order derivative can be solved directly via the Hellmann-Feynman theorem [Rae, 2008] which shows that the first order derivative of the expectation value of the Hamiltonian is equivalent to expectation value of the first order derivative of the Hamiltonian, that is:

$$\frac{\partial E}{\partial \lambda} = \frac{\partial}{\partial \lambda} \langle \psi | \hat{\mathscr{H}} | \psi \rangle = \langle \psi | \frac{\partial \hat{\mathscr{H}}}{\partial \lambda} | \psi \rangle . \tag{3.16}$$

Thus, for the forces we find the derivative with respect to a change in position of the ion:

$$\mathbf{F}_i^{e^-} = -\frac{\partial E}{\partial \mathbf{R}_i} = -\langle \psi | \frac{\partial \hat{\mathscr{H}}}{\partial \mathbf{R}_i} | \psi \rangle \tag{3.17}$$

3.3 Other Approaches

There are numerous other potentials and force-field methods which could be used to produce silicate behaviour. This could be alternative parametrisations of potentials such as the Tersoff potential [Tersoff, 1988] which has been

parametrised for silicates [Munetoh *et al.*, 2007]. The reason why we have chosen the BKS potential can be explained by its greater ability to model all parts of the silica phase diagram [Cowen and El-Genk, 2015].

"Reactive potentials" such as ReaxFF [van Duin *et al.*, 2001], which are designed to handle bond making-breaking interactions have been used in both simulations of shock-waves in materials [Budzien *et al.*, 2009] and have been used in simulations of silicates [Kulkarni *et al.*, 2013].

Other methods exist which could be used to automatically generate potentials with more flexible functional forms such as [Bartók *et al.*, 2010] which uses DFT data to fit to a variety of forms and provides information about the most viable potential to match the acquired data.

As discussed previously, however, these potentials still possess the same limitations in that they are usually fit to equilibrium systems and cannot be guaranteed to reproduce the complex processes involved in non-equilibrium extreme states simulations.

It would be possible to parametrise a potential specifically for the purposes of reproducing properties relevant to the shock system, though this might fail to reproduce equilibrium properties to which the other potentials are fit and, given the range of states a shocked system explores, call its own validity into question.

In order to fit a potential which can reproduce the dynamics of a shock calculation it may be possible to use a transferable neural network potential (NNP) which fits a neural network to a measurement of local structure in the system. The idea of a transferable neural network is that because it only relies on the local structure, it is possible to generate fitting data on a small system, then apply the network to a larger one [Behler, 2011]. An NNP has the advantage of not relying on functional forms and with enough flexibility and training data can theoretically model any potential accurately.

There are other approaches which could be used to speed up the DFT calculations, including techniques which sit directly on top of the DFT framework, such as "On the fly potentials" [Csányi *et al.*, 2004]. Such techniques can promise several orders of magnitude of speed-up compared to pure DFT, however, these approaches would still likely be limited in scale to a solvable DFT system.

3.4 This Work

In this work we will be using all of the potentials described in detail in §§3.1 & 3.2 as a test of the robustness and applicability of the methods to different systems. We hope to be able to use DFT accuracy in shock-wave calculations and be able to extract and extrapolate these results to real-world systems.

In doing this, we will also be exploring the applicability of a NNP to extreme systems, where matter is at extreme temperatures and pressures and in ordered and disordered phases simultaneously. This requires the neural network approach is sufficiently flexible to cope with a variety of states, which may require a larger or specially constructed data-set to cover all eventualities.

Chapter 4

Developments in this work

4.1 Potential

As noted in (§3.1) a new parametrisation for the short-ranged correction to the BKS potential has been calculated by fitting a 6-2-1 potential to the point of inflexion of the BKS in the style of Farrow [2009] with new values.

4.2 Hugoniostat

The Hugoniostat is a method developed originally by Maillet and Bernard [2001] in order to equilibrate a molecular dynamics system to the state of maximal shock by means of a thermostatting integrator. They called this method, which compressed the system instantaneously and then held the volume fixed in the manner of other such ensembles, the NVHug (constant particle number, constant volume, constant Hugoniot relation).

This was later extended [Ravelo *et al.*, 2004] to allow for a thermo-barostatted system, which they found provided greater robustness and correspondence to experimental values, with the added advantage that the applied pressure was a more experimentally relevant property than that of the volume difference between the unshocked and shocked material.

In this work, we have extended these methods and added modifications to make the Hugoniostat approaches more viable for both empirical and *ab initio* calculations, but with a particular focus towards *ab initio*.

4.2.1 Improvements to the Hugoniostats

4.2.1.1 Nosé-Hoover Hugoniostat

The Nosé-Hoover approach to the Hugoniostat was described by Maillet and Bernard [2001]. We have implemented this, along with the extensions as proposed in Ravelo *et al*. [2004] and constructed a time-reversible splitting of the integrator, as described in Tuckerman *et al*. [1992]. This integrator is similar to the Liouvillian formulation of the standard Nosé-Hoover integrator. The benefits of this are described in §2.4.2.

Algorithm 1 The Liouvillian derived Velocity Verlet integrator for the Nosé-Hoover Hugoniostat

Input: Cell state at t
Output: Cell state at $(t + \Delta t)$
{Velocity Verlet Step 1}
calculate pressure and energy
calculate $\dot{\chi}$
update χ with new $\dot{\chi}$
check quenching
update velocities and positions
calculate new forces
{Velocity Verlet Step 2}
calculate new pressure and energy
calculate new velocities
calculate new $\dot{\chi}$
update χ with new $\dot{\chi}$
check quenching

4.2.1.2 Langevin Hugoniostat

The NVHug Langevin formulation was alluded to in Maillet and Stoltz [2008], though was not stated in a form which could be implemented using instantaneous system properties (§2.4.9.2)

We have derived a means of calculating a Langevin integrator following the same scheme as the Langevin integrator already present in CASTEP (§2.4.7.2), though the temperature is replaced by a Hugoniot estimator (Eq. 2.74). The advantage of a Langevin thermostat rather than an Nosé-Hoover formulation is that it is guaranteed to be ergodic (§2.4) by the nature of the Gaussian fluctuations.

The EoM that govern the Langevin Hugoniostat are:

$$\dot{\mathbf{r}}_i = \frac{\mathbf{p}_i}{m_i} \tag{4.1}$$

$$\dot{\mathbf{p}}_i = \mathbf{F}_i - \underbrace{\gamma \mathbf{p}_i}_{\text{Damping Term}} + \underbrace{\sqrt{\frac{2m_i k_B T \gamma}{\Delta t}} N(0,1)}_{\text{Fluctuation}} \tag{4.2}$$

$$\dot{T} = \frac{-\Delta t T_0}{\nu C}(E(t) - E_H(t)) \tag{4.3}$$

where γ is a coupling constant which determines the decorrelation time of the system (i.e. the time over which the velocities of the particles may be considered no longer correlated), ν determines the coupling of the Hugoniostat to the temperature, T_0 is the pre-shock temperature, used as a scaling to preserve units, C is a scaling constant in units of energy to conserve system size independence.

This scheme has been implemented for both the constant-volume and constant-pressure Hugoniostats.

4.2.1.3 Nosé-Hoover-Langevin Hugoniostat

By an identical scheme to the Langevin approach, we can construct a Nosé-Hoover-Langevin-style integrator (§2.4.7.5)[Leimkuhler *et al.*, 2009] for the NVHug scheme, which we believe should be more robust to poor coupling than the standard Nosé-Hoover formulation and overcome the ergodicity problem presented by the Nosé-Hoover formulation, while also preserving more of the deterministic nature of the motion of the atoms, especially with regard to the direction of motion which can be disturbed by Langevin dynamics.

The EoM that govern the Nosé-Hoover-Langevin Hugoniostat are:

$$\dot{\mathbf{r}}_i = \frac{\mathbf{p}_i}{m_i}, \tag{4.4}$$

$$\dot{\mathbf{p}}_i = \mathbf{F}_i - \eta \mathbf{p_i}, \tag{4.5}$$

$$\dot{\eta} = \frac{p_\eta}{Q}, \tag{4.6}$$

$$\dot{p}_\eta = \frac{1}{Q}\left(\sum_{i=1}^{N} \frac{\mathbf{p}_i^2}{m_i} - dNk_BT\right) - \underbrace{\exp\left(-\tfrac{\Delta t}{\sigma}\right) p_\eta}_{\text{Damping Term}} + \underbrace{\sqrt{\frac{k_BT}{Q}\left(1 - \exp\left(-\tfrac{2\Delta t}{\sigma}\right)\right)} N(0,1),}_{\text{Fluctuation}} \tag{4.7}$$

$$\dot{T} = \frac{-\Delta t T_0}{\nu C}(E(t) - E_H(t)) \tag{4.8}$$

This scheme has also been implemented for both the constant-volume and

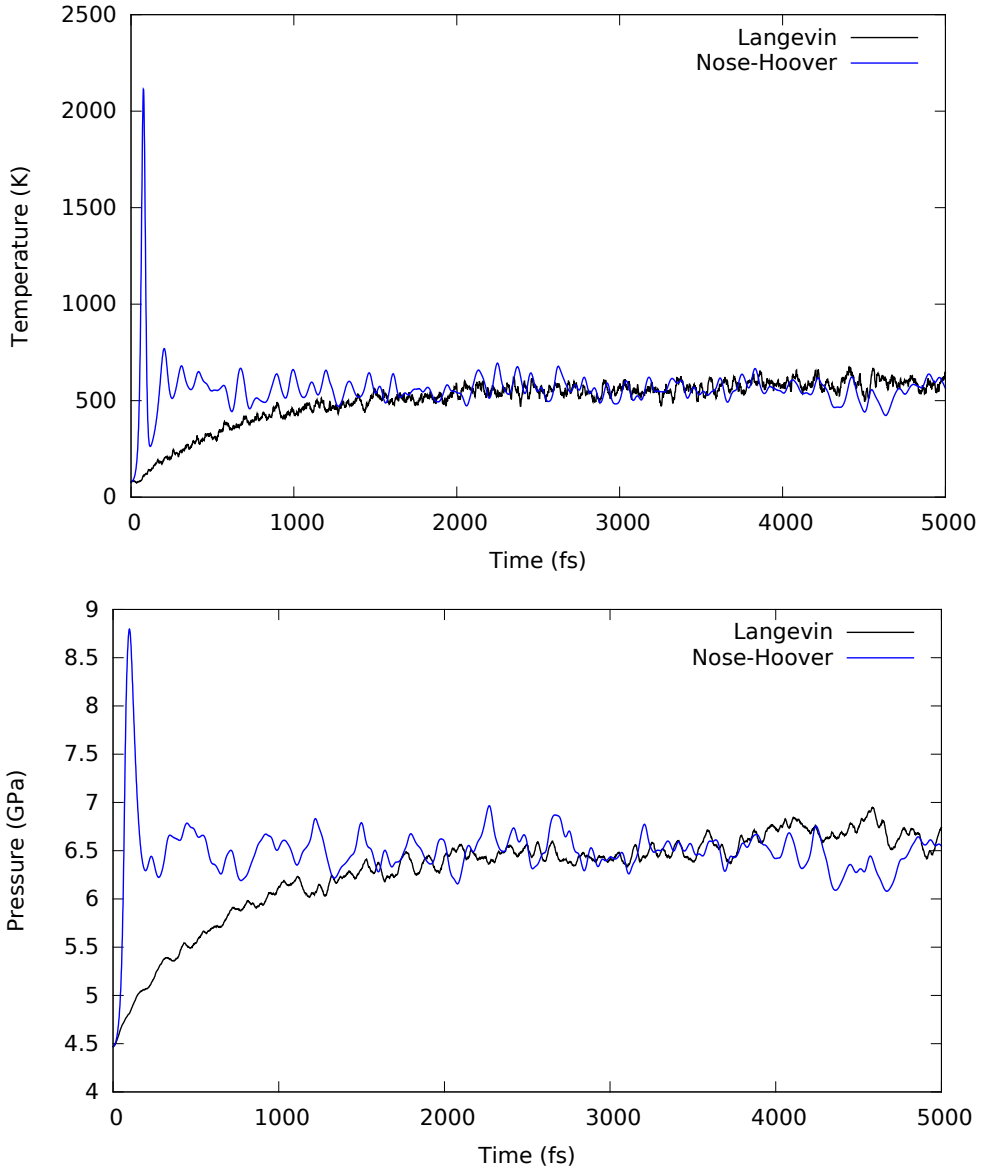

Figure 4.1: A comparison of the convergence of the NVHug Nosé-Hoover and NVHug Langevin to the Hugoniot state. Note the lack of a transient state in the Langevin formulation. Using more advanced damping and quenching techniques (§4.2.2.1 and §4.2.2.2) the convergence rate of both can be significantly increased and transients removed.

constant-pressure Hugoniostats.

4.2.2 Extensions

Due to the nature of plane-wave density functional theory (DFT) calculations and the way in which the forces are calculated (§3.2), DFT can be very susceptible to rapid changes in structure and can become unstable at high temperatures, and if atoms become close enough the fundamental assumptions of non-polarisability of core electrons becomes invalid in DFT.

DFT is also expensive to calculate compared to empirical force-fields, and so wasting as little calculation as possible is essential. It is not feasible to perform a large number of DFT simulations as trial runs before formulating the final calculation, hence it is necessary to construct a methodology which is both robust and predictable from the outset. This is very difficult to achieve in a complex and variable system such as a shock-wave.

We present here several of the modifications we have made to account for these problems in DFT calculations.

4.2.2.1 Damping

As was suggested in Ravelo *et al*. [2004] it is possible to achieve a more rapid equilibration to the Hugoniot temperature through applying a damping to the Nosé-Hoover formulation of the Hugoniostat, such that the equation for the update (Eq. 2.72) becomes:

$$\dot{\chi} = \frac{1}{\nu C}(E(t) - E_H(t)) - \beta_H \chi, \tag{4.9}$$

and similarly for the update (Eq. 2.88) of the NPHug formulation:

$$\dot{\eta}_\alpha = \frac{\nu_p}{D}(P_{\alpha\alpha}(t) - \sigma_{\alpha\alpha}) - \beta_p \eta, \tag{4.10}$$

where β_H and β_p are user-defined damping coefficients for the heat-flow and barostat piston respectively, chosen to bring about critical damping to the Hugoniot state.

These have been implemented into CASTEP, but an equivalent idea for the Langevin implementation is difficult to formulate given the target temperature is not 0, but a finite, unknown value (§4.2.1.2).

To overcome this limitation, we have taken ideas from a modified bisection search and have developed a method which modifies the coupling factor. If

we consider an inversion of direction to mean that we have over-shot the ideal target value:

$$\text{if } \dot{T}^{n-1}\dot{T}^{n} < 0 \text{ then:} \qquad \nu_H \rightarrow \beta_H \nu_H, \tag{4.11}$$

where superscript n refers to the time-step.

This serves to slow the dynamics of the temperature and attempts to minimise the overshooting effect, while still leaving the system free to explore and modify temperatures. More advanced methods could be implemented in order to apply an adaptive step-size method to the dynamics, however, as an initial smoothing mechanism this approach is found to be sufficient (Fig. 4.2).

We can also see that the rapid convergence techniques can be applied across the entire Hugoniot range for rapid convergence (Fig. 4.3). Using a β_H of 0.3 with with the Langevin NVHug scheme. The initial coupling can be modified to reduce the initial-overshoot at the expense of a slower convergence to the initial temperature.

4.2.2.2 Quenching

In order to improve the equilibriation time of the Hugoniostat, inspired by rapid convergence techniques of geometry optimisation [Probert, 2003], we have implemented a quenching scheme for the Hugoniostat. This scheme also helps reduce transient effects (Fig. 4.4) before equilibriation significantly, the magnitude of which can lead to instabilities in *ab initio* calculations.

If we consider the Hugoniostat variable (χ) as a velocity of the temperature (T) and the change in the Hugoniostat variable ($\dot{\chi}$) as the acceleration, we can apply a quenching scheme whereupon:

$$\text{if } \chi\dot{\chi} < 0 \text{ then:} \qquad \chi = 0 \tag{4.12}$$

This is permissible because the Hugoniostat variable (χ) is not directly affecting the system, but only modifying a fictitious variable which in turn affects the dynamics system. This first order separation from the simulation itself means that the system is still free to continue to explore configurations as it would if unquenched. It is also generally made more acceptable given that the transient data is usually excluded from calculation of properties anyway, deemed the "equilibriation phase", the quenching can be restricted so that it is only active during the specified equilibriation time and the system acts under the pure Hugoniostat after this time.

We have also implemented this idea for quenching the piston variable of the constant-pressure Hugoniostat. This means that if the system is especially far from the equilibrium point, the momentum of the piston will not cause drastic over-compression causing the system to go unstable, as can be the case with *ab initio* calculations should atomic overlap occur.

Another advantage of this is the ability to initialise the piston with an initial momentum which is far more than the system could normally account for using damping or slowing the piston through Eq. 2.88. This allows for much more rapid convergence of the cell volume to the compressed cell volume

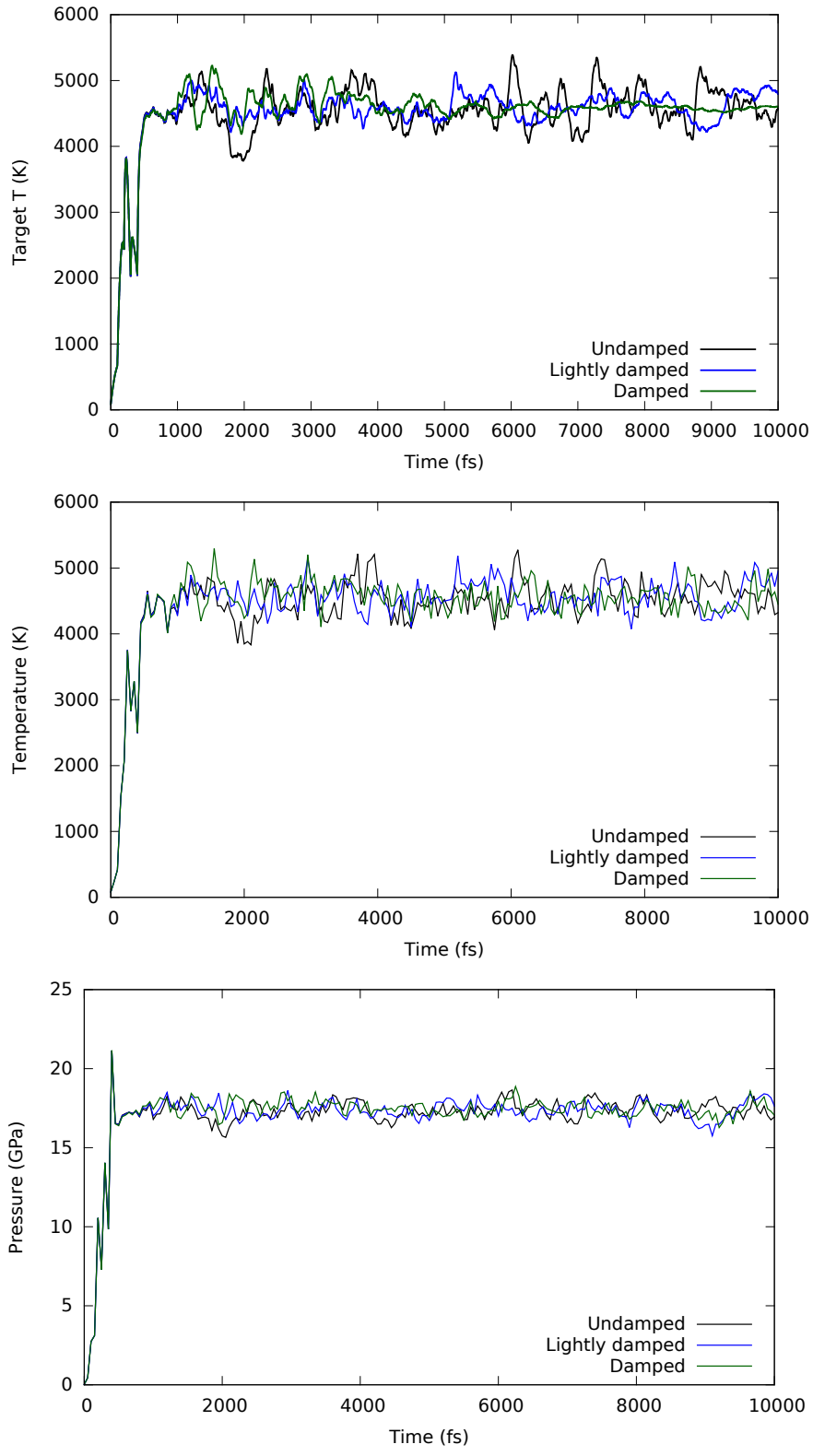

Figure 4.2: Effects of the damping on the Langevin scheme (Eq. 4.2) on a 500-atom Lennard-Jones cell at a 60% compression with an overly strong Hugoniostat coupling (ν_H) of 0.1fs^{-1} and a damping factor (β_H) of (Undamped) 0.0, (Lightly Damped) 0.1, (Damped) 0.3, (Top) Convergence of the target temperature to that of the Hugoniot temperature is accelerated and smoothened. (Middle, Low) Convergence of the system properties, with a sample every 50fs. Note that the mean of the system properties are effectively unchanged, but with lower variance.

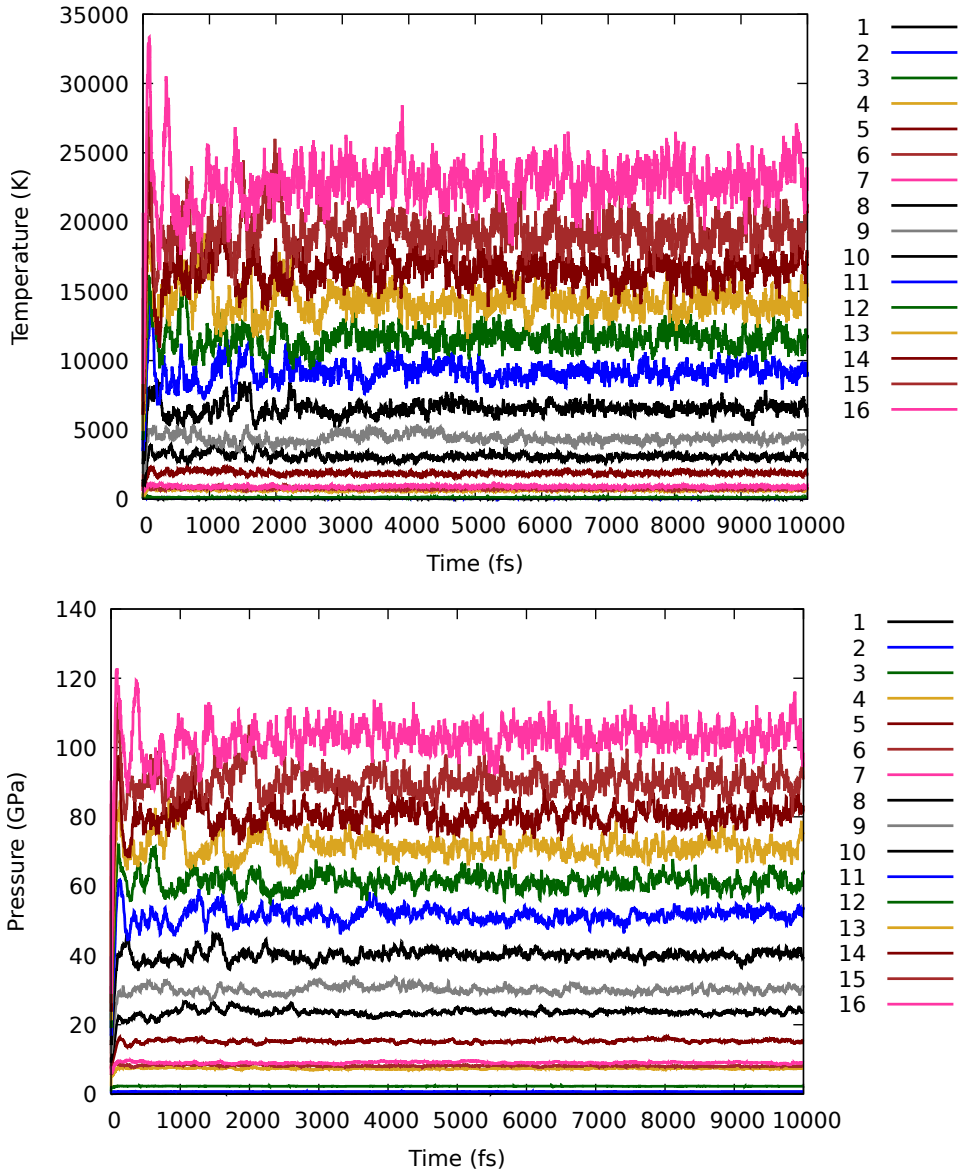

Figure 4.3: Plot showing the accelerated convergence of the Langevin Hugoniostat method with moderate damping for 864-Atom Lennard-Jones FCC crystal over first $10ps$ across entire Hugoniot. Line labels correspond to the predictor (§4.2.2.4) steps.

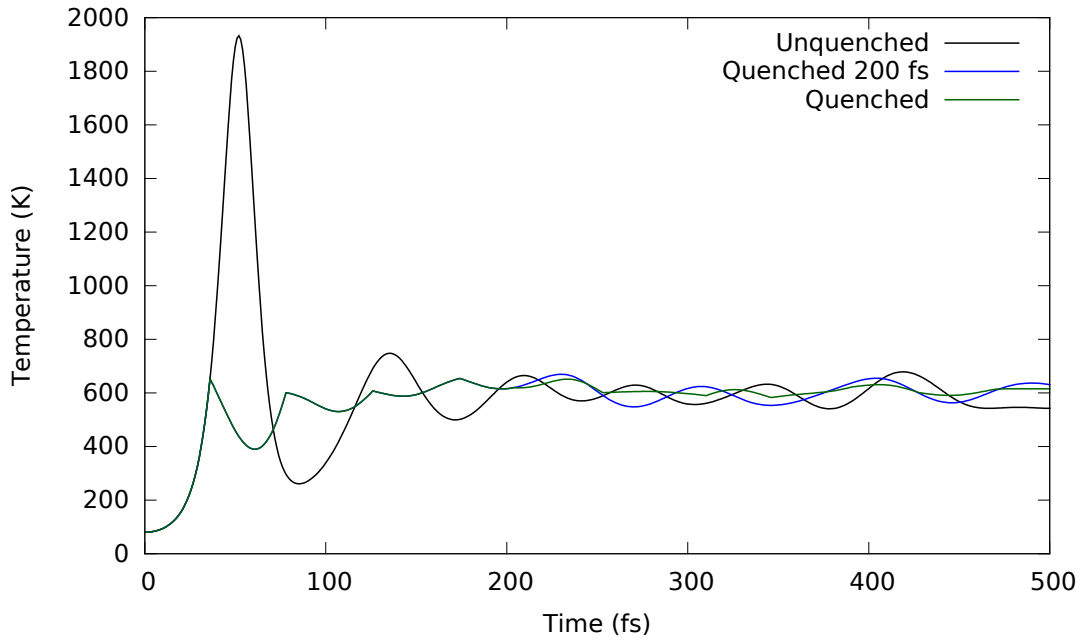

Figure 4.4: The effects of quenching on the temperature of a 30% compressed 500-atom Lennard-Jones system, unquenched line (black) shows a large transient initially, the quenched lines (blue and green) show the elimination of this transient at the expense of "unphysical" temperature dynamics, which are eliminated when the quenching is turned off (blue) after equilibration. It should be noted that all three converge to the same temperature.

without damaging the dynamics by applying overly strong piston coupling.

$$\text{if } \eta\dot{\eta} < 0 \text{ then:} \qquad \eta = 0 \tag{4.13}$$

While it may be argued that this is more directly affecting the system than the quenching of the Hugoniostat variable, it is still only used during the equilibriation period, and should still not alter the system's exploration of phase-space.

4.2.2.3 Steady Compression

As suggested by Ravelo *et al*. [2004] we have implemented a scheme which allows the system to reduce the transient of the shocked system by means of a steady compression for an NVHug calculation. This scheme drives the system towards the compressed equilibrium state by performing work through the thermostat at a steady pace while reducing the work via compression to a slower rate, the effect of this can be seen in Fig. 4.5.

$$\dot{h}_{\alpha\alpha} = C \tag{4.14}$$

where $h_{\alpha\alpha}$ is the cell vector in the direction of compression and C is described below.

The scheme does so by compressing by a finite, fixed amount after a specified number of time steps have elapsed (the reason for this block compression is similar to those for the extrapolation scheme below §4.2.2.4), to cause the compression to match either a specified strain rate or to make the compression occur over a given period of time.

$$C = \eta \qquad \text{or} \tag{4.15}$$

$$C = \frac{\varepsilon}{\varepsilon_t \Delta t} \tag{4.16}$$

The Hugoniostat integrator operates as though the volume is already at the target final volume in order to improve equilibriation rates.

4.2.2.4 Predictor

Due to the nature of DFT, where a lot of important parameters are tied to the simulation cell, it is generally more efficient to use a fixed-cell calculation in order to reduce the computational expense of recalculating all the properties

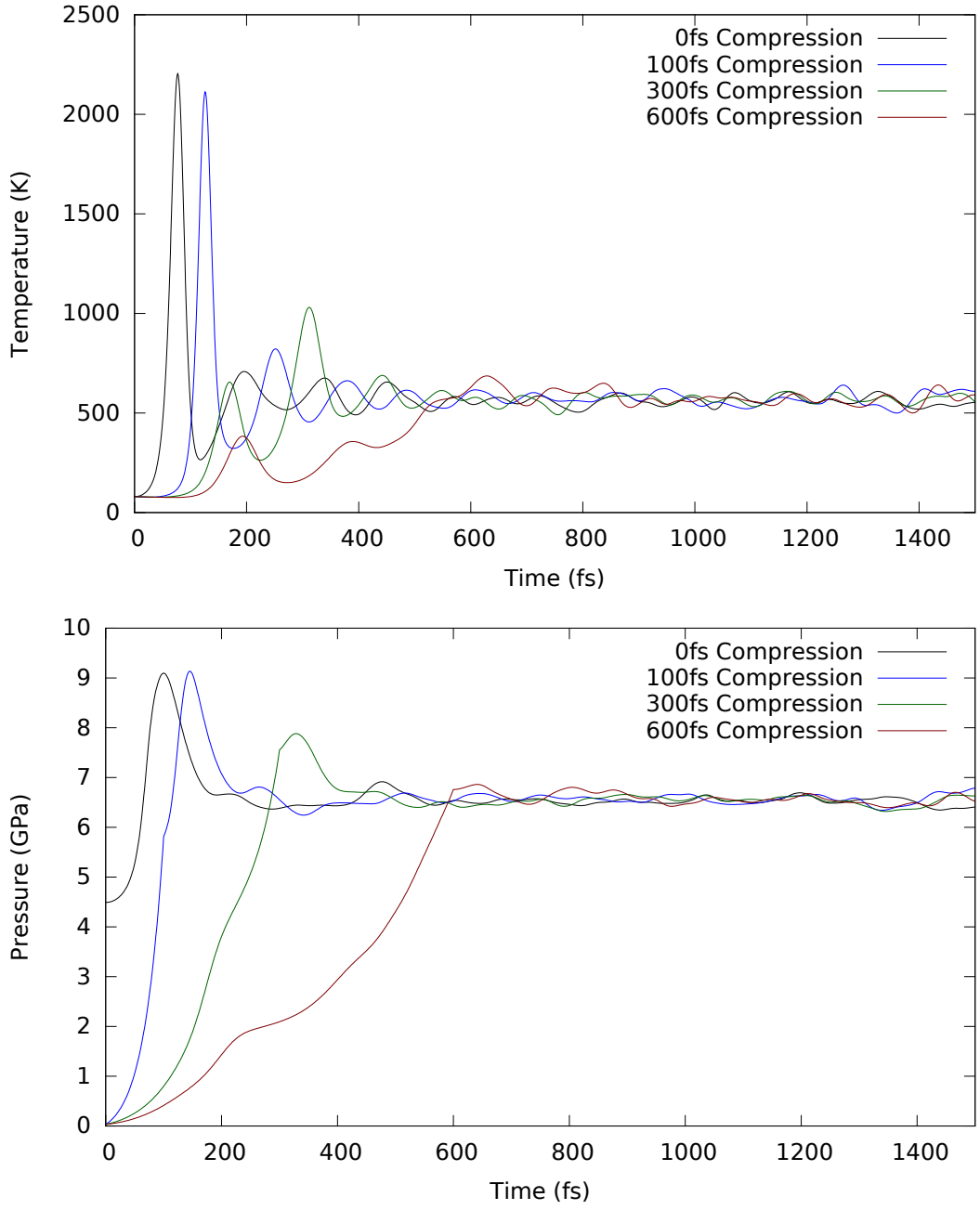

Figure 4.5: The effects of steady compression on equilibriation of a 30% compressed 500-atom Lennard-Jones system using a Nosé-Hoover integration scheme. Note the reduction, then elimination of the initial transient as the compression is spread over longer times, and also that all calculations converge to the same value.

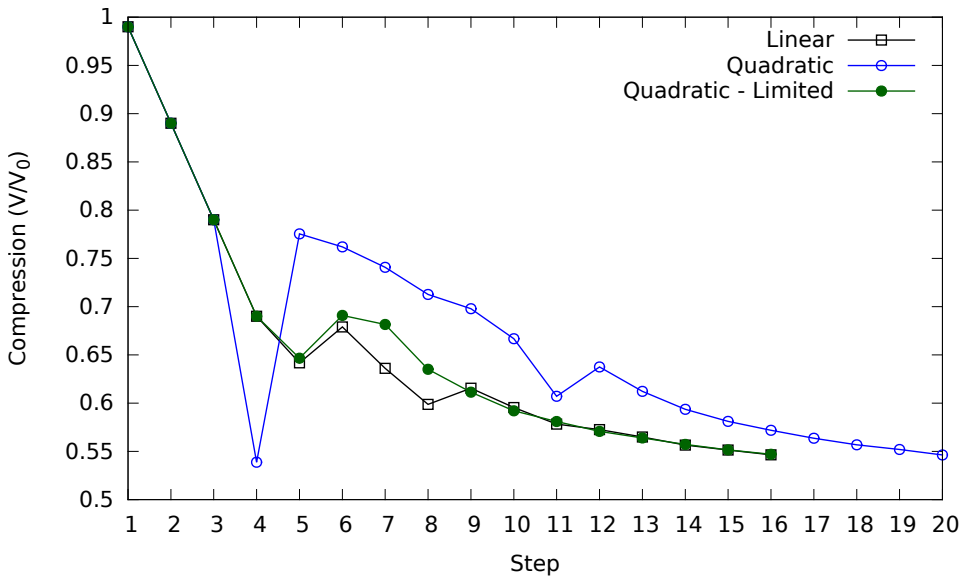

Figure 4.6: Comparison between different predictor formulae, purely linear (Black) and quadratic (Blue & Green), for an 864-atom Lennard-Jones FCC crystal. Due to the softness of the Lennard-Jones potential, the polynomial predictor does not have accurate enough information when it switches from the linear regime (Step 2), this is remedied by applying a limit to the maximum compression (10%) which can be applied at each step (Green). Note that the linear predictor always has this limit applied.

which are related to the cell.

To this end, we have developed an extrapolation algorithm in order to calculate a series of constant-volume Hugoniostat runs at even sampling along pressure space of the Hugoniot in order to construct the full Hugoniot in a fire-and-forget manner.

Given a target pressure and a number of desired steps, the predictor is able to automatically trace the Hugoniot curve to minimise the amount of effort needed from the the user. It is capable of calculating a number of Hugoniot properties such as the coupling of the Nosé-Hoover Hugoniostat and estimating the temperature, speed of sound and speed of shock in the target system, and in principle a lot more such as new k-point grids.

A linear and a quadratic predictor were implemented and tested (Fig. 4.6). This was because until the quadratic predictor has sufficient information to function (an underdetermined equation), it uses a linear estimator. The linear predictor only ever uses the previous two data points, whereas the quadratic scheme uses a user-specified length of history.

The algorithm and approaches used in this section are described in Algs. 2 & 3.

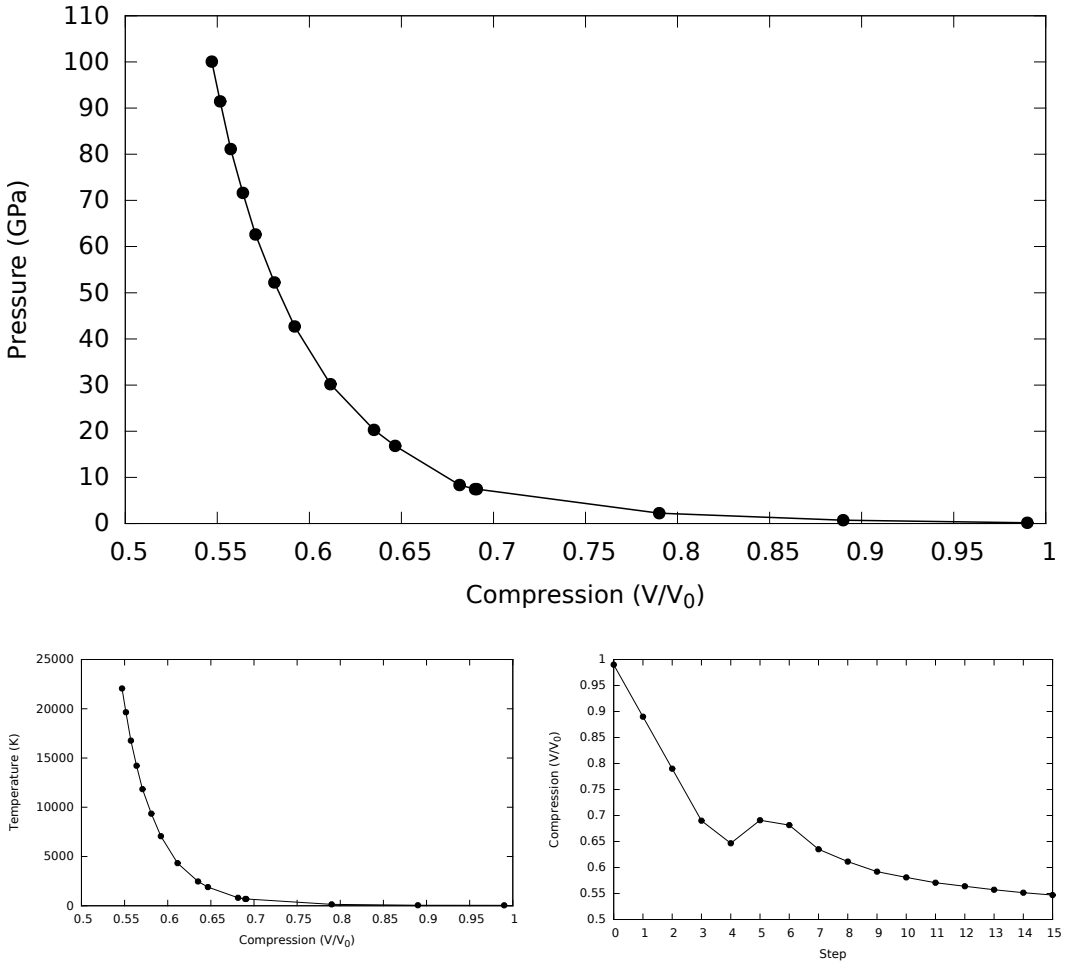

Figure 4.7: Result of the Hugoniot predictor algorithm for an 864-atom Lennard-Jones cell using the Langevin integrator. (Top) Compression against pressure, (Bottom-Left) Temperature against pressure, (Bottom-Right) Compression against predictor step. Calculations were performed using a 2nd order polynomial predictor aiming to step from 0-100GPa in steps of 10GPa, with a permitted error of 20% to the target. 19 steps were taken, though this could be reduced by skipping state points which have been previously explored.

Algorithm 2 Hugoniostat predictor algorithm, with fail-safe, reuse, and Nosé-Hoover coupling sections. $\leftarrow$ implies push on the front of the array (unshift). take_predictor_step is described in Alg. 3

Input: Cell state at t_{final}, history
Output: New cell state
  if initialising **then**
    history $\leftarrow$ [1, P_0, T_0, E_0]
    save backup of original cell
    compression initialised to some small value
    if restart **then**
      history $\leftarrow$ [ε, P, T, E] {Read all old history}
    end if
  end if
  calculate average P,T and E of previous predictor step
  history $\leftarrow$ [ε, P_{av}, T_{av}, E_{av}]
  print [ε, P_{av}, T_{av}, E_{av}]
  if $\left|P_{av} - P_{target}\right| < \Delta P$ **then**
    i = steps taken {Check prior history to avoid repeats}
    while i > 0 **do**
      if $\left|\text{history[i][}P\text{]} - P_{target}\right| < \Delta P$ **then**
        $P_{target} += P_{step}$
        i = steps taken
      end if
      i = i -1
    end while
  end if
  ε, deriv = take_predictor_step(P_{target}, history, V_0, ε)
  if $\varepsilon < 0$ **or** $\varepsilon > 1$ **then**
    abort Instability in predictor
  end if
  if reuse **and** history[1][ε] $> \varepsilon$ **then**
    continue
  else
    reset cell to initial state
  end if
  compress cell to new volume and re-initialise molecular dynamics variables
  if Nosé-Hoover **then**
    $v_s = \sqrt{\text{deriv}/V_0}$
    tmpcoup $= \left(6\pi^2 \rho v_s^3\right)^{1/3}$
    coup = **max**(coup, tmpcoup) {Coupling can be unstable in early phases}
  end if

Algorithm 3 Algorithm to calculate the next step in the Hugoniostat predictor for general polynomial and linear predictors. Other fitted forms could easily be used.

Input: P_{target}, history, V_0, compression_in
Output: compression, derivative
  steps taken = steps taken $+1$
  if steps taken $> 2 \times$ steps requested **then**
    abort Too many steps taken {Avoid infinite runs}
  end if
  ndata = **min** (steps taken, history length)
  if polynomial **and** steps taken $>$ poly order + 1 **then**
    coeffs = polynomial_regression(history[1:ndata][ε], history[1:ndata][P], poly order) $\{a + bx + cx^2 \dots\}$
    compression = solve_poly(P_{target}, coeffs) :=
    return max$\left(\frac{-b \pm \sqrt{b^2 - 4c(a - P_{target})}}{2c}\right)$ {If poly order = 2 (i.e. quadratic)}
    derivative = -poly_deriv(compression) := {Negative because compressing not expanding}
    return $2c \cdot$ compression$+b$
  else
    coeffs = polynomial_regression(history[1:2][ε], history[1:2][P], 1) $\{a + bx\}$
    derivative = $-b$
    compression = compression -$\left(\frac{P_{target} - P}{a}\right)$
  end if
  if $|$compression $-$ compression_in$| >$ max_comp_step **then**
    compression = compression_in + max_comp_step$\times$**sgn**(compression - compression_in)
  end if

Modifications

Not-resetting states

We have also experimented with using the prior state of compression as the initial state for the next compression, rather than resetting the cell and recompressing at each step, in an attempt to eliminate transients entirely to initiate the newly-compressed system at more reasonable temperatures and configurations. Though this may restrict the explored states, due to the reduction of transient states, it can be reasoned that the state would likely pass through the states explored by the previous compression as part of the transient process.

Fail-safe

There is also a fail-safe mechanism built in, such that should there be a discontinuity in the Hugoniot (for example, due to a phase transition), the predictor will forget its history and build forward from that point. This detection is a simple mechanism which just ensures linearity such that as compression is increased, temperature and pressure increase correspondingly.

Coupling

In using the extrapolation, it was found that because coupling depends on the compression, it became impossible to simulate harder materials, as the static coupling would quickly cause calculations to become unstable.

Using the property of the coupling described by Maillet *et al*. [2000], that is that it relates to the Einstein frequency (ω_E) of the material for the Nosé-Hoover formulation, we constructed a mechanism for estimating the related Debye frequency (ω_D), based on the derivative of predictor function. The reason for not using the Einstein frequency itself (§2.5.7), is that the calculation of curvatures of potentials is expensive mid-calculation and not guaranteed to be accurate, especially for non-equilibrium states where the potential is not guaranteed to be in a harmonic region, while the predictor already stores all the relevant information for predicting the coupling.

$$v_s = \sqrt{\frac{B}{\rho}} \tag{4.17}$$

Where v_s is the speed of sound, B is the bulk modulus ($V\frac{\partial^2 E}{\partial V^2}$) and ρ is the density ($\frac{N}{V}$). The predictor corrector relates P and V (via ε) and allows us to

take a trivial derivative of the predictor's fitted function, which gives us:

$$\frac{\partial P}{\partial \varepsilon} \approx v_s^2 \tag{4.18}$$

Taking the formula for the Debye frequency [Debye, 1912]:

$$\omega_D^3 = \frac{6\pi^2 N}{V} v_s^3, \tag{4.19}$$

$$\omega_D = \sqrt[3]{6\pi^2 \rho v_s^3}, \tag{4.20}$$

which gives us a reasonable estimate for the coupling based on the material in its current state.

Though we have ideas for the prediction of the coupling of the Langevin Hugoniostat, based on the ratio between the uncompressed and the last Debye frequency as a scaling factor for the coupling, tests show that by using the damping approach this is rendered wholly unnecessary (Fig. 4.2) and so these approaches have not been implemented or tested.

Chapter 5

Argon Simulations

In this section we present the results obtained from a number of simulations of Argon using the Lennard-Jones pair-potential using both LAMMPS [Plimpton, 1995] and CASTEP [Clark *et al.*, 2005] and *ab initio* calculations from CASTEP.

Argon has been chosen as the test case of choice due to its simplistic and cheap potential and its well studied properties. Due to its inert nature as a noble gas it does not undergo any particular complex structural changes and its simple interactions mean that many properties can be estimated analytically.

5.1 NEMD

As discussed in previous sections (§1.5.3.1) the most obvious way to create a shock-wave in a system is to directly emulate the experimental set-up. In this case, we are constructing a flyer-plate experiment with a small block of material colliding with the experimental medium or direct NEMD.

All of the following NEMD calculations were performed using LAMMPS using the Lennard-Jones (6–12) potential. The simulation setup is based on a script by Guerrero-Miramontes, it uses a flyer plate with a constant velocity, which experiences no response forces from the bulk (i.e. is effectively infinitely massive) (Fig. 5.2), but interacts with the bulk via the Lennard-Jones potential, and so is softer than the momentum mirror approach which is known to be overly strong and produce unphysical shocks [Farrow, 2009].

Prior to the piston interaction, the cell is minimised in its bulk state, using a conjugate gradient minimisation scheme in which the box size is optimised, and the particles are allowed to relax with a $1ps$ NVE calculation. The system then collides with the piston, producing the impact (Fig. 5.1).

From these calculations it is trivial to extract certain Hugoniot properties as

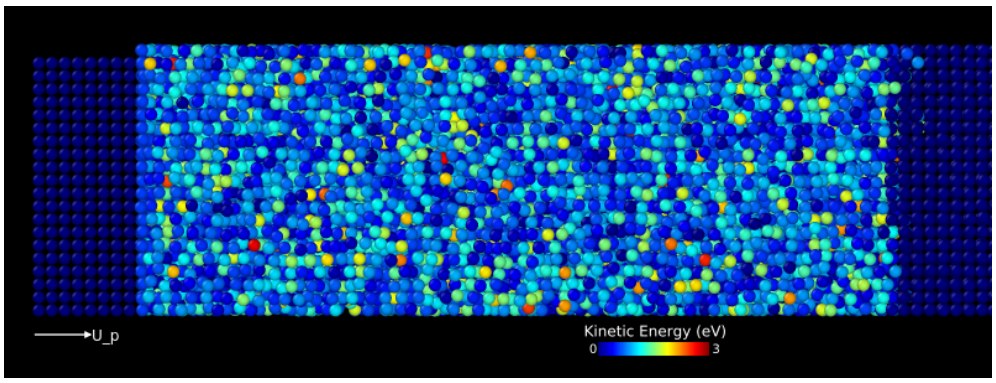

Figure 5.1: Snapshot of NEMD shock-wave in LAMMPS FCC Argon crystal. The colouration is the kinetic energy of the medium. The discontinuity in the kinetic energies (temperature) is clearly visible at the shock-front (the unshocked dark blue region at the right hand side).

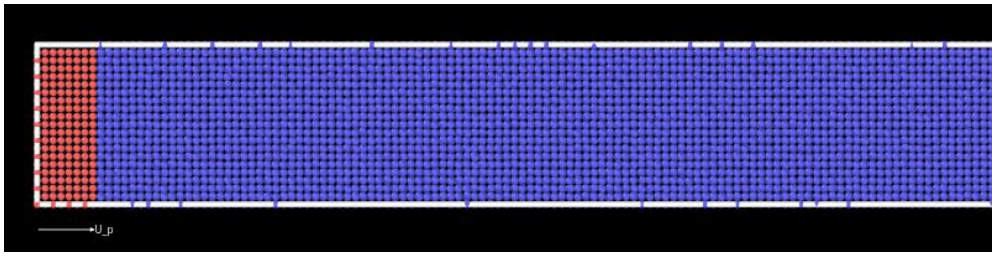

Figure 5.2: The initial system set-up for the LAMMPS NEMD shock. The flyer-plate (red) is launched into the system with a specified initial velocity and is set to feel no force from the bulk making it essentially infinitely massive.

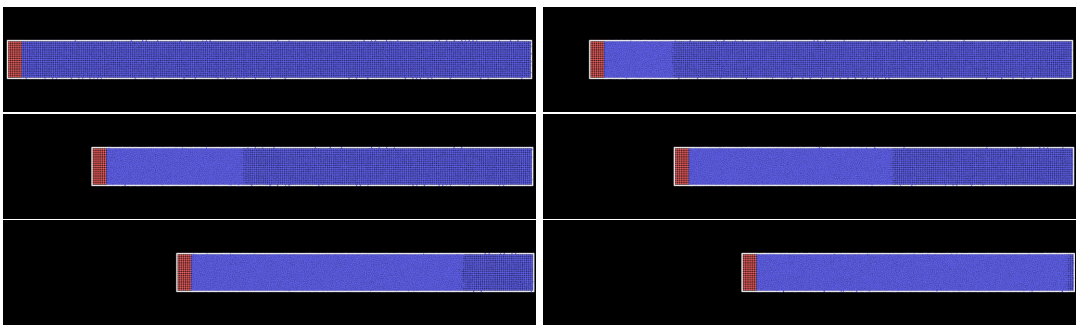

Figure 5.3: Series of snapshots of a 3km/s NEMD flyer-plate impact taken at $0ps$, $2ps$, $4ps$, $6ps$, $8ps$ and $9ps$ (maximum compression) respectively, showing the progression of the shock .

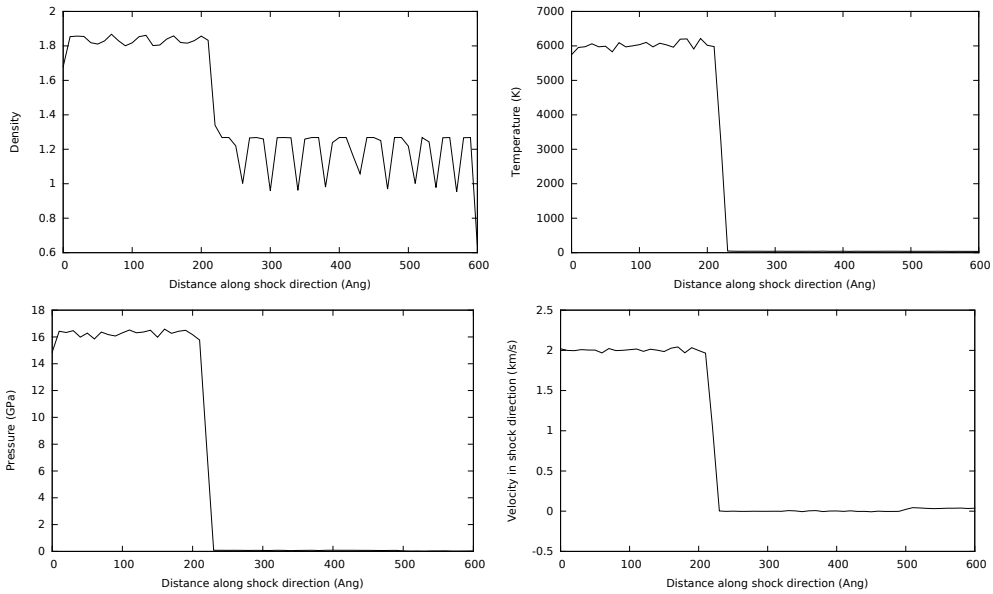

Figure 5.4: Examples of the shock discontinuity in four different system properties: (Top Left) Density, (Top Right) Temperature, (Bottom Left) Pressure, (Bottom Right) Velocity in the direction fo the shock. These samples are taken at 6ps from a 2km/s flyer plate impact, block averaged over atoms every 10Å in the direction of the shock.

they are directly measured in the calculation, including the shock- and particle-velocities, local pressure (calculated using the Voronoi cell of each particle, see §2.6.1), temperature, and density as the shock propagates. These are averaged along slices of the cell taken at regular intervals in the direction of the shock-propagation to produce these measurements (Figs. 5.4 & 5.5).

Using these discontinuities which show the location of the shock-front, by simply taking the difference between the locations of two shock-fronts at different times (Fig. 5.3), and dividing by the difference in time we find the shock-velocity which we can then plot against the particle-velocity in the direction of the shock, which gives us the u_s–u_p curves commonly obtained from shock experiments.

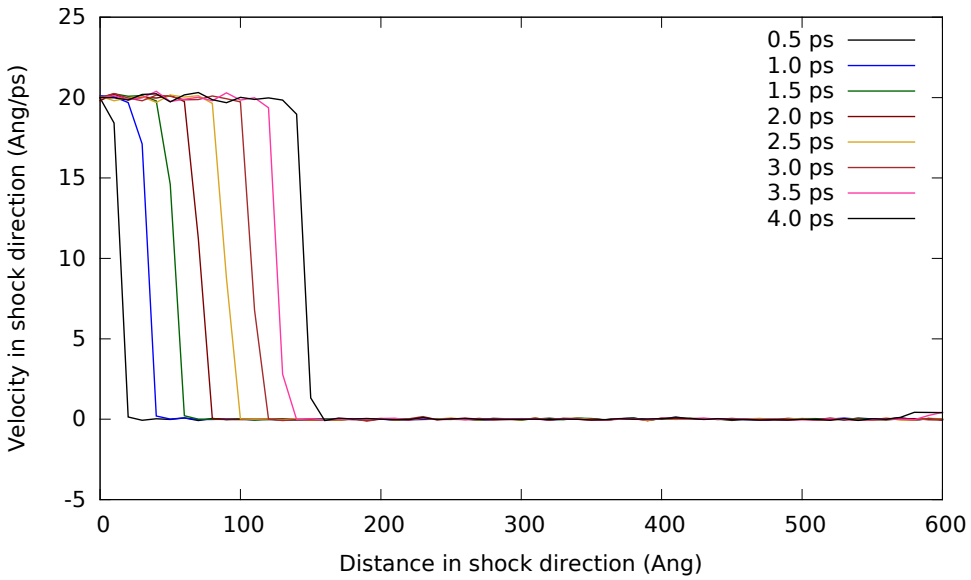

Figure 5.5: The velocity profile of a shock in a 2km/s (u_p) flyer-plate impact on a 42,000 atom Lennard-Jones argon FCC lattice. From this it is easy to measure the shock-front's velocity (u_s) as it tavels down the block by measuring the distance the discontinuity has travelled between samples.

5.2 Hugoniostat

In this section we explore the Hugoniostat approach to simulation of shock-waves. The calculations presented here were produced using the CASTEP and LAMMPS codes. The CASTEP runs may involve some of the more advanced rapid equilibration schemes described in (§4.2.2), which are unavailable in the NPHug scheme presented in LAMMPS. All calculations, however, are run to their required convergence to give a fair comparison between the approaches.

5.2.1 Convergence and Finite-size

It is essential in any molecular dynamics simulation that the system is able to be representative of the material of interest, and the Hugoniostat approach is no different. To this end, understanding the variation in properties based on the cell size and number of atoms is critical. A key requirement in shocks is the ability for the structure to respond appropriately to the injection of energy, and more atoms means that the structure has more degrees of freedom, and thus is more free to change with larger cell sizes.

One of the key properties calculated in the Hugoniostat molecular dynamics simulations is the Hugoniot temperature, which should be an intensive property (independent of the system size), but fluctuations become more pronounced as the number of atoms is reduced (Fig. 5.6). The statistical deviation

Supercell	Atoms	Temperature (K)	Pressure (GPa)
1x1x1	8	584.9±242.4	5.962±0.647
2x2x2	64	822.5±152.8	7.279±0.477
3x3x3	216	814.5±70.5	7.364±0.226
4x4x4	512	845.0±44.7	7.542±0.171
5x5x5	1000	829.1±30.7	7.520±0.101

Table 5.1: Table of calculated Hugoniostat temperatures and pressures at 30% compression, averaged over the last 7000fs for supercells of Lennard-Jones FCC crystals with corresponding standard deviation.

in the temperature reduces proportionally to the square root of the number of atoms [Landau and Lifshitz, 1980]:

$$\Delta T = \frac{T}{\sqrt{N}}. \tag{5.1}$$

The pressure of the system is another property which is also essential to the determination of the Hugoniot, fluctuations in the pressure usually correlate with the fluctuations in the temperature as the temperature is a measure of the kinetic energy of the system and the kinetic component of the pressure is calculated in a similar way (§2.5.3). If we assume the ideal gas law (which we deem reasonable given the Hugoniot equations rely upon an inviscid fluid):

$$PV = Nk_BT, \tag{5.2}$$

taking the total derivative:

$$\Delta(PV) = \Delta(Nk_BT), \tag{5.3}$$

$$P\Delta V + V\Delta P = Nk_B\Delta T + k_BT\Delta N + NT\Delta k_B, \tag{5.4}$$

and knowing that V and N are held constant by the system and k_B is a constant we find that:

$$\Delta P \propto \Delta T, \tag{5.5}$$

and so we can surmise:

$$\Delta P \propto \frac{1}{\sqrt{N}}. \tag{5.6}$$

5.2.2 Runs

The reference implementation for the Hugoniostat is the NPHug implementation in the LAMMPS code [Plimpton, 1995], to demonstrate the efficacy of our

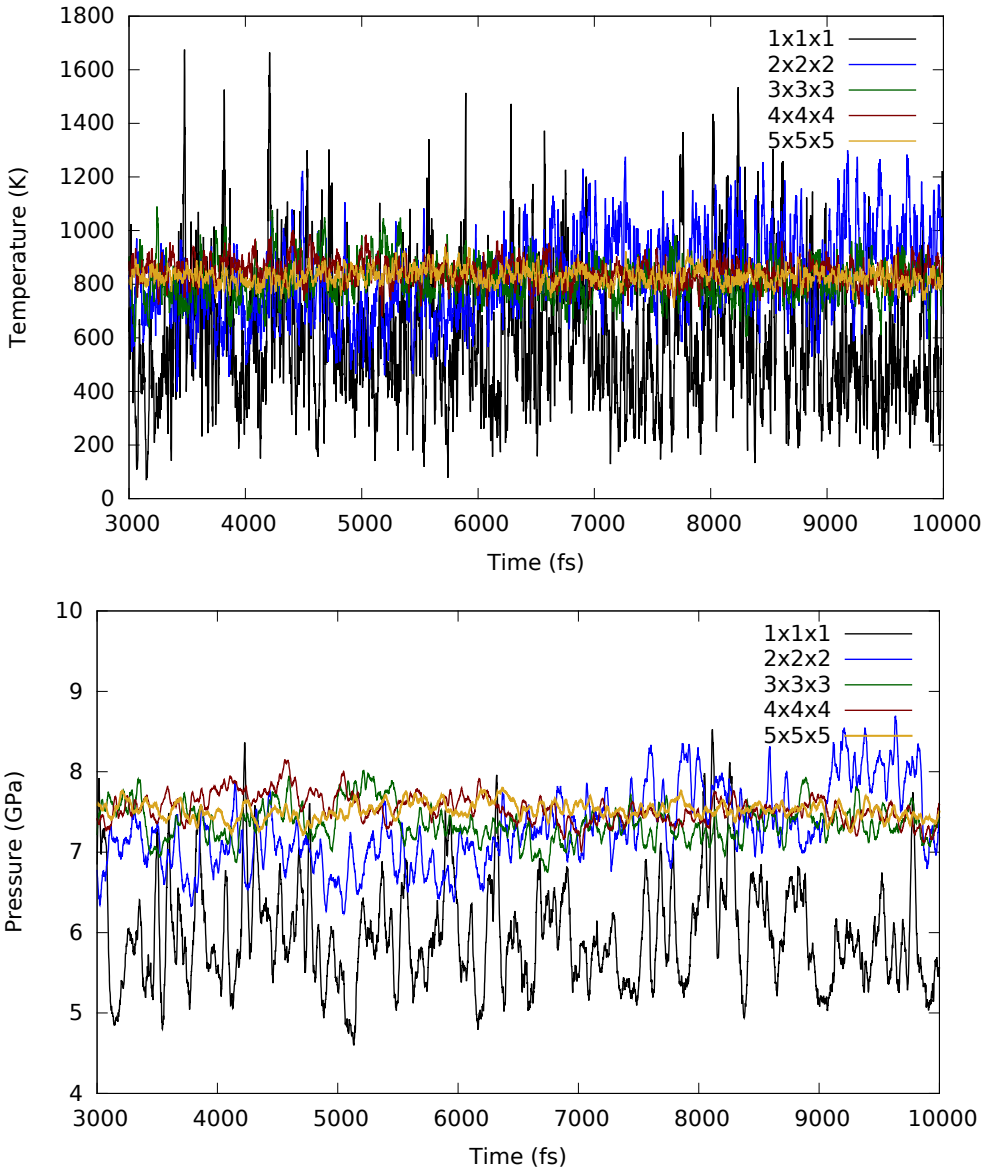

Figure 5.6: A demonstration of the effects of finite cell-size on temperature (top) and pressure (bottom) fluctuations from a 30% compression using the NVHug Langevin formulation (§4.2.1.2). A series of 5 runs with different sizes of supercells of an initially perfect FCC Lennard-Jones cell. 1x1x1 refers to the 8-atom conventional cubic unit-cell and others are respectively larger (64, 216, 512 and 1000 atoms respectively).

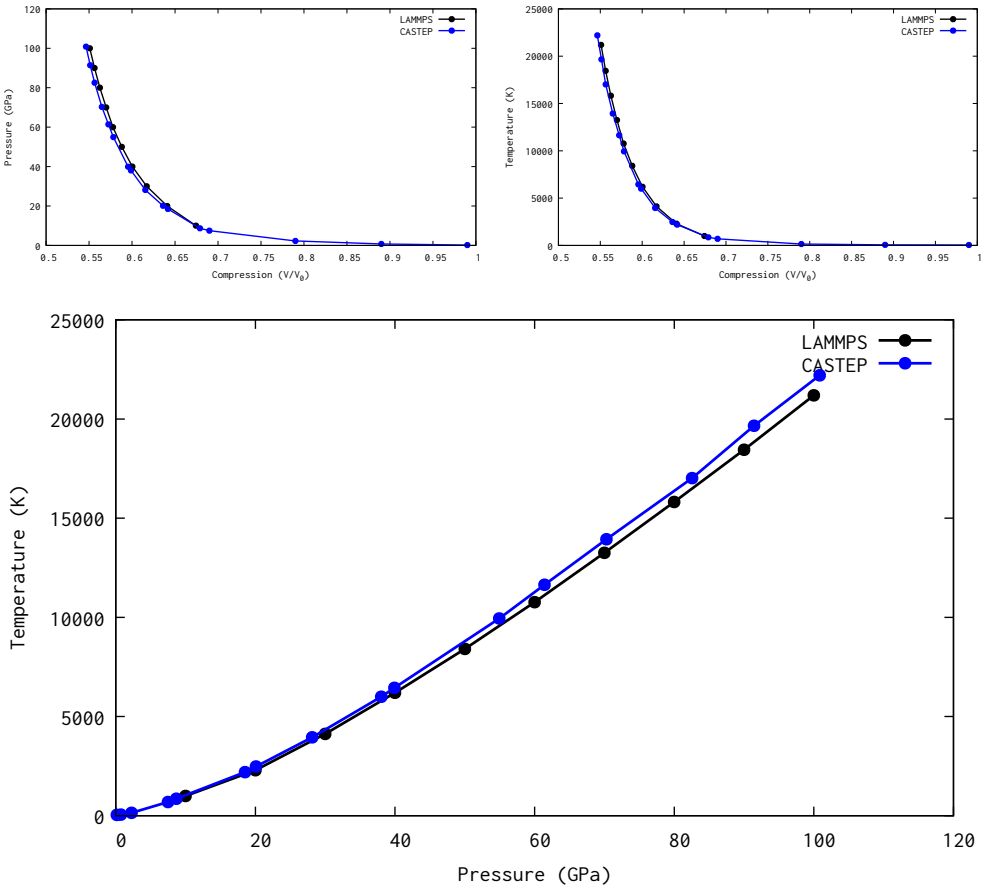

Figure 5.7: Plot to demonstrate agreement between this work's implementation of the Hugoniostat and a reference implementation in the LAMMPS code. The results of CASTEP are using an 864-Atom Lennard-Jones perfect FCC cell and the Langevin NVHug linear predictor method, attempting to reach 100GPa in steps of 10GPa. LAMMPS' results are those of a series of Nosé-Hoover NPHug on a 2048-atom Lennard-Jones FCC cell, taking steps in pressure of 10 GPa.

implementation we first must verify that our results agree with the standard implementation.

From Fig. 5.7 we can see that though there are slight deviations at higher compressions, these deviations are well within expected fluctuations, and are most likely due to the different scales of the calculations. As can be seen in Fig. 5.8 the rates of convergence differ greatly between the two calculations, due to the approaches taken in this work, with its focus on DFT simulations where longer runs are simply infeasible.

We find that our NPHug follows strongly in agreement with the NVHug predictors, despite being based on different algorithms and having different approaches. It is also in good agreement with the LAMMPS reference calculation, which further affirms our implementation is correct.

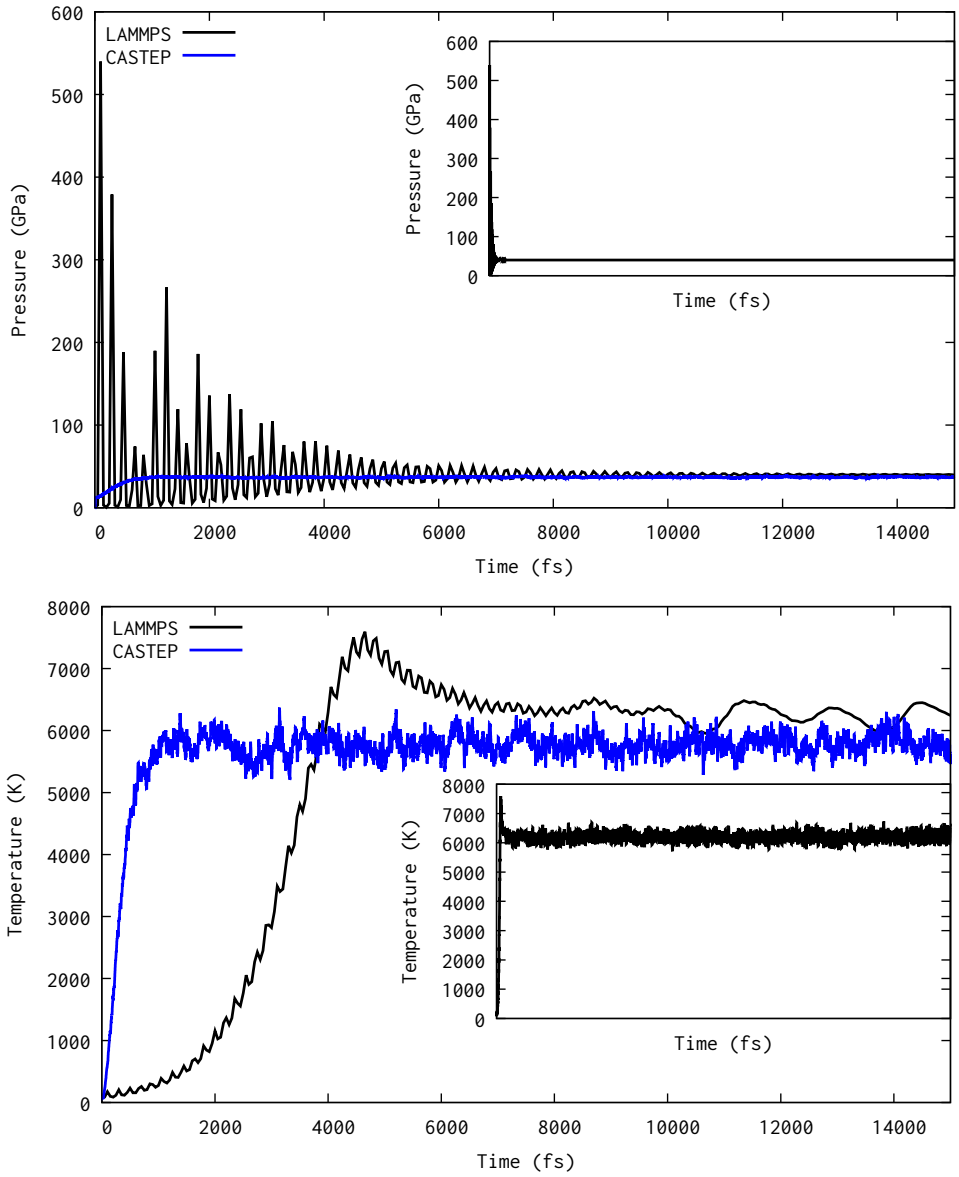

Figure 5.8: Plot to demonstrate agreement between this work's implementation of the Hugoniostat and a reference implementation in the LAMMPS code. The results of CASTEP are using an 864-Atom Lennard-Jones perfect FCC cell and the Langevin NVHug method at 60% compression (Approx. 36GPa). LAMMPS' results are those of a Nosé-Hoover NPHug on a 2048-atom Lennard-Jones FCC cell at 40GPa. The inset graphs show the full trajectory of the 500,000fs LAMMPS run to demonstrate its convergence.

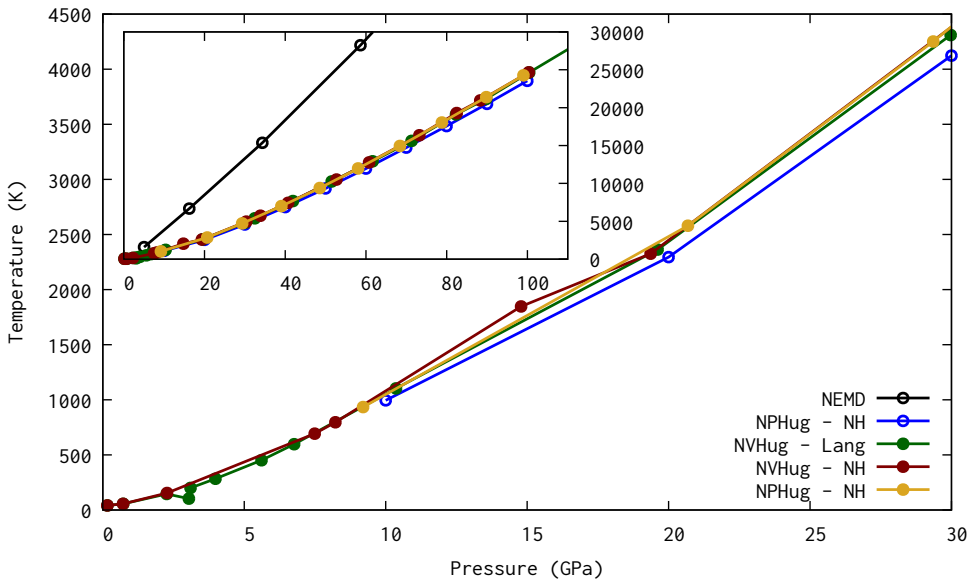

Figure 5.9: Pressure-Temperature Hugoniot plot for the different approaches implemented in CASTEP. The two NVHug methods are using the Langevin and Nosé-Hoover thermostat styles, the NPHug calculation is using the Nosé-Hoover approach in both LAMMPS and CASTEP. Solid circles denote CASTEP, hollow circles denote LAMMPS. Due to its extremity, the NEMD data is shown only on the inset.

5.2.3 Hugoniot

One of the key properties that we wish to be able to extract from our calculations is the Hugoniot. This equation of state can be plotted in many planes, the most common being the pressure–temperature (Fig. 5.9) and the shock velocity–particle velocity (Fig. 5.10).

Fig. 5.9 shows the Pressure-Temperature Hugoniots generated by each of our methods in LAMMPS and CASTEP. There is a strong agreement between most of the methods, the one exception being the NEMD approach, however, this may be due to an issue in the way the temperature is calculated in the sample slices.

The shock- and particle-velocities are direct observables from an NEMD calculation (Fig. 5.5), and they can be extracted from a Hugoniostat calculation via:

$$u_s = \sqrt{\frac{P - P_0}{\rho_0(1-\varepsilon)}} \tag{5.7}$$

$$u_p = \sqrt{\frac{(P - P_0)(1-\varepsilon)}{\rho_0}} \tag{5.8}$$

$$= u_s(1-\varepsilon) \tag{5.9}$$

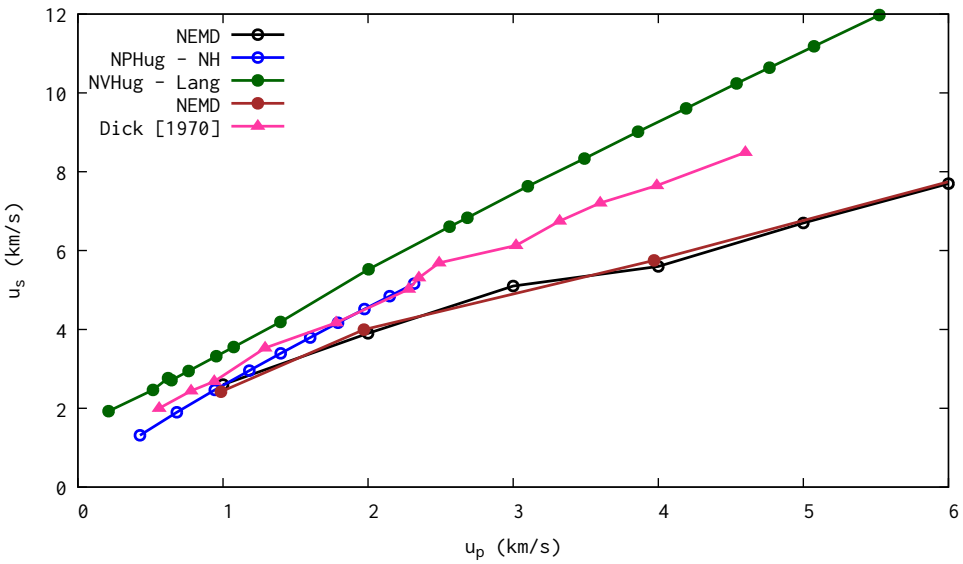

Figure 5.10: Shock-Particle velocity Hugoniot of Argon using various methods, theoretical data is using Lennard-Jones (6-12), CASTEP NEMD taken from Farrow and Probert [2011], experimental data taken from Dick *et al*. [1970].

As noted in (§1.4), the shock (u_s) and the particle (u_p) velocities are related by a linear dependence:

$$u_s = v_s + s\,u_p, \tag{5.10}$$

where v_s is the speed of sound, s is some constant which is material dependent.

Fitting a linear curve to the data in Fig. 5.10 we can obtain the material dependent s value and an estimate for v_s, which is essential for the fitting of the Mie-Grüneisen EoS (Table 5.2).

Source	s	v_s (km/s)
CASTEP NVHug	1.92 ± 0.01	1.55 ± 0.04
LAMMPS NEMD	0.83 ± 0.04	2.28 ± 0.25
LAMMPS NPHug	2.02 ± 0.02	0.53 ± 0.04
Farrow [2009]	1.02 ± 0.04	1.68 ± 0.20
Dick *et al*. [1970]	1.62 ± 0.04	1.29 ± 0.11
Moeller and Squire [1966]	—	1.26 – 1.35

Table 5.2: Calculated Hugoniot slopes and speed of sound and corresponding standard errors of the fit for Argon shocks calculated by different methods. Experimental data for the speed of sound in solid Argon is included from Moeller and Squire [1966].

As can be seen in Fig. 5.10, the NEMD calculations performed both in this work and in that of Farrow [2009] fail to accurately capture the shock speed as is measured experimentally. This could be due to the mass discreperancy between a real flyer-plate and the unrealistically high mass flyer-plate used in

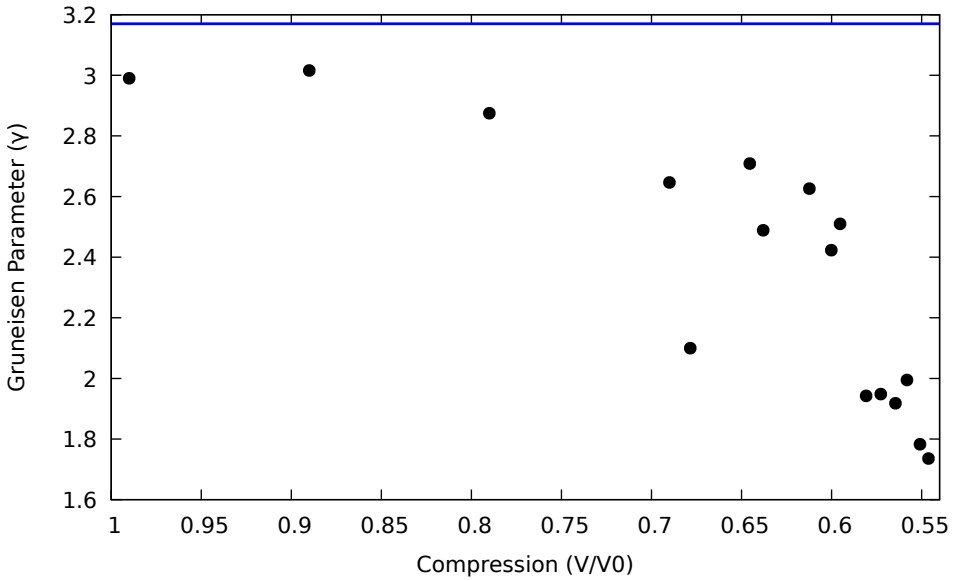

Figure 5.11: Calculated Grüneisen parameters for Lennard-Jones Argon under shock compression using a NVHug Langevin predictor scheme. The ideal crystal Grüneisen parameter is shown in blue.

the simulations (infinite in the LAMMPS NEMD calculations) causing a much harder shock than is physically reachable, despite the softer interaction than methods such as the momentum mirror. The inability to redistribute strain laterally due to the periodic boundaries may also be a key factor in this.

The Hugoniostat approaches, however, seem to capture the trends quite effectively, and both methods reproduce the slope of the curve to a reasonable degree, though both over-estimate the slope (Table 5.2).

5.2.4 Grüneisen parameter for Lennard-Jones Argon

Because of the pseudo-equilibrium nature of the NVHug method, and that after sufficient equilibration with the damped Langevin coupling it behaves like an NVT ensemble (Fig. 4.2), we can use the fluctuation formula defined in §2.5.9 to calculate the Grüneisen parameter for the shocked states of our system and calculate the change in the Grüneisen parameter with respect to the impact speed or maximum compression (Fig. 5.11).

The ideal Grüneisen parameter for zero-temperature, zero-pressure Lennard-Jones argon is 3.17 as shown in Krivtsov and Kuz'kin [2011]. Our estimates based on fluctuations in the molecular dynamics calculation will be subject to error due to finite run lengths, finite size systems, and possible correlation which we attempt to eliminate by spacing sampling. The approach does provide some insight into the trends which are present in the shocked medium

and is in agreement with the trends shown in experimental shocked materials such as HCP iron [Nie *et al.*, 2011].

The anomalous datum around 68% compression corresponds to the first backstep after the overstep and this may have arisen due to the lack of reuse of the previous cell (Alg. 2) and the associated increase in required convergence time. Looking at the graph of convergence, however, it seems sufficiently converged (Fig. 4.3). It may also, however, just be due to stochastic drift in the system temperature due to the Langevin thermostat.

5.3 *Ab Initio* Argon

The main focus of this project was to bring into the realms of feasibility the calculation of Hugoniots for any material without significant prior parametrisation. To this end it is essential that we are able to calculate the Hugoniot using *ab initio* methods. The many modifications we have made to the Hugoniostat method as outlined in earlier chapters (§4) have been with a focus on optimising the approach for DFT calculations in a static cell (NVHug) simulation.

The calculations were performed using CASTEP on 108 atoms of argon. This system is small, however, it is not beyond feasible tolerance according to Table 5.1. It is significantly smaller than the optimal size and was chosen purely as an example to show that this method works and can be applied to *ab initio* systems and converge in a reasonable time. Larger and more accurate simulations are certainly possible and would be favourable given a longer reasonable timespan in which to perform the calculations.

Due to prior failures caused by an error in the code, which is now fixed, a compromise between speed, and accuracy and stability had to be chosen in order to produce results. The cut-off energy was calculated to be 550 eV to give reasonable accuracy without damaging performance, the Brillouin-zone sampling was chosen to be 0.05Å^{-1} for the same reason.

Fig. 5.12 shows the Hugoniot extracted from the *ab initio* calculations of argon. The discrepancy between the *ab initio* and the LJ calculations are believed to be a combination of the finite-size effects due to the small scale of the system, which is in line with the error due to finite-size effects as found in Farrow and Probert [2011] and the fundamental differences between LJ and DFT argon. As Lennard-Jones is parametrised for stable argon we would expect deviations to occur as the system is put under extreme conditions in the Hugoniot due to electronic effects.

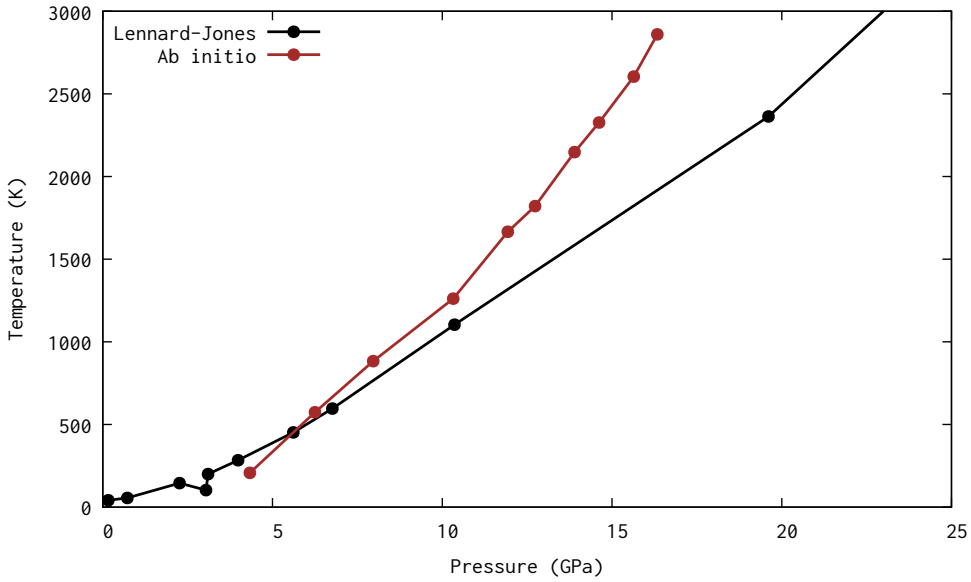

Figure 5.12: Pressure-Temperature Hugoniot plot comparing 864-atom Lennard-Jones perfect FCC cell and 108-atom *ab initio* argon perfect FCC cell using Langevin NPHug

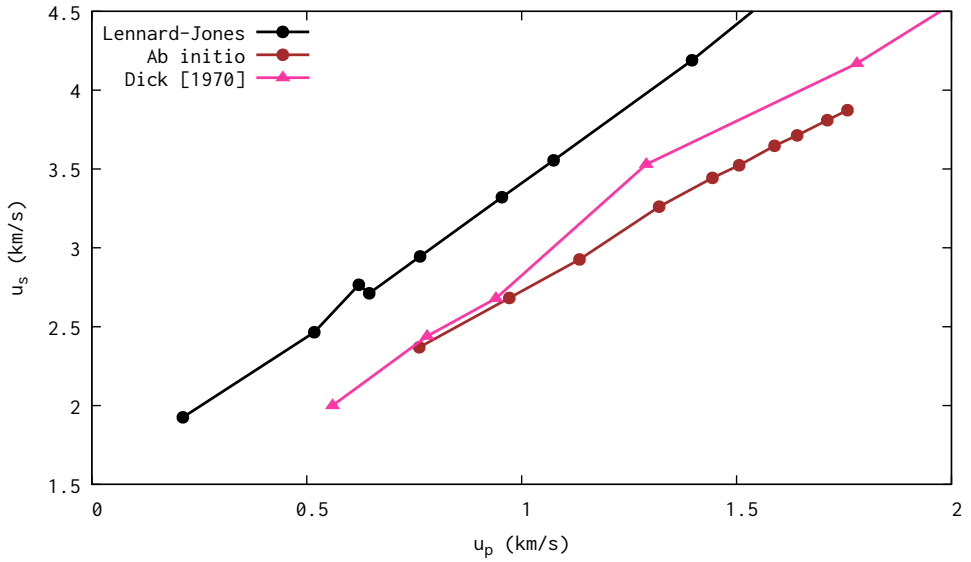

Figure 5.13: Shock-Particle velocity Hugoniot of argon comparing 864-atom Lennard-Jones perfect FCC cell and 108-atom *ab initio* argon perfect FCC cell using Langevin NPHug, experimental data taken from Dick *et al*. [1970].

Fig. 5.13 shows the corresponding u_s-u_p curve for the LJ and *ab initio* data. The *ab initio* data aligns surprisingly well with the experimental data of Dick *et al*. [1970] which may be due to its better representation of the pressure effects outside of equilibrium. In addition to this, as can be seen in Table 5.3, the agreement with experimental data is better than the best of the Lennard-Jones systems, even with the apparently erroneous finite-size effects.

Source	s	v_s (km/s)
Lennard-Jones	1.92 ± 0.01	1.55 ± 0.04
Ab Initio	1.53 ± 0.02	1.21 ± 0.03
Dick *et al*. [1970]	1.62 ± 0.04	1.29 ± 0.11
Moeller and Squire [1966]	—	1.26 – 1.35

Table 5.3: Calculated Hugoniot slopes and speed of sound and corresponding standard errors of the fit for Argon shocks calculated by different methods. Experimental data for the speed of sound in solid Argon is included from Moeller and Squire [1966].

Chapter 6

Quartz Simulations

In this section we will explore the the different methods of generating shock-waves by applying them to a more complex system. The system of choice as mentioned previously is that of quartz silicates, starting from the α-quartz phase. The results were generated using the short-range modified BKS potential as discussed in (§3.1) in both LAMMPS [Plimpton, 1995] and CASTEP [Clark *et al.*, 2005].

The reasons for this choice are manifold, it is anisotropic material, with multiple elements, but with a well defined and explored set of empirical potentials and with a large set of experimental and theoretical data. It is also an abundant material and its high-pressure phases are of interest to a number of fields.

The potential used in LAMMPS is the same as that of CASTEP. It is generated from an interpolation table generated from the CASTEP pair-potential output, with an overlaid long-ranged Coulomb interaction.

6.1 BKS Simulations

6.1.1 NEMD

NEMD Simulations were performed in LAMMPS [Plimpton, 1995], again using a modified script based on that of Guerrero-Miramontes. With an infinitely massive flyer-plate interacting using the re-fitted modified BKS potential [van Beest *et al.*, 1990] with the short range modification and parameters as given in Table 3.3.

The key difference between the α-quartz NEMD simulations and those of the Lennard-Jones argon is that due to the long-range potential in the Coulomb part of the calculation (performed using Ewald summation), it is necessary

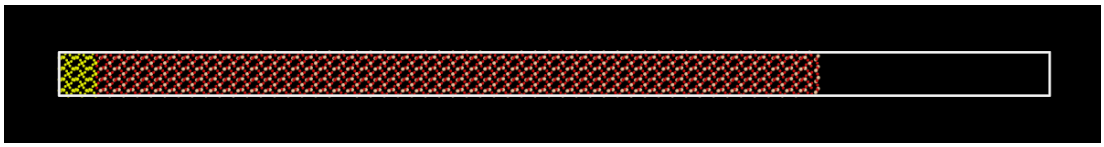

Figure 6.1: The initial system set-up for the LAMMPS NEMD BKS shock. The flyer-plate is in yellow and launched with its initial velocity and feels no response force. Note the addition of a vacuum gap compared to Lennard-Jones simulations to reduce interaction along the direction of the shock.

to make several adjustments. For example, we cannot have the open-face boundary conditions in the Z-axis which were permissible in the Lennard-Jones simulations, and so fixed boundaries are used. We must also create a slab-geometry for our system (Fig. 6.1), as the Coulomb term would interact across the periodic images of our structure. Due to the polar nature of α-quartz we also need to take account of the long-range dipole interaction in the NEMD simulations. The cleave planes at the surface of the silica slab leave exposed faces of oxygen or silicon (Fig. 6.2), which due to long-range Coulomb interactions cause a potential difference between the two faces of the slab. To account for this we apply the correction of Yeh and Berkowitz [1999], which is available in the LAMMPS code.

Before the start of the calculation, the system is once again allowed to relaxed in the bulk state to optimise the crystal structure. The cell is then extended, creating the slab separation and the system is allowed to relax under NVE for a period of time (1ps) to account for any required surface reconstruction of the cleaved faces.

Because of the stiffer material and its higher speed of sound, at lower piston speeds the wave disperses and loses its discontinuity (Fig. 6.3), this is due to these impacts being sub-sonic and thus not shocks.

The NEMD simulations of the BKS quartz are in strong agreement with the experimental and Hugoniostat results in the u_s-u_p space (Fig. 6.5), but disagree strongly with those of Farrow [2009]. This is probably due to the difference in potentials (§3.1).

The upper graph in Fig. 6.3 shows some dispersion of the shock front. This may be due to a sub-sonic impact and a dissipation of the shock-wave. It may also be that the system is showing a finite ramping of the particle velocities due to the finite strain rate of low-velocity impacts [Swegle and Grady, 1985].

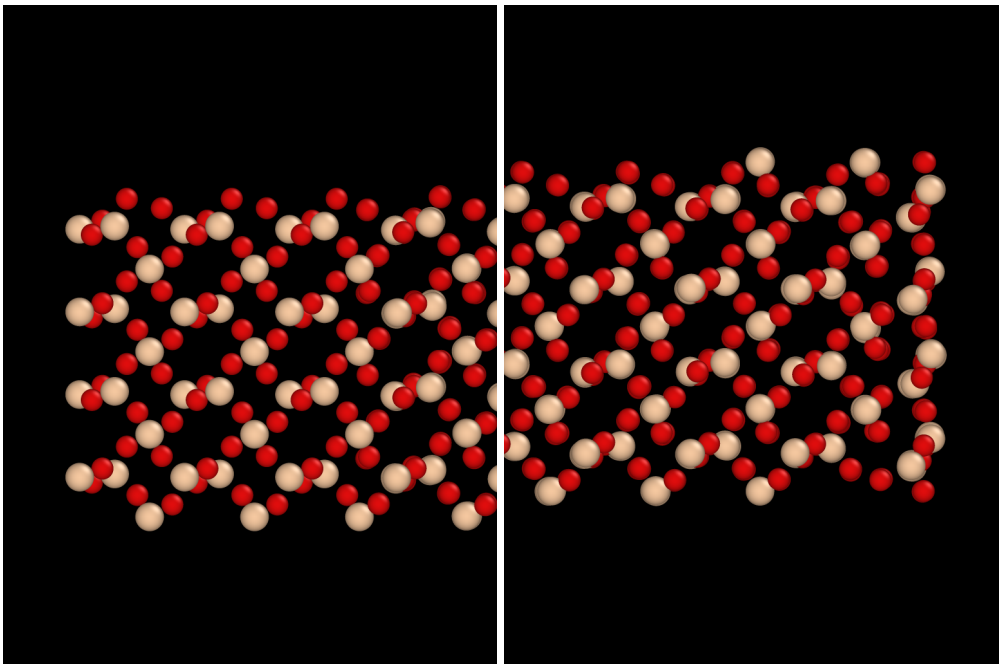

Figure 6.2: (Left: Piston end, Right: Open top surface after reconstruction) The exposed, charged face of the silicon interacts through through the long-ranged Coulomb potential to create a potential difference along the long axis of the cell.

6.1.2 Hugoniostat

6.1.2.1 Issues with the Constant-Volume Hugoniostat

The accelerated equilibration approaches used in the CASTEP NVHug approach are not without some drawbacks. Initial attempts at simulating α-quartz with a uniaxial compression resulted in a divergence in the target temperature to negative values. This is obviously unphysical.

It is believed that the origin of this issue is that the structure of α-quartz, when compressed along the perpendicular axis (which we call Z), disperses the pressure laterally along the X & Y axes. This leads to a drop in the measured pressure in the direction of compression. Recalling that in the uniaxial Hugoniot-Rankine EoS:

$$E_H = E_0 - \frac{1}{2}(P_{zz} + P_0)(V - V_0)\,, \tag{6.1}$$

the only contributing stress component is that of the direction of compression.

As such the compression for the NVHug CASTEP calculations was performed isotropically by applying:

$$\underline{\underline{\mathbf{h}}}_{comp} = \varepsilon \underline{\underline{\mathbf{I}}} \cdot \underline{\underline{\mathbf{h}}}_0, \tag{6.2}$$

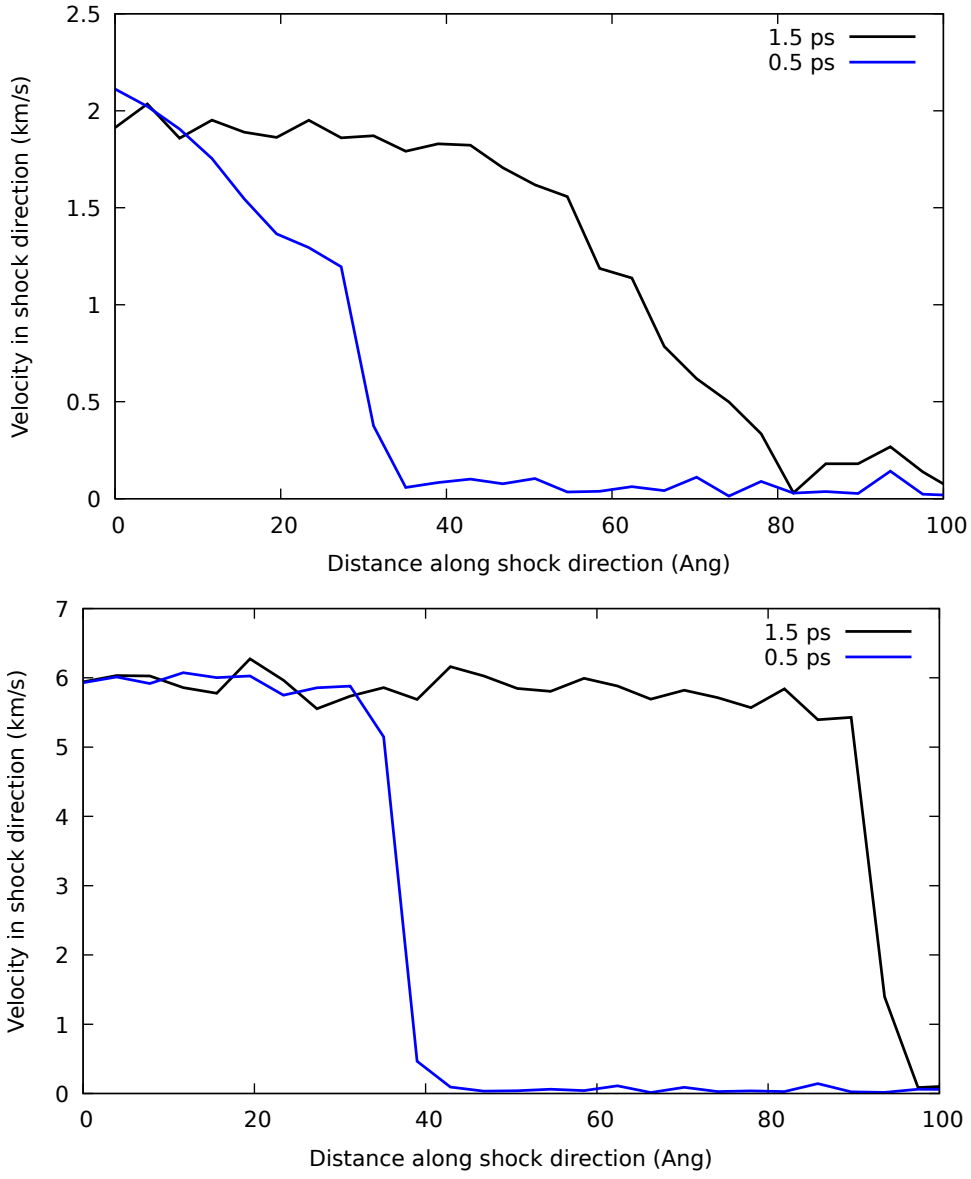

Figure 6.3: Velocity profile of two different impact speeds (Top: 2km/s, Bottom: 6km/s) showing the dispersion of the shock at low impact velocities.

and the Hugoniot-Rankine equation is replaced with:

$$E_H = E_0 - \frac{1}{2}\left(\tfrac{1}{3}\mathbf{Tr}(\underline{\underline{\mathbf{P}}}) + P_0\right)(V - V_0)\,, \tag{6.3}$$

It may be possible using the Poisson ratio [Sokolnikoff, 1956] of a material to estimate how the pressure will be distributed in a material. Since this requires foreknowledge of the material system in question, we do not currently see this as a complete solution to our issues as it may also vary depending on compression phenomena and phase transitions in the material make it costly to calculate.

6.1.2.2 Results

The LAMMPS calculations in this section were performed using a 576-atom α-quartz cell and the uniaxial (along the C-axis) constant-pressure Nosé-Hoover Hugoniostat from 10–100GPa in steps of 10GPa, but with extra measurements taken at 15GPa and 18GPa to attempt to capture the collapse of the α-quartz structure.

The CASTEP calculations were performed using 72- or 576-atom α-quartz cell and the isotropic constant-volume Langevin Hugoniostat predictor from 20–200GPa in steps of 20GPa.

Both the LAMMPS and CASTEP Hugoniostat calculations for BKS quartz show a strong reproduction of the trends displayed in the results obtained by Marsh [1980] and Wackerle [1962] for α-quartz shocks in the higher pressure regions, though at lower pressures there is some discrepancy in the LAMMPS data (Fig. 6.4). This could be explained by an early phase transition in the BKS potential [Saika-Voivod *et al.*, 2004] or due to the anisotropy of the quartz crystal, by the crystal direction in which the shocks are occurring.

The CASTEP Hugoniot follows the lower compression trends much more closely, though there is a significant drop in measured pressure around a compression of 0.63, which could be due to a phase transition in the material or a secondary collapse of the α-quartz structure.

Both Hugoniostat methods agree extremely well with experiment for the u_s-u_p Hugoinot (Fig. 6.5). The large disagreement between the results of Farrow [2009] probably comes from the discontinuities in the potential used, as demonstrated by the NEMD results obtained using the corrected potential in LAMMPS.

The discontinuity in the Hugoniot around 10–20 GPa is likely due to a tran-

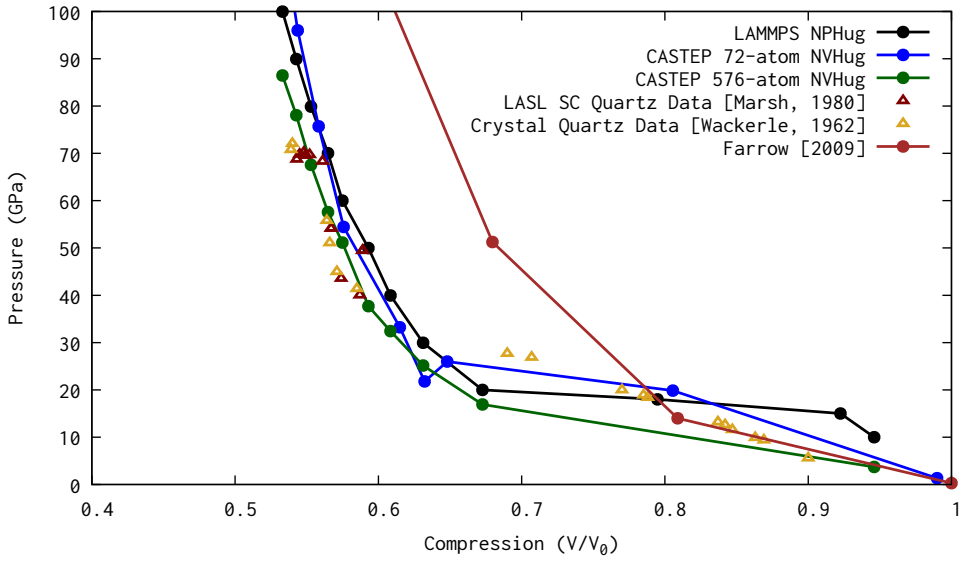

Figure 6.4: Compression-Pressure Hugoniot for BKS α-quartz with experimental data taken from Marsh [1980] and Wackerle [1962] and theoretical data from Farrow [2009].

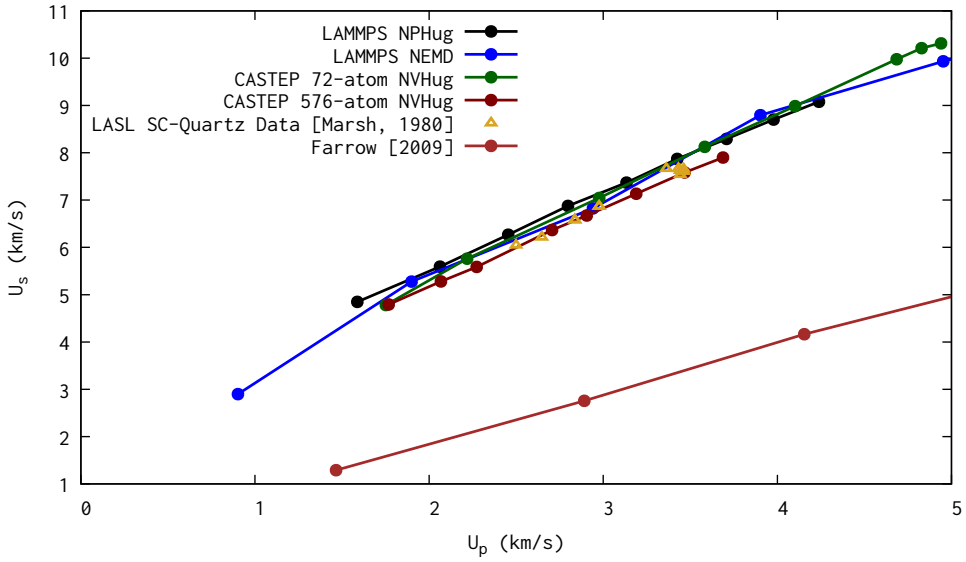

Figure 6.5: Shock-Particle velocity Hugoniot for BKS α-quartz with experimental data taken from Marsh [1980] and theoretical data from Farrow [2009].

Source	s	v_s (km/s)
CASTEP NVHug	1.73 ± 0.02	1.84 ± 0.09
LAMMPS NPHug	1.60 ± 0.02	2.34 ± 0.07
LAMMPS NEMD	1.74 ± 0.12	1.66 ± 0.39
Marsh [1980]	1.72 ± 0.06	1.72 ± 0.19
Farrow [2009]	0.94 ± 0.02	0.27 ± 0.06

Table 6.1: Calculated Hugoniot slopes and speed of sound and corresponding standard errors of the fit for BKS shocks calculated by different methods. Experimental data is included from Marsh [1980].

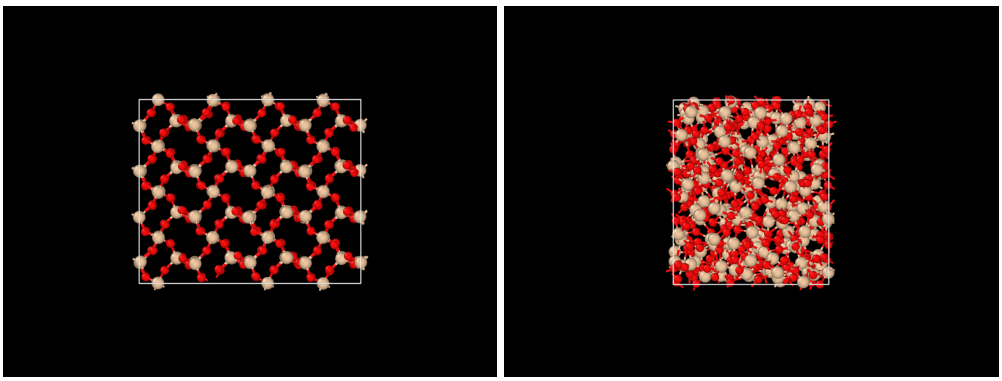

Figure 6.6: Structure of post-shock BKS silica after LAMMPS NPHug calculations for 10GPa (Left) and 20GPa (Right) showing the collapse of the ordered α-quartz structure and the origin of the discontinuity in volume between the 10 and 20GPa measures in the LAMMPS data of Fig. 6.4.

sition to a phase transition between the α-quartz phase and the stishovite phase, resulting in a volume drop. The ratio of volumes per atom between α-quartz and stishovite for the BKS potential is $1:0.596$. The collapse seen in the LAMMPS calculation is ~ 0.72, this discreperancy can be accounted for by noting that in Fig. 6.6 the collapsed phase is not pure Stishovite, but a very dense disordered phase.

6.1.2.3 Grüneisen parameter of BKS Quartz

Applying the methods described in §2.5.9, we can determine the Grüneisen parameter for BKS quartz from our CASTEP NVHug simulations.

Unfortunately, our measurements for the Grüneisen parameter (Fig. 6.7) does not seem in alignment with the experimental data [Knudson and Desjarlais, 2013]. This may be due to the perfect nature of the crystal, limitations in the potential or due to the approximations made in calculating the fluctuation formula.

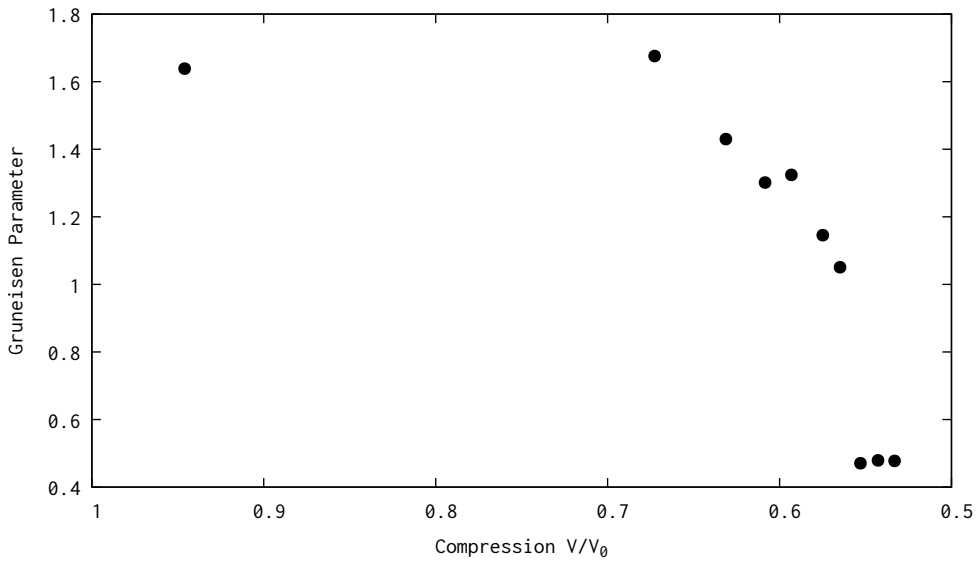

Figure 6.7: Graph of calculated Grüneisen parameters for α-quartz from 576-atom CASTEP NVHug simulations .

6.1.2.4 Structural Analysis of discontinuity in the LAMMPS NPHug Hugoniot

Visual analysis of the structure of the 10GPa compressed crystal (Fig. 6.6) suggests the medium is still in the α-quartz phase.

Coordination analysis, however, appears to show that the state is half-way towards the β-quartz phase and is not a pure α-quartz phase (Fig. 6.11). This could be due to thermal smearing, to which the Voronoi coordination can be somewhat sensitive. The method used specifies that, for a face to be counted in the coordination analysis, its surface must make up at least 1.5% of the total Voronoi polyhedron's area in an effort to eliminate these "noisy faces".

Centrosymmetry analysis, tells the original story and suggests that the 10GPa phase is likely still in an α-quartz phase with some distortion (Fig. 6.9), which is in line with the visual inspection.

RDF analysis of the structure agrees that the structure is in a distorted α-quartz phase (Fig. 6.10).

Neither bond-angle analysis nor common neighbour analysis are able to identify the structure as it does not align with any of the predefined structural types.

None of our analysis techniques have revealed any key identifiable features of the structure of the 20GPa compressed phase, suggesting that it is some sort of amorphous phase, especially given that the structure appears to have lost its long-range order (Fig. 6.10), though the atomic volumes of the 20GPa phase

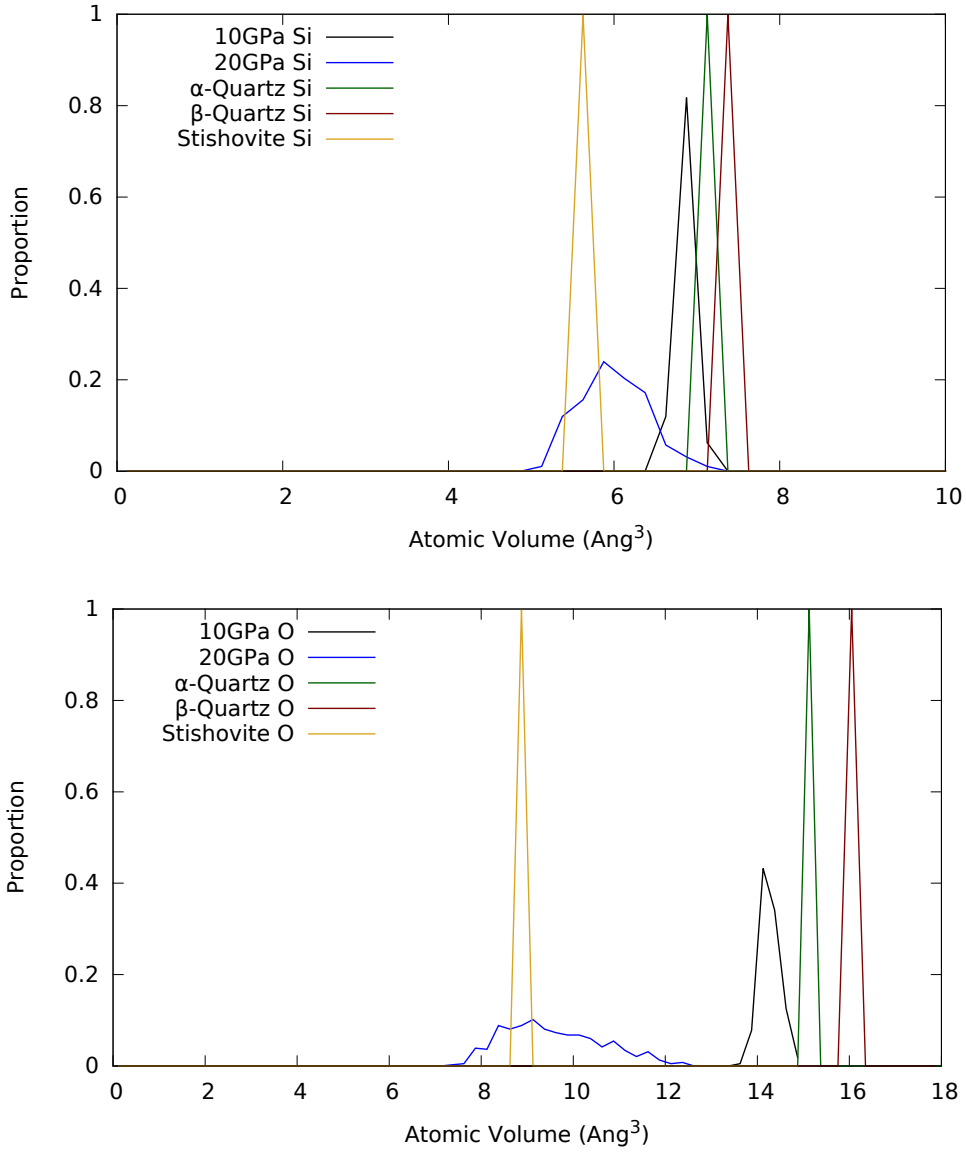

Figure 6.8: Species separated Voronoi polyhedron volume with minimum face threshold of 1.5% of the structures in Fig. 6.6 compared with ideal crystals.

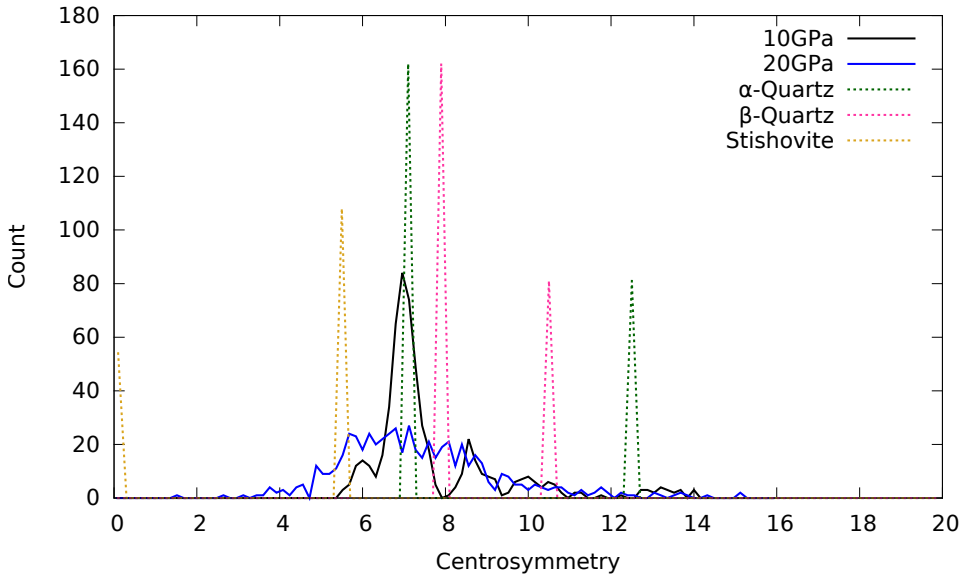

Figure 6.9: Centrosymmetry analysis with 12 neighbour basis (based on Fig. 6.11) of the structures in Fig. 6.6 compared with ideal crystals.

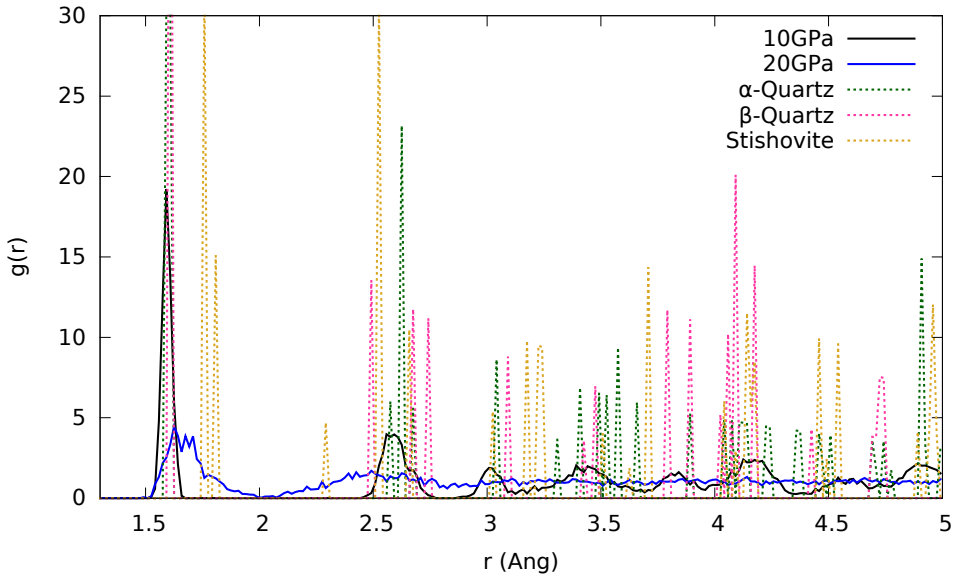

Figure 6.10: RDF analysis of the structures in Fig. 6.6 compared with ideal crystals.

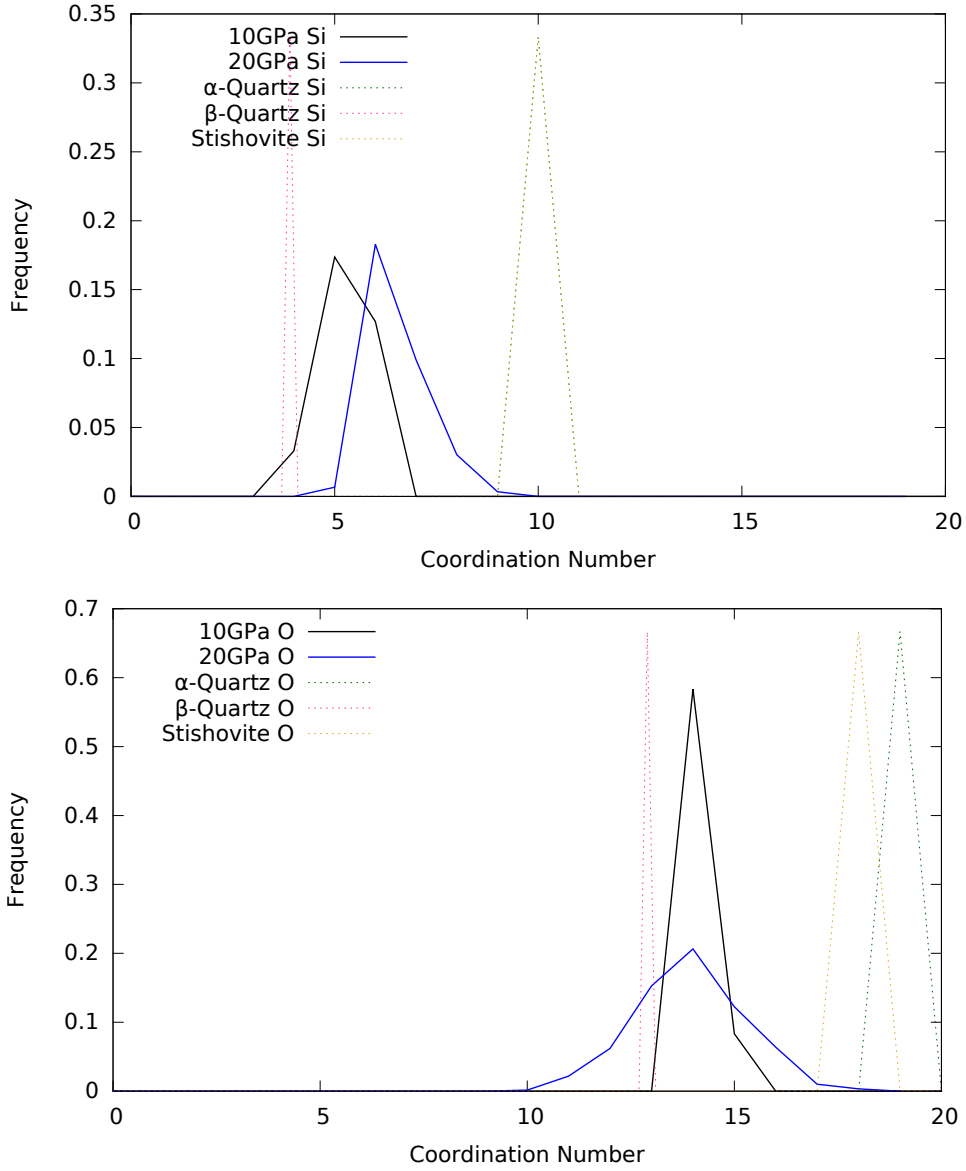

Figure 6.11: Species separated Voronoi coordination analysis with minimum face threshold of 1.5% of the structures in Fig. 6.6 compared with ideal crystals. Frequency is as a proportion of the whole cell. α-Quartz and β-quartz coordinations of silicon are both 10-fold

correspond much more closely with those of Stishovite than the other phases (Fig. 6.8) and at a volume per atom in the order of 9.5Å^3 should find stishovite a more stable phase at ambient temperatures (Fig. 3.3).

6.1.2.5 Post-Minimisation Shocked Structure

Taking the 20GPa shocked structure, and using a Parrinello-Rahman NPT Langevin calculation at 400K and zero external pressure for 500ps and then performing a FIRE minimisation, we attempt to find a relaxed structure. The realised minimum structure is shown in Fig. 6.12.

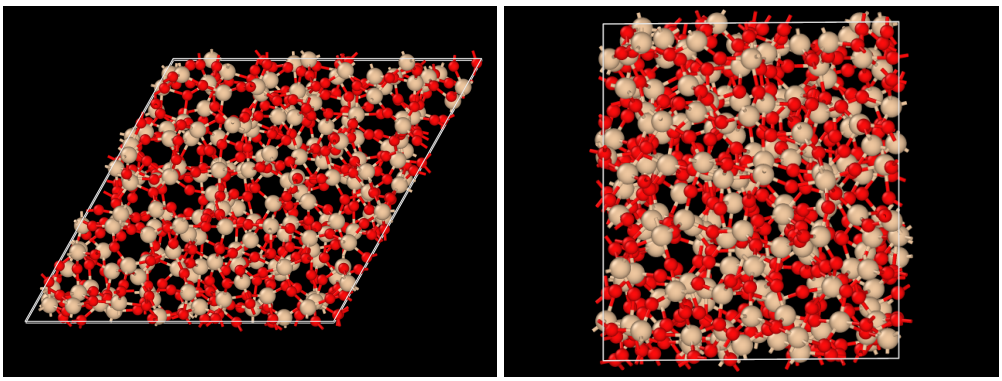

Figure 6.12: Structure of post-shock BKS silica after minimisation according to the precedure laid out in the text.

We do not cool the material down from the 400K peak as any cooling rates in the course of the simulation would not be physically realisable and would instantaneously quench the medium into a glassy phase.

The choice of 400K as the temperature for the equilibriation is that this is around the final Hugoniostat temperature calculated in the NPHug simulation, and as such is assumed to be the temperature from which the shocked material would cool.

The reason for the Langevin calculation is that its symplectic nature guarantees that any energy barriers in minimising the structure can eventually be overcome.

Though this structure still shows a great deal of disorder it still favours staying in the compressed state and, though the cell does expand, does not relax into a much more voluminous state (Fig. 6.13 and Fig. 6.14). This is in agreement with the energy-volume curve for BKS (Fig. 3.3).

The results of the local- and global-structure analyses, it is clear that the minimised structure is still a glassy phase, without long-range order (Fig. 6.15)

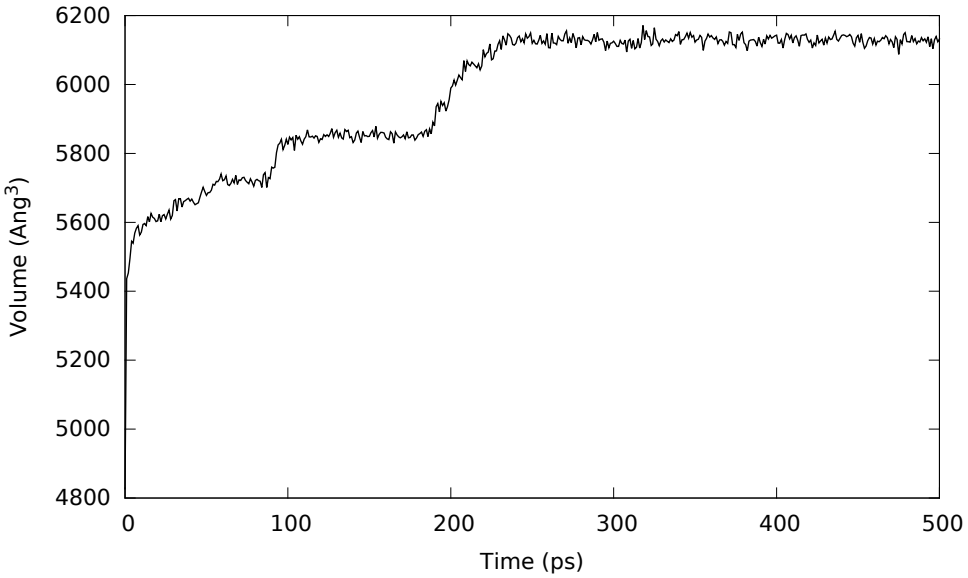

Figure 6.13: Plot of Volume fluctuation in the NPT minimisation of the 20GPa shocked structure. Sampled every picosecond.

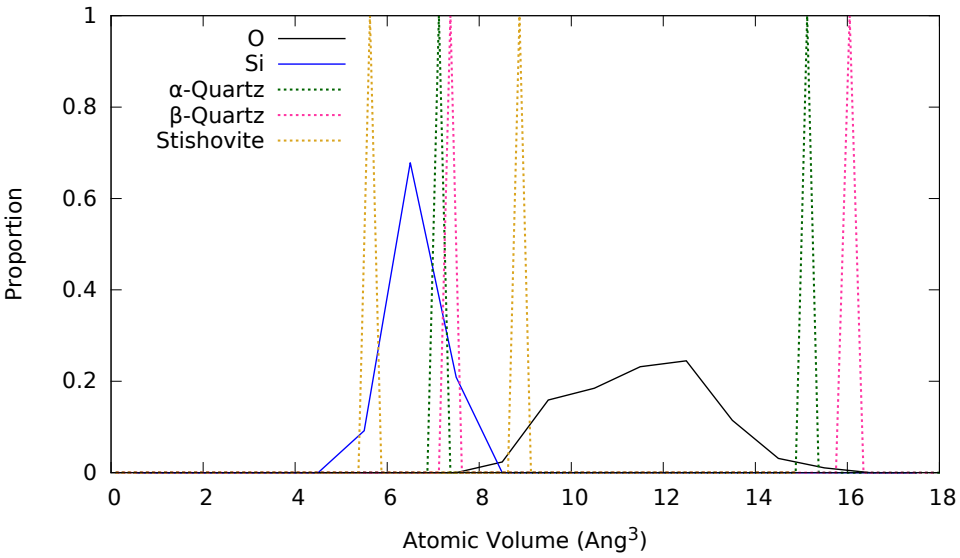

Figure 6.14: Voronoi polyhedron volume with minimum face threshold of 1.5% of the minimised 20GPa shocked structure compared with ideal crystals.

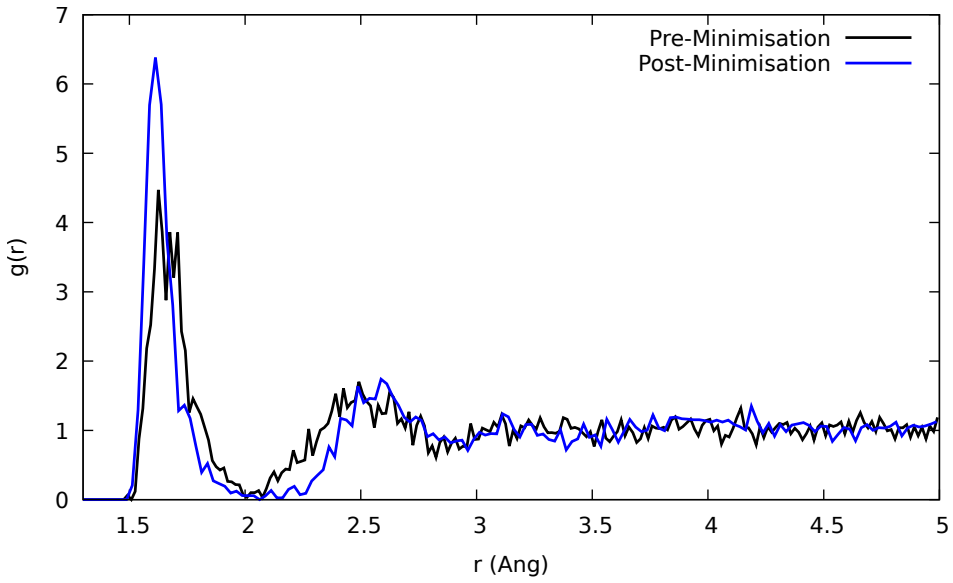

Figure 6.15: RDF of the pre- and post-minimisation structures of the 20GPa shocked structure. Note that though there has been sharpening of the first and second neighbour peaks, there is still a distinct lack of long-range order.

and does not conform to any of the usual quartz structures (Fig. 6.16).

Examining the Molecular Dynamics trajectory more closely reveals that the volume relaxation goes in stages rather than a continuous expansion, and that after 200ps, the volume of the cell appears to not change (Fig. 6.13). The MSD (Fig. 6.17) indicates that the relaxation also goes in stages as perhaps a major slippage occurs, however, this does not necessarily correlate temporally with a volume change in the cell. This might indicate that a longer run could result in slippage into an ordered phase.

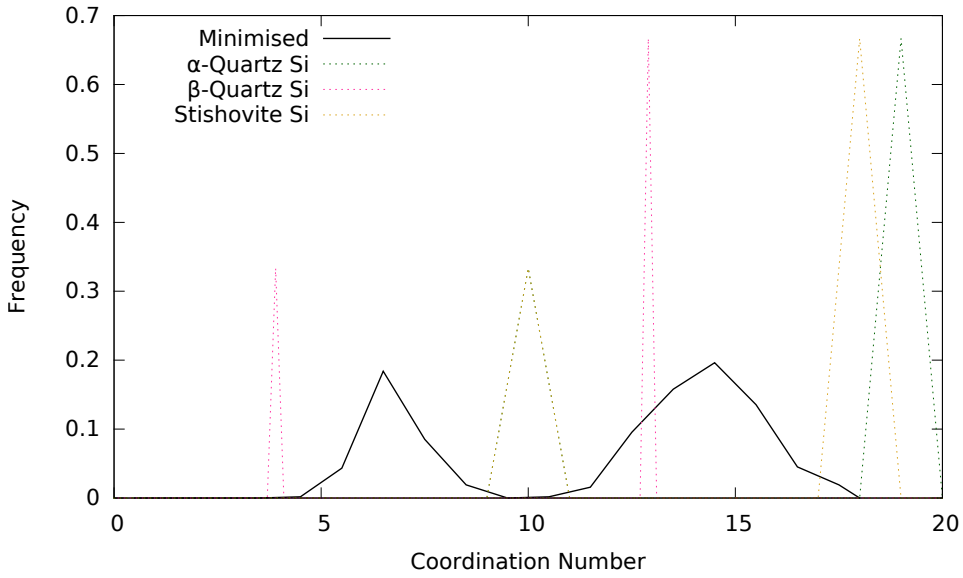

Figure 6.16: Voronoi coordination analysis with minimum face threshold of 1.5% of the minimised 20GPa shocked structure compared with ideal crystals.

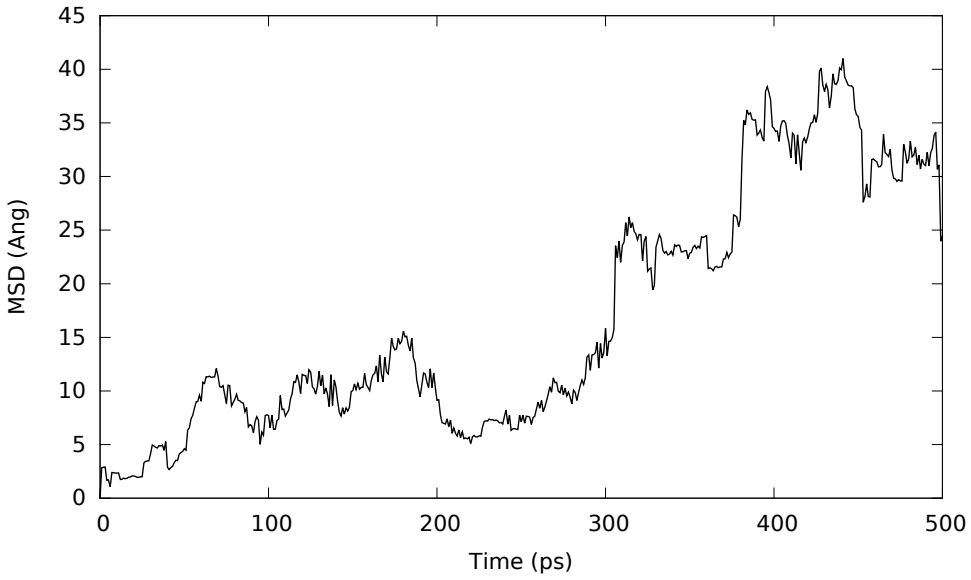

Figure 6.17: Mean-Square-Displacement of the NPT calculation of the 20GPa shocked structure. Sampled every picosecond.

Chapter 7

Conclusions

Atomistic simulations of shock-waves open a new world of information to a broad range of fields and may be useful in predicting mechanisms of structural collapse in materials and material resistances to shocks and strains in general.

The ability for a non-expert to perform *ab initio* shock calculations simply will hopefully spread the use of these more accurate and adaptable techniques in the field of extreme rates. The capacity for doing large-scale databasing of materials properties for different applications could help locate potentially useful building materials. It may also help geoscientists to understand the mechanisms behind the formation of new mineral structures along fault-lines and astronomical impact sites, terrestrial and otherwise.

The improvements made to convergence rates with the new Langevin integrator and the lack of dependence on couplings, mean that these calculations are now made easier than ever to perform accurately and should be feasible for anyone with a reasonable understanding of *ab initio* simulation. The advantages given by an independence from requiring accurate couplings for convergence is that the recommended estimates for optimal coupling given in Ravelo *et al*. [2004] are expensive to calculate, especially in an *ab initio* calculation. Not only that, but they should be updated for different compressions to achieve rapid equilibration, this becomes prohibitive *ab initio*.

The usefulness of local-structure analysis techniques in shocked systems is limited when the system falls into a glassy disordered phase, again, possibly due to the scale of the simulations. Should it, however, become possible in future to perform realistic shock unloading simulations, local-structure analysis will no doubt prove invaluable in detecting the polycrystalline structures formed from the relaxation.

Even without simulating the entire Hugoniot the Hugoniostat may prove use-

ful in generating high-pressure physically relevant structures for the purposes of exploring electronic or phononic properties using *ab initio* approaches such as birefringence to explain experimental findings such as Tear *et al*. [2014]. It may even be possible to generate these feasible systems using the Hugoniostat with an empirical potential and then apply *ab initio* analysis on the resulting structures.

7.1 Quartz

In our attempts to analyse the resultant systems produced by shocking quartz structures, we do not find a transition between crystalline phases in the shocked state. Instead we find that the structure collapses upon reaching a certain stress, forms an amorphous structure and remains in this collapsed phase.

This could be due to the small number of atoms (and hence degrees of freedom) in the calculations performed. Scaling limitations of the *ab initio* calculations and, because it is not a dedicated empirical potential code for CASTEP's pair-potentials as well, limit our ability to perform much larger calculations without considerable computational expense.

This does, however, mean that the results obtained by the *ab initio* are more directly comparable with results from the empirical potential and we have shown that the results with even small simulation cells reproduce the experimental properties reliably.

Attempts to relax this phase back into a stable quartz-like crystal structure failed and the structure was fixed into a glassy phase. It is possible that with sufficient heating the system would relax back into a quartz structure, however, it is known that glassy phases of quartz are quite stable, given that it is the glassy silicate phases which are commonly called "glass".

7.2 Hugoniostat

We find that our implementation of the Hugoniostat is in agreement with that of the reference implementation of the Hugoniostat in the LAMMPS code. We also find that our extensions to the Hugoniostat have significantly improved the equilibration times compared to those of LAMMPS without detracting from its accuracy.

The static compression of the constant-volume Hugoniostat is much more amenable to *ab initio* simulations as its consistent cell lengths mean that the *ab initio* cal-

culations can be accelerated and do not have to recalculate a lot of properties which depend upon the simulation cell. As the cell properties are known from the start of the calculation it is also possible to account for the compression in the convergence of systematic parameters.

The ability to generate a Hugoniot automatically from a starting state for any material, in principle, gives great power to those who wish to be able to "black box" *ab initio* simulation and opens a new, wide range of properties to materials databasing projects. Given how important shock resilience is to a large number of engineering and geophysical sciences, this will doubtless prove essential in the future.

Although our *ab initio* simulations are certainly not conclusive, having an exploratory probe showing that their calculation is possible is still a major step in the right direction, and hopefully with the dedication of more resources and time to the problem, a more detailed exploration of new materials can be opened to research.

7.3 Farrow and Probert

We have identified several inconsistencies between this work and that of Farrow [2009].

Though they found that the ground state for the BKS potential to be in the β-quartz phase, we find that the BKS potential follows the experimental phase diagram and has its ground state in the α-quartz phase and transitions to the β-quartz phase under thermal excitation, which is in agreement with other implementations of BKS [Cowen and El-Genk, 2015].

We also found that the curves fitted to the point of inflexion of the BKS potential were mislocated, suggesting that the implementation of their potential may differ from that in this work. These have been refitted and now align with the potential output from the CASTEP pair-potential plotting routines.

These may be the root cause or key factors contributing to the major discrepancy between the experimental data and the results of the calculations they performed.

7.4 Future Work

7.4.1 Further post-shock analysis

It should be possible using the systems produced by the Hugoniostat method to calculate a variety of electronic properties in the materials of interest in the shocked state. Such calculations, such as electrical conductivity calculations, could improve experimental measurements which rely on material properties such as impedance. It should also, as suggested previously, be possible to calculate optical properties of the shocked state, such as birefringence [Tear *et al.*, 2014].

In this work we have already shown the capability of calculating system properties such as the Grüneisen parameter as thermodynamic averages in the shocked state, which can be essential in calculating the equations of state for shocks [Mie, 1903].

7.4.2 Extended Automation in the Predictor

Ideally, the Hugoniostat predictor method would be able to automatically recompute properties such as k-point grids for the compressed cells as the calculation continues, allowing faster calculations at lower compression (larger cells), where fewer k-points are needed, while still maintaining the accuracy of the converged k-point spacing. This benefit would only be possible in the constant-volume Hugoniostat formulation.

It could also be possible to perform some sort of wave-function extrapolation and speed up the calculation of the first step after a compression rather than starting afresh with a wave-function for a system which bears little resemblance to the new one. This extrapolation could purely be a compression of the wave-function for the uncompressed cell, which undoubtedly be a better match for the system than the last state of the previous shocked system.

As mentioned in (§4.2.2.4) it would also be possible to derive an approximation for the coupling of the Langevin or Nosé-Hoover-Langevin formulations of the predictor. This could accelerate the convergence of these calculations further. Ideally, it would also be possible to derive a critical damping from the predictor for the coupling in all of the integrator schemes, such that the calculation can converge as quickly as possible.

Using predictions based on the compression-temperature relationship, it should be possible to estimate the next system temperature and thus estimate the

likely maximum velocity. Using predictions of speed of sound in the medium as a point of reference, it should be possible to calculate whether the current time-step is viable and also an optimal coupling for the thermostat to the system, not just the Hugoniostat to the thermostat.

7.4.3 Shock Unloading

The process of shock unloading would be an interesting place to explore further, though the attempts made in this work to relax the material from its collapsed shock state into a crystalline phase failed, it may be possible to calculate a better approach by which to release the shock by causing processes like rarefaction to occur in the material.

The rarefaction process would require an estimate for the negative pressure applied to the system as the material relaxed, which could prove an area which has not been well explored, though there are numerical studies in the field [Popov, 2007].

Appendix A

Nosé Hamiltonian

The Nosé Hamiltonian [Nosé, 1984] is the basis of the Nosé-Hoover-like systems of equations and is generated from an extension of the classical Hamiltonian (Eq. A.1) with a heat bath. It should be noted that, although the Nosé-Hoover equations are derived from a transformation of the Nosé Hamiltonian, they are in fact describing a non-Hamiltonian system.

$$\mathscr{H}_C = \sum_{i=1}^{N} \frac{\mathbf{p}_i^2}{2m_i} + U(\mathbf{r}_i, \ldots, \mathbf{r}_N) \tag{A.1}$$

$$\mathscr{H}_N = \sum_{i=1}^{N} \frac{\mathbf{p}_i^2}{2m_i s^2} + U(\mathbf{r}_i, \ldots, \mathbf{r}_N) + \frac{p_s^2}{2Q} + g k_B T \ln(s) \tag{A.2}$$

Where $\mathbf{p}$ is the momentum, m is the mass, r is the position, U is the potential energy, s is the "position" of the heat bath, p_s is the "momentum" of the heat bath, Q is the "mass" of the heat bath, k_B is the Boltzmann constant, T is the target temperature, properties of particle i are indicated by a subscript, g is the number of degrees of freedom.

Appendix B

Andersen Hamiltonian

The Andersen Hamiltonian [Andersen, 1980] for pressure regulation is based on a transformation of the classical positions and momenta such that they have an explicit dependence on the volume of the cell which is being modified.

$$\mathbf{s}_i = V^{-\frac{1}{3}}\mathbf{r}_i \tag{B.1}$$

$$\pi_i = V^{\frac{1}{3}}\mathbf{p}_i \tag{B.2}$$

where V is the volume of the cell.

$$\mathscr{H}_A = \sum_{i=1}^{N} \frac{V^{-\frac{2}{3}}\pi_i^2}{2m_i} + U\left(V^{\frac{1}{3}}\mathbf{s}_i, \ldots, V^{\frac{1}{3}}\mathbf{s}_N\right) + \frac{p_V^2}{2W} + PV \tag{B.3}$$

where U is the potential, p_V is the piston velocity, P is the instantaneous pressure, W is the pressure coupling which is determined as:

$$W = (3N+1)\,k_B T\,\tau_b^2, \tag{B.4}$$

where τ_b is a time scale for the pressure regulation, $3N+1$ is due to the number of degrees of freedom in the system (i.e. $3N$ particle and one volume)

By Hamilton's equations we find:

$$\frac{\partial \mathbf{s}_i}{\partial t} = \frac{\partial \mathscr{H}_A}{\partial \pi_i} = \frac{V^{\frac{2}{3}}}{\pi_i^2 m_i} \tag{B.5}$$

$$\frac{\partial \pi_i}{\partial t} = -\frac{\partial \mathscr{H}_A}{\partial \mathbf{s}_i} = -\frac{\partial U}{\partial\left(V^{\frac{1}{3}}\mathbf{s}_i\right)} V^{\frac{1}{3}} \tag{B.6}$$

$$\frac{\partial V}{\partial t} = \frac{\partial \mathscr{H}_A}{\partial p_V} = \frac{p_V}{W} \tag{B.7}$$

$$\frac{\partial p_V}{\partial t} = -\frac{\partial \mathscr{H}_A}{\partial V} = \frac{1}{3} V^{-\frac{1}{3}} \left(\sum_{i=1}^{N} \frac{V^{-\frac{4}{3}} \pi_i^2}{m_i} - \frac{\partial U}{\partial\left(V^{-\frac{2}{3}}\mathbf{s}_i\right)} \cdot \mathbf{s}_i \right) - P \tag{B.8}$$

Appendix C

Work Undertaken Outside the Scope of the Main Project

C.1 Ergodic Integrators

In the software package CASTEP [Clark *et al.*, 2005] it was found that the integrators for Nosé-Hoover-like (NHC, NHL) schemes were not ergodic for the case of the simple harmonic oscillator.

It was discovered that the integrators as described in Martyna *et al.* [1992] required an implicit integration step within the update called a Suzuki-Yoshida integration. This arises due to the fact that for a non-Hamiltonian system, we need to consider the lack of a definition of what symplecticity means or how it can be measured [Ezra, 2006]. Therefore Tuckerman [2010] describes how to construct a measure-conserving integrator through the Liouvillian formulation.

If the propagator through phase space is given by

$$\dot{\mathbf{x}} = \xi(\mathbf{x}) \text{ ,which is equivalent to,} \tag{C.1}$$

$$\dot{\mathbf{x}} = i\mathscr{L}\mathbf{x}, \tag{C.2}$$

where

$$i\mathscr{L} = \xi(\mathbf{x}) \cdot \nabla_x. \tag{C.3}$$

Then, using equations 2.52 to 2.57 we find the corresponding Liouville operator to be:

$$i\mathscr{L} = i\mathscr{L}_{NHC} + i\mathscr{L}_p + i\mathscr{L}_r, \tag{C.4}$$

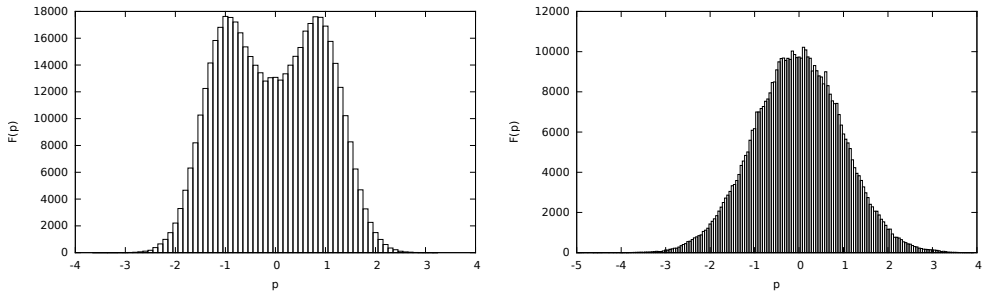

Figure C.1: Histogram of velocities for a simple harmonic oscillator before (left) and after (right) the modifications which introduced the Suzuki-Yoshida integration scheme. The correct distribution of the velocities should be a Gaussian [Tuckerman, 2010].

where

$$i\mathscr{L}_p = \sum_{i=1}^{N} \frac{\mathbf{p}_i}{m_i} \cdot \frac{\partial}{\partial \mathbf{r}_i} \tag{C.5}$$

$$i\mathscr{L}_r = \sum_{i=1}^{N} \mathbf{F}_i \cdot \frac{\partial}{\partial \mathbf{p}_i} \tag{C.6}$$

$$i\mathscr{L}_{NHC} = -\sum_{i=1}^{N} \frac{p_{\eta_1}}{Q_1} \mathbf{p}_i \cdot \frac{\partial}{\partial \mathbf{p}_i} + \sum_{j=1}^{M} \frac{p_{\eta_j}}{Q_j} \frac{\partial}{\partial \eta_j} + \tag{C.7}$$

$$\sum_{j=1}^{M-1} \left(\frac{p_{\eta_{j-1}}^2}{Q_{j-1}} - p_{\eta_j} \frac{p_{\eta_{j+1}}}{Q_{\eta_{j+1}}} \right) \frac{\partial}{\partial p_{\eta_j}} + \frac{p_{\eta_{M-1}}^2}{Q_{M-1} - k_B} \frac{\partial}{\partial p_{\eta_M}} \tag{C.8}$$

This was implemented and recovered the ergodic velocity distribution and phase space exploration.

C.2 Empirical Forcefield Routines

The module in CASTEP, which handles empirical forcefields was developed entirely during the course of the project. This includes calculation of a selection of one-, two- and three-body-potentials, neighbour lists and mechanisms to hook in various extra force generators such as neural-network potentials, external library potentials and exotic force generators such as fourier interpolated potential energy surfaces.

The code is written to be parallel-safe using MPI and also to be actively parallelised using OpenMP.

One key element which was required, but for which little information could be found was the means of safely generating three-body neighbour lists, and so this had to be developed. In hopes of posterity for those who might need to

generate their own, this is provided here:

Algorithm 4 The general idea of the interface of the search algorithm. Recommend using a binary search

```
search(arr:list, int:value, bool:greater)
if greater then
  FIND list[index] ≥ value
else
  FIND list[index] > value
end if
return int:index
```

Algorithm 5 Collates two neighbours lists for atoms i&j returning only the unique reduced set, without repeating on further iterations

Input: arr:NL[IJ], int:NN[IJ], int:ID[IJ]
{Neighbour lists, number of neighbours and id of atoms i & j}
Output: arr:NL, int:N
{New collated neighbour list, number of common neighbours}
using **search** (Alg. 4)
int:j = **search**(NLJ,IDI,**true**)
int:init = **search**(NLI,IDJ,**true**)
int:tmp_i = **search**(NLI,NLJ[j])
N=0; NL=0
for int:i=init **to** NNI **do**
  if NLI[i] $\geq$ NLJ[j] **then**
    int:next_j = **search**(NLJ[j:],NLI[i])
    for j=j**to** next_j **do**
      for tmp_i = tmp_i **to** NNI **do**
        if NLI[tmp_i] $\geq$ NLJ[j] **then**
          exit
        end if
      end for
      if NLI[tmp_i] $\neq$ NLJ[j] **then**
        N++
        NL[N] = NLJ[j]
      end if
    end for
    if NLI[i] = NLJ[j] **then**
      j++
    end if
  end if
  N++
  NL[N] = NLI[i]
end for
for i=j **to** NNJ **do**
  if any(NLI[tmp_i:] = NLJ[i]) **then**
    cycle
  end if
  N++
  NL[N] = NLJ[i]
end for

C.3 Voronoi Tesselation

An algorithm was written and implemented into CASTEP [Clark *et al.*, 2005] which enabled the generation of Voronoi cells from within the code, based on the code given in Allen and Tildesley [1987].

The idea was that the data for post-analysis techniques which we wanted to use, involving Voronoi cells or Delaunay triangulations would be accessible. It later turned out that the software OVITO [Stukowski, 2010] had this capability in-built, and so rendered this effort unnecessary for this project, however, for further extension to the CASTEP suite, it may prove useful as it may be possible to render fast calculation of neighbour lists usuing this techinique for the pair-potential module or there is suggestion of a rapid preconditioner for geometry optimisation which relies on the use of a nearest neighbour technique.

Bibliography

G. J. Ackland and A. P. Jones. Applications of local crystal structure measures in experiment and simulation. *Phys. Rev. B*, 73:054104, Feb 2006.

M. P. Allen and D. J. Tildesley. *Computer Simulation of Liquids*. Oxford University Press, 1987. ISBN 0198556454.

H. C. Andersen. Molecular dynamics simulations at constant pressure and/or temperature. *The Journal of Chemical Physics*, 72(4):2384–2393, 1980.

J. D. Anderson. *Fundamentals of Aerodynamics*. McGraw-Hill Companies, 2001. ISBN 0072373350.

S. I. Anisimov, V. V. Zhakhovskiĭ, and V. E. Fortov. Shock wave structure in simple liquids. *Journal of Experimental and Theoretical Physics Letters*, 65(9): 755–761, 1997. ISSN 0021-3640.

N. Ashcroft and I. Mermin. *Solid State Physics*. Harcourt College Publishers, 1976. ISBN 0030839939.

S. A. Ashraf, B. G. Stewart, D. Hepburn, and C. Zhou. Simulation of shock wave due to partial discharge using finite element method. *Annual Report - Conference on Electrical Insulation and Dielectric Phenomena, CEIDP*, pages 120–123, 2007. ISSN 0084-9162. doi: 10.1109/CEIDP.2007.4451469.

L. M. Barker. Laser interferometry in shock-wave research. *Experimental Mechanics*, 12(5):209–215, May 1972.

A. P. Bartók, M. C. Payne, R. Kondor, and G. Csányi. Gaussian approximation potentials: The accuracy of quantum mechanics, without the electrons. *Phys. Rev. Lett.*, 104:136403, 2010.

J. Behler. Atom-centered symmetry functions for constructing high-dimensional neural network potentials. *The Journal of Chemical Physics*, 134 (7):074106, 2011.

H. J. C. Berendsen and W. F. van Gunsteren. Practical algorithms for dynamic simulations. *Molecular Dynamics Simulations of Statistical Mechanics Systems*, pages 43–65, Proceedings of the 97th Int. "Enrico Fermi" School of Physics, 1986.

H. J. C. Berendsen, J. P. M. Postma, W. F. van Gunsteren, A. DiNola, and J. R. Haak. Molecular dynamics with coupling to an external bath. *The Journal of Chemical Physics*, 81(8):3684–3690, 1984.

J. D. Bernal. A geometrical approach to the structure of liquids. *Nature*, 183: 141 –147, 1959.

F. Birch. Finite elastic strain of cubic crystals. *Phys. Rev.*, 71:809–824, Jun 1947.

R. Bowley and M. Sánchez. *Introductory statistical mechanics*. Oxford University Press. ISBN 0198505760.

R. A. Buckingham. The classical equation of state of gaseous helium, neon and argon. *Proceedings of the Royal Society of London A: Mathematical, Physical and Engineering Sciences*, 168(933):264–283, 1938. ISSN 0080-4630.

F. Buda, R. Car, and M. Parrinello. Thermal expansion of c-Si via ab initio molecular dynamics. *Phys. Rev. B*, 41:1680–1683, Jan 1990.

J. Budzien, A. P. Thompson, and S. V. Zybin. Reactive molecular dynamics simulations of shock through a single crystal of pentaerythritol tetranitrate. *The Journal of Physical Chemistry B*, 113(40):13142–13151, 2009.

S. J. Clark, M. D. Segall, C. J. Pickard, P. J. Hasnip, M. J. Probert, K. Refson, and M.C. Payne. First principles methods using CASTEP. *Z. Kristall.*, 220: 567–570, 2005.

L. Coes. A new dense crystalline silica. *Science*, 118(3057):131–132, 1953. ISSN 0036-8075.

B. J. Cowen and M. S. El-Genk. On force fields for molecular dynamics simulations of crystalline silica. *Computational Materials Science*, 107:88 – 101, 2015. ISSN 0927-0256.

G. Csányi, T. Albaret, M. C. Payne, and A. De Vita. "learn on the fly": A hybrid classical and quantum-mechanical molecular dynamics simulation. *Phys. Rev. Lett.*, 93:175503, Oct 2004.

L. Davison and R. A. Graham. Shock compression of solids. *Physics Reports*, 55 (4):255 – 379, 1979. ISSN 0370-1573.

P. Debye. Zur Theorie der spezifischen Wärmen [On the theory of specific heats]. *Annalen der Physik*, 344(14):789–839, 1912. ISSN 1521-3889.

R. D. Dick, R. H. Warnes, and J. Skalyo. Shock compression of solid argon. *The Journal of Chemical Physics*, 53(5):1648–1651, 1970.

D. D. Dlott. Ultrafast spectroscopy of shock waves in molecular materials. *Annual Review of Physical Chemistry*, 50(1):251–278, 1999.

N. Dubrovinskaia, L. Dubrovinsky, N. A. Solopova, A. Abakumov, S. Turner, M. Hanfland, E. Bykova, M. Bykov, C. Prescher, V. B. Prakapenka, S. Petitgirard, I. Chuvashova, B. Gasharova, Y.-L. Mathis, P. Ershov, I. Snigireva, and A. Snigirev. Terapascal static pressure generation with ultrahigh yield strength nanodiamond. *Science Advances*, 2(7), 2016.

E. Engel and R. Dreizler. *Density Functional Theory : An Advanced Course*. Springer-Verlag, 2011. ISBN 9783642140891.

P. P. Ewald. Die Berechnung optischer und elektrostatischer Gitterpotentiale [On the calculation of optical and electrostatic grid potentials]. *Annalen der Physik*, 369(3):253–287, 1921.

G. S. Ezra. Reversible measure-preserving integrators for non-hamiltonian systems. *The Journal of Chemical Physics*, 125(3):034104, 2006.

M. Farrow. *Computer Simulation of Shock Waves in Condensed Matter*. PhD thesis, University of York, York, 2009.

M. R. Farrow and M. I. J. Probert. Atomistic molecular dynamics simulations of shock compressed quartz. *The Journal of chemical physics*, 135(4):044508, 2011.

A. C. Faul. *A Concise Introduction to Numerical Analysis*. CRC Press, 2016. ISBN 978-1-4987-1218-7.

R. P. Feynman and A. Hibbs. *Quantum Mechanics and Path Integrals*. McGraw-Hill Companies, 1965. ISBN 0070206503.

Michael Fleischer. New mineral names. *American Mineralogist*, 47(2):172–174, 1962.

D. Frenkel and B. Smit. *Understanding Molecular Simulation : From Algorithms to Applications*. Academic Press, 1996. ISBN 0-12-267370-0.

E. Grüneisen. Theorie des festen zustandes einatomiger elemente [Theory of the solid state of monoatomic elements]. *Annalen der Physik*, 344(12):257–306, 1912. ISSN 1521-3889.

O. Guerrero-Miramontes. A beginners guide to the modeling of shock/uniaxial/quasi-isentropic compression using the lammps molecular dynamics simulator. URL `https://www.researchgate.net/publication/259644293_A_beginner's_guide_to_the_modeling_of_shockuniaxialquasi-isentropic_compression_using_the_LAMMPS_molecular_dynamics_simulator_By_Oscar_Guerrero-Miramontes`. Accessed: 20/03/17.

A. Fernández Guillermet. On the use of grüneisen parameters in the treatment of shock-wave data. *International Journal of Thermophysics*, 8(6):751–761, Nov 1987. ISSN 1572-9567.

Y. Guissani and B. Guillot. A numerical investigation of the liquidvapor coexistence curve of silica. *The Journal of Chemical Physics*, 104(19):7633–7644, 1996.

J. M. Haile. *Molecular Dynamics Simulation : Elementary Methods*. Wiley-Interscience, 1992. ISBN 0-471-81966-2.

J. L. Hall, F. E. Belles, and M. R. Lauver. Shock-tube gas temperature measurements by infrared monochromatic radiation pyrometry. 1965. URL `https://ntrs.nasa.gov/archive/nasa/casi.ntrs.nasa.gov/19650021298.pdf`.

M. Hebbache and M. Zemzemi. Ab initio study of high-pressure behavior of a low compressibility metal and a hard material: Osmium and diamond. *Phys. Rev. B*, 70:224107, Dec 2004.

P. Hohenberg and W. Kohn. Inhomogeneous electron gas. *Phys. Rev.*, 136: B864–B871, 1964.

B. L. Holian. Atomistic computer simulations of shock waves. *Shock Waves*, 5 (3):149–157, 1995. ISSN 0938-1287.

J. D. Honeycutt and H. C. Andersen. Molecular dynamics study of melting and freezing of small lennard-jones clusters. *The Journal of Physical Chemistry*, 91 (19):4950–4963, 1987.

Joseph Honour. Ultrafast cameras streak ahead. *Physics World*, 2001. URL `https://physicsworld.com/a/ultrafast-cameras-streak-ahead/`. Accessed 13-8-2018.

R. Hooke, D. Papin, J. Young, and S. Sturmy. *Lectures de potentia restitutiva, or, Of spring : explaining the power of springing bodies : to which are added some collections ...* 1678.

W. G. Hoover. Canonical dynamics: Equilibrium phase-space distributions. *Phys. Rev. A*, 31:1695–1697, Mar 1985.

W. G. Hoover, O. Kum, and H. A. Posch. Time-reversible dissipative ergodic maps. *Phys. Rev. E*, 53:2123–2129, Mar 1996.

B. Hopkinson. A method of measuring the pressure produced in the detonation of high explosives or by the impact of bullets. *Philosophical Transactions of the Royal Society of London A: Mathematical, Physical and Engineering Sciences*, 213(497-508):437–456, 1914. ISSN 0264-3952.

H. Hugoniot. Mémoire sur la propagation des mouvements dans les corps et spécialement dans les gaz parfaits (première partie) [memoir on the propagation of movements in bodies, especially perfect gases (first part)]. *Journal de l'École Polytechnique*, 57:3–97, 1887.

J. Jung, W. Nishima, M. Daniels, G. Bascom, C. Kobayashi, A. Adedoyin, M. Wall, A. Lappala, D. Phillips, W. Fischer, C.-S. Tung, T. Schlick, Y. Sugita, and K. Y. Sanbonmatsu. Scaling molecular dynamics beyond 100,000 processor cores for large-scale biophysical simulations. *Journal of Computational Chemistry*, 1–12, 2019. doi: 10.1002/jcc.25840.

J. Kalikka, J. Akola, and R. O. Jones. Simulation of crystallization in $ge_2sb_2te_5$: A memory effect in the canonical phase-change material. *Phys. Rev. B*, 90: 184109, Nov 2014.

G. I. Kanel, V. E. Fortov, and S. V. Razorenov. *Shock-Wave Phenomena and the Properties of Condensed Matter*, pages 29–82. Springer New York, New York, NY, 2004. ISBN 978-1-4757-4282-4.

C. L. Kelchner, S. J. Plimpton, and J. C. Hamilton. Dislocation nucleation and defect structure during surface indentation. *Phys. Rev. B*, 58:11085–11088, Nov 1998.

T. Kihara and S. Koba. Crystal structures and intermolecular forces of rare gases. *Journal of the Physical Society of Japan*, 7(4):348–354, 1952.

G. Kimminau, B. Nagler, A. Higginbotham, W. Murphy, J. Wark, N. Park, J. Hawreliak, D. Kalantar, H. Lorenzana, and B. Remington. Simulating picosecond X-ray diffraction from crystals using FFT methods on MD output. *AIP Conference Proceedings*, 955(1):1251–1254, 2007.

M. L. Klein and J. A. Venables. *Rare Gas Solids*. Academic Press, 1976. ISBN 0124135013.

S. Klotz, K. Kamenov, S. T. Weir, Y. Vohra, W. Holzapfel, J. B. Parise, F. A. Gorelli, A. F. Goncharov, F. M. Grosche, C. Sanloup, P. F. McMillan, E. Bailey, K. Leinenweber, M. C. Wilding, and R. J. Hemley. *High-Pressure Physics*. CRC Press, 2012. ISBN 978-1-4398-1428-4.

M. D. Knudson and M. P. Desjarlais. Adiabatic release measurements in α-quartz between 300 and 1200 gpa: Characterization of α-quartz as a shock standard in the multimegabar regime. *Phys. Rev. B*, 88:184107, Nov 2013.

W. Kohn and L. J. Sham. Self-consistent equations including exchange and correlation effects. *Phys. Rev.*, 140:A1133–A1138, 1965.

H. Kolsky. An investigation of the mechanical properties of materials at very high rates of loading. *Proceedings of the Physical Society. Section B*, 62(11):676, 1949.

C.H. Konrad, James Asay, and C.A. Hall. Use of z-pinch sources for high-pressure shock wave studies. 01 1998. doi: 10.2172/570174.

P. Krehl and S. Engemann. August toepler — the first who visualized shock waves. *Shock Waves*, 5(1):1–18, Jun 1995.

P. O. K. Krehl. The classical rankine-hugoniot jump conditions, an important cornerstone of modern shock wave physics: ideal assumptions vs. reality. *The European Physical Journal H*, 40(2):159–204, Mar 2015. ISSN 2102-6467.

A. M. Krivtsov and V. A. Kuz'kin. Derivation of equations of state for ideal crystals of simple structure. *Mechanics of Solids*, 46(3):387, Jul 2011. ISSN 1934-7936.

R. Kubo. The fluctuation-dissipation theorem. *Reports on Progress in Physics*, 29 (1):255, 1966.

A. Kubota, M.-J. Caturla, J. S. Stölken, and M. D. Feit. Densification of fused silica due to shock waves and its implications for 351 nm laser induced damage. *Opt. Express*, 8(11):611–616, May 2001.

A. D. Kulkarni, D. G. Truhlar, S. Goverapet Srinivasan, A. C. T. van Duin, P. Norman, and T. E. Schwartzentruber. Oxygen interactions with silica surfaces: Coupled cluster and density functional investigation and the development of a new reaxff potential. *The Journal of Physical Chemistry C*, 117(1): 258–269, 2013.

L. D. Landau and E. M. Lifshitz. *Course of Theoretical Physics Vol V: Statistical Physics*. Pergamon Press, 1980. ISBN 0080230393.

P. Langevin. Sur la théorie du mouvement brownien [On the theory of brownian motion]. *C. R. Acad. Sci. (Paris)*, 146:530–533, 1908.

E. A. Lazar, J. K. Mason, R. D. MacPherson, and D. J. Srolovitz. Complete topology of cells, grains, and bubbles in three-dimensional microstructures. *Phys. Rev. Lett.*, 109:095505, Aug 2012.

E. A. Lazar, J. Han, and D. J. Srolovitz. Topological framework for local structure analysis in condensed matter. *Proceedings of the National Academy of Sciences*, 112(43):E5769–E5776, 2015.

B. Leimkuhler, E. Noorizadeh, and F. Theil. A gentle stochastic thermostat for molecular dynamics. *J. Stat. Phys.*, 135:261–277, 2009.

J. E. Lennard-Jones. On the determination of molecular fields. *Proc. R. Soc. Lond. A*, 106(738):463–477, 1924.

J.-B. Maillet and S. Bernard. Uniaxial hugoniostat: Method and applications. In *Shock Compression of Condensed Matter*. American Institute of Physics, 2001.

J.-B. Maillet and G. Stoltz. Sampling constraints in average: The example of hugoniot curves. *Applied Mathematics Research eXpress*, 2008, 2008.

J.-B. Maillet, M. Mareschal, L. Soulard, R. Ravelo, P. S. Lomdahl, T. C. Germann, and B. L. Holian. Uniaxial hugoniostat: A method for atomistic simulations of shocked materials. *Phys. Rev. E*, 63:016121, Dec 2000.

S. P. Marsh. *LASL Shock Hugoniot Data*. Berkeley : University of California Press, 1980. ISBN 0520040082.

G. J. Martyna, M. L. Klein, and M. Tuckerman. Nosé-hoover chains – the canonical ensemble via continuous dynamics. *Journal Of Chemical Physics*, 97:2635–2643, 1992.

D. Marx. *Ab initio molecular dynamics*. Cambridge University Press, 2012. ISBN 978-1107663534.

E. F. Medici, J. S. Allen, and G. P. Waite. Modeling shock waves generated by explosive volcanic eruptions. *Geophysical Research Letters*, 41(2):414–421, 2013.

G. Mie. Zur kinetischen theorie der einatomigen körper [On the kinetic theory of monoatomic bodies]. *Annalen der Physik*, 316(8):657–697, 1903.

H. R. Moeller and C. F. Squire. Ultrasonic velocities in solid argon. *Phys. Rev.*, 151:689–693, Nov 1966.

S. Munetoh, T. Motooka, K. Moriguchi, and A. Shintani. Interatomic potential for Si-O systems using tersoff parameterization. *Computational Materials Science*, 39(2):334 – 339, 2007. ISSN 0927-0256.

Chuanhui Nie, Junping Wang, and Ruiting Gong. Gruneisen parameter for hcp iron at extreme compression. *High Pressure Research*, 31:214–218, 03 2011.

R. H. Nochetto, K. G. Siebert, and A. Veeser. Theory of adaptive finite element methods: An introduction. In Ronald DeVore and Angela Kunoth, editors, *Multiscale, Nonlinear and Adaptive Approximation*, pages 409–542, Berlin, Heidelberg, 2009. Springer. ISBN 978-3-642-03413-8.

S. Nosé. A unified formulation of the constant temperature molecular dynamics methods. *The Journal of Chemical Physics*, 81(1):511–519, 1984.

S. Nosé. Constant temperature molecular dynamics methods. *Progress of Theoretical Physics Supplement*, 103:1–46, 1991.

S. Ono. First-principles molecular dynamics calculations of the equation of state for tantalum. *Int. J. Mol. Sci.*, 10, Sep 2009. ISSN 1422-0067.

M. C. Payne, M. P. Teter, D. C. Allan, T.A. Arias, and J. D. Joannopoulos. Iterative minimization techniques for ab initio total-energy calculations - molecular-dynamics and conjugate gradients. *Rev. Mod. Phys.*, 64:1045–1097, 1992.

Steve Plimpton. Fast parallel algorithms for short-range molecular dynamics. *Journal of Computational Physics*, 117(1):1 – 19, 1995. ISSN 0021-9991. URL `http://lammps.sandia.gov/`.

J.-P. Poirier and A. Tarantola. A logarithmic equation of state. *Physics of the Earth and Planetary Interiors*, 109(1):1 – 8, 1998. ISSN 0031-9201.

S. P. Popov. Numerical study of the interaction between shocks and rarefaction waves in an ideal gas. *Computational Mathematics and Mathematical Physics*, 47(1):151–156, Jan 2007. ISSN 1555-6662.

M. I. J. Probert. Improved algorithm for geometry optimisation using damped molecular dynamics. *Journal of Computational Physics*, 191(1):130 – 146, 2003. ISSN 0021-9991.

D. Quigley. Mdtep analysis program. URL `http://www.tcm.phy.cam.ac.uk/castep/MD/node19.html`. Accessed: 08/08/17.

A. I. M. Rae. *Quantum Mechanics*. Taylor & Francis, 2008. ISBN 1584889705.

W. J. M. Rankine. On the thermodynamic theory of waves of finite longitudinal disturbances. *Philosophical Transactions of the Royal Society of London*, 160:277–28, 1870.

R. Ravelo, B. L. Holian, T. C. Germann, and P. S. Lomdahl. Constant-stress hugoniostat method for following the dynamical evolution of shocked matter. *Phys. Rev. B*, 70:014103, 2004.

Lord Rayleigh. Aerial plane waves of finite amplitude. *Proceedings of the Royal Society of London A: Mathematical, Physical and Engineering Sciences*, 84(570): 247–284, 1910. ISSN 0950-1207.

Lord Rayleigh and W. Ramsay. Argon, a new constituent of the atmosphere. *Proceedings of the Royal Society of London*, 57(340-346):265–287, 1895.

K. Refson. Running phonon calculations in castep. URL `http://www.tcm.phy.cam.ac.uk/castep/Phonons_Guide/Castep_Phononsch2.html`. Accessed: 03/08/17.

M.H. Rice, R.G. McQueen, and J.M. Walsh. Compression of solids by strong shock waves. In Frederick S. and David T., editors, *Advances in Research and Applications*, volume 6 of *Solid State Physics*, pages 1–63. Academic Press, 1958.

I. Saika-Voivod, F. Sciortino, T. Grande, and P. H. Poole. Phase diagram of silica from computer simulation. *Phys. Rev. E*, 70:061507, Dec 2004.

F. A. Sapozhnikov, G. V. Ionov, and V. V. Dremov. An adaptive template method for analyzing crystal structures and defects in molecular dynamics simulations of high-rate deformations. *Russian Journal of Physical Chemistry B*, 2(2):238–245, 2008.

SERC. URL `https://serc.carleton.edu/research_education/equilibria/metamorphic_diagrams.html`. Accessed: 27/6/18.

I. S. Sokolnikoff. *Mathematical theory of elasticity*. McGraw-Hill book company, 1956.

A. Stukowski. Visualization and analysis of atomistic simulation data with OVITOthe open visualization tool. *Modelling and Simulation in Materials Science and Engineering*, 18(1):015012, 2010. URL `www.ovito.org`.

A. Stukowski. Structure identification methods for atomistic simulations of crystalline materials. *Modelling and Simulation in Materials Science and Engineering*, 20(4):045021, 2012.

V. Swamy, S. K. Saxena, B. Sundman, and J. Zhang. A thermodynamic assessment of silica phase diagram. *Journal of Geophysical Research: Solid Earth*, 99 (B6):11787–11794, 1994.

J. W. Swegle and D. E. Grady. Shock viscosity and the prediction of shock wave rise times. *Journal of Applied Physics*, 58(2):692–701, 1985.

W. C. Swope, H. C. Andersen, P. H. Berens, and K. R. Wilson. A computer simulation method for the calculation of equilibrium constants for the formation of physical clusters of molecules: Application to small water clusters. *J. Chem. Phys*, 76:637–649, Jan 1982.

G. R. Tear, D. E. Eakins, D. J. Chapman, and W. G. Proud. Technique to measure change in birefringence under shock compression. *Journal of Physics: Conference Series*, 500(19):192020, 2014.

J. Tersoff. New empirical approach for the structure and energy of covalent systems. *Phys. Rev. B*, 37:6991–7000, 1988.

H. F. Trotter. On the product of semi-groups of operators. *Proc. Amer. Math. Soc.*, 10:545–551, 1959.

R. F. Trunin. *Shock Compression of Condensed Materials*. Cambridge University Press, Jun 1998. ISBN 0521582903.

M. Tuckerman, B. J. Berne, and G. J. Martyna. Reversible multiple time scale molecular dynamics. *The Journal of Chemical Physics*, 97(3):1990–2001, 1992.

M. E. Tuckerman. *Statistical Mechanics: Theory and Molecular Simulation*. Oxford Graduate Texts, 2010. ISBN 9780198525264.

M. E. Tuckerman, C. J. Mundy, and G. J. Martyna. On the classical statistical mechanics of non-hamiltonian systems. *EPL (Europhysics Letters)*, 45(2):149, 1999.

B. W. H. van Beest, G. J. Kramer, and R. A. van Santen. Force fields for silicas and aluminophosphates based on *ab initio* calculations. *Phys. Rev. Lett.*, 64: 1955–1958, Apr 1990.

A. C. T. van Duin, S. Dasgupta, F. Lorant, and W. A. Goddard. Reaxff: a reactive force field for hydrocarbons. *J. Phys. Chem. A*, 105:9396–9409, 2001. ISSN 1089-5639.

P. Vinet, J. Ferrante, J. H. Rose, and J. R. Smith. Compressibility of solids. *Journal of Geophysical Research: Solid Earth*, 92(B9):9319–9325, 1987. ISSN 2156-2202.

E. Volterra. Alcuni risultati di prove dinamiche sui materiali [Some results on the dynamic testing of materials]. *Rivista Nuovo Cimento*, 4:1–28, 1948.

J. Wackerle. Shock-wave compression of quartz. *Journal of Applied Physics*, 33 (3):922–937, 1962.

C. E. Wehrenberg, D. McGonegle, C. Bolme, A. Higginbotham, A. Lazicki, H. J. Lee, B. Nagler, H.-S. Park, B. A. Remington, R. E. Rudd, M. Sliwa, M. Suggit, D. Swift, F. Tavella, L. Zepeda-Ruiz, and J. S. Wark. In situ x-ray diffraction measurement of shock-wave-driven twinning and lattice dynamics. *Nature*, 550:496–499, 2017.

R. C. West, editor. *CRC Handbook of Chemistry and Physics, 55th Ed.* CRC Press, 1974. ISBN 0878194541.

Ertl Balu: Wikipedia. Voronoi image, a. URL `https://upload.wikimedia.org/wikipedia/commons/5/54/Euclidean_Voronoi_diagram.svg`. Accessed: 21/07/17.

Johan Fredriksson: Wikipedia. Gas gun schematic, b. URL `https://upload.wikimedia.org/wikipedia/commons/1/1a/Light-gas_gun.svg`. Accessed: 17/07/18.

I.-C. Yeh and M. L. Berkowitz. Ewald summation for systems with slab geometry. *The Journal of Chemical Physics*, 111(7):3155–3162, 1999.

V. V. Zhakhovskiĭ, S. V. Zybin, K. Nishihara, and S. I. Anisimov. Shock wave structure in Lennard-Jones crystal via molecular dynamics. *Phys. Rev. Lett.*, 83:1175–1178, Aug 1999.

V. V. Zhakhovsky, M. M. Budzevich, N. A. Inogamov, I. I. Oleynik, and C. T. White. Two-zone elastic-plastic single shock waves in solids. *Phys. Rev. Lett.*, 107:135502, Sep 2011.